June 4, 2003

Final Report

For

High Resolution Inductive Sensor Arrays for UXO Detection, Identification and Clutter
Suppression

SERDP Project Number UX-1326

P.I.: Neil J. Goldfine
JENTEK Sensors, Inc.
Waltham, MA

VIEWS, OPINIONS, AND/OR FINDINGS CONTAINED IN THIS REPORT ARE THOSE OF
THE AUTHOR(S) AND SHOULD NOT BE CONSTRUED AS AN OFFICIAL
DEPARTMENT OF THE ARMY POSITION, OR DECISION UNLESS SO DESIGNATED
BY OTHER OFFICIAL DOCUMENTATION

Report Documentation Page

1. REPORT DATE **04 JUN 2004**	2. REPORT TYPE **Final**	3. DATES COVERED **-**

4. TITLE AND SUBTITLE	5a. CONTRACT NUMBER
High Resolution Inductive Sensor Arrays for UXO Detection, Identification and Clutter Suppression	5b. GRANT NUMBER
	5c. PROGRAM ELEMENT NUMBER

6. AUTHOR(S)	5d. PROJECT NUMBER
Dr. Neil J. Goldfine	**UX-1326**
	5e. TASK NUMBER
	5f. WORK UNIT NUMBER

7. PERFORMING ORGANIZATION NAME(S) AND ADDRESS(ES) **JENTEK Sensors, Inc. 110-1 Clematis Avenue Waltham, MA 02453**	8. PERFORMING ORGANIZATION REPORT NUMBER

9. SPONSORING/MONITORING AGENCY NAME(S) AND ADDRESS(ES) **Strategic Environmental Research & Development Program 901 N Stuart Street, Suite 303 Arlington, VA 22203**	10. SPONSOR/MONITOR'S ACRONYM(S) **SERDP**
	11. SPONSOR/MONITOR'S REPORT NUMBER(S)

12. DISTRIBUTION/AVAILABILITY STATEMENT
Approved for public release, distribution unlimited

13. SUPPLEMENTARY NOTES
The original document contains color images.

14. ABSTRACT

15. SUBJECT TERMS

16. SECURITY CLASSIFICATION OF:			17. LIMITATION OF ABSTRACT	18. NUMBER OF PAGES	19a. NAME OF RESPONSIBLE PERSON
a. REPORT **unclassified**	b. ABSTRACT **unclassified**	c. THIS PAGE **unclassified**	**UU**	**68**	

PREFACE

This document has been submitted under Contract Number DACA72-03-C-0001. The information contained in this document includes both development under this SERDP contract and development under JENTEK IR&D.

Table of Contents

Summary

This report provides an overview of the results for the base program under SERDP Project Number UX-1326. The base program for this project has been successfully completed and all technical milestones have been met. The focus of efforts during the base program has been on (1) adaptation of the instrumentation and probe electronics, (2) testing of an enhanced drive winding method developed under JENTEK IR&D, (3) fabrication and testing of the elements of a sixteen channel array with higher resolution than the original prototype MWM®-Array, (4) refinement and validation of JENTEK's model based inversion method for estimation of depth and size of spherical objects, (5) preliminary field testing, (6) development of UXO depth and size measurement method, and (7) preliminary development of model-based clutter suppression methods.

Significant results achieved during the base program have included:
- **Demonstration of a substantial improvement in signal to noise and associated depth of sensitivity** for buried bomblets and fabricated spherical objects. This was accomplished through an enhanced drive winding construct using adapted impedance instrumentation and probe electronics developed under JENTEK IR&D.
- **Demonstration that doubling the resolution of the sensing element array can be accomplished without reducing signal-to-noise.** Thus, higher resolution images can be provided without loss of depth of sensitivity. This higher resolution image will be used to suppress clutter and improve object feature recognition.
- **Demonstration of rapid scanning capability.** This permits real-time data acquisition with images created at scan rates of up to 4 ft/sec with single frequency operation. Higher data acquisition rates and higher resolution images can be achieved with higher frequency operation with instrumentation enhancements. However, for object identification, lower or multiple frequency operation, that can lead to lower scan speeds, may be necessary. This potentially permits real-time analysis for classification based on estimated object properties.
- **Demonstration of preliminary object shape discrimination capability.** Preliminary scan images over simple objects, such as a spherical bomblet and a cylinder, indicate object shape and orientation (in a plane parallel to the sensing array).
- **Demonstration of preliminary model based depth and size estimation potential using a model based grid method.** These methods provide estimates of object properties to assist in object identification and clutter suppression.
- **Demonstration of object imaging in the field.** Preliminary measurements were performed with the prototype drive and adapted instrumentation. Object responses obtained in the field were similar to laboratory measurements.
- **Generated criteria for enhancements and recommendations.** Observations from the field and laboratory measurements have been incorporated into enhancement criteria and recommendations for the follow-on program.

Background

The efficiency of unexploded ordnance (UXO) remediation is currently limited by the inadequate discrimination capability of existing UXO detection technologies. Inductive sensors with a single sensing coil are commonly used for detection. These single coil methods often detect all relevant metal objects but generally cannot discriminate between UXO and harmless clutter. The goal of this program is to develop inductive arrays for high resolution UXO imaging and discrimination by leveraging existing MWM-Array sensor and instrumentation technologies used in nondestructive testing.

Numerous researchers have demonstrated the value of increased resolution through simulation and field testing with single coils scanned carefully to produce registered images of object shape. JENTEK has been working on such solutions for many years and has fielded systems in traditional nondestructive testing applications that use a combination of high resolution inductive sensors and model based inversion methods to estimate multiple unknowns of subsurface cracks, and corrosion damage.

JENTEK's MWM-Array technology is based on unique designs for EMI sensor arrays, which use a single drive winding with multiple sense elements, which permit both high resolution imaging and accurate modeling of the sensor response to buried objects. The drive creates a shaped magnetic field pattern, which provides a continuous variation in the orientation of the magnetic field relative to the buried ordnance. Arrays of small inductive coils placed throughout the shaped field sense the field variations from conducting or magnetic UXO and clutter. Images obtained from scans over buried objects provide a basis for spatial filtering and signal processing. An eight-element prototype array developed five years ago demonstrated the capability to produce images of buried ordnance. Although this was at a much higher resolution than single coil methods, JENTEK's new commercial parallel architecture instrumentation can acquire data from up to 39 channels in less than 0.01 seconds.

JENTEK has also developed methods that use pre-computed databases of sensor responses to analyze the response of the sensors in real-time. This is critical since real time imaging in the field is necessary if confirmatory methods are to be employed at the UXO site. If successful, this program will provide an enhanced capability for the reclamation of lands contaminated with unexploded ordnance. The ability to discriminate between ordnance and clutter and provide information on ordnance type, depth and orientation would greatly reduce the false alarm rate and improve the efficacy of reclamation efforts, substantially reducing the cost and risks associated with UXO clearance and transitioning of lands back to public use.

Results

This section provides a summary of the results from this program.

For reference, the base program objectives were
(1) adapt JENTEK's commercial 39-channel impedance instrument for use with large scale MWM-Arrays for UXO detection
(2) establish MWM-Array object size and depth measurement capabilities for simple objects
(3) evaluate current UXO discrimination capabilities, and
(4) complete an initial field test of the prototype MWM-Array with adapted instrumentation.

The tasks for the base program plan were:
Task 1: Adapt current instrumentation
        Task 1.1: Adapt prototype array and perform initial laboratory tests
        Task 1.2: Adapt object size, shape, and depth algorithms
        Task 1.3: Fabricate 12 or more sense element array
        Task 1.4: Test new array and evaluate performance in laboratory tests
        Task 1.5: Evaluate trade-offs based on sense element size
Task 2: Demonstrate prototype array
        Task 2.1: Acquire representative inert munitions
        Task 2.2: Develop initial detection/suppression algorithm for field testing
        Task 2.3: Demonstrate size and depth measurements for known objects
        Task 2.4: Demonstrate preliminary discrimination and clutter suppression approach
        Task 2.5: Provide plan for initial field test
        Task 2.6: Perform initial field tests
Task 3: Determine enhancement criteria and recommendations
Task 4: Submit Base Program final report

The following sections include: (1) a description of the system adaptations; (2) laboratory testing results; (3) field testing results; and (4) a discussion of recommendations and criteria for enhancements.

System Adaptations

As part of this SERDP effort, JENTEK adapted the prototype instrumentation to support a modified winding design that provides higher sensitivity to buried objects. This has included adaptation of the MWM-Array probe electronics for the prototype MWM-Array so that JENTEK's parallel architecture, 39 channel impedance instrumentation can be used to support rapid imaging. Additional field hardening of the probe electronics prototype and MWM-Array will be required to support extensive field testing, but the current configuration was successfully used to support laboratory testing and limited field testing during the base program.

To support the development of an enhanced imaging capability, 16 sensing elements were fabricated. This essentially doubled the imaging resolution capability of the MWM-Array over the previous prototype. The array is designed to fit within the 0.61 m (24 in.) width of the existing drive winding structure with a reasonable spacing between the ends of the array and the return/side portions of the drive winding. The distance to the return portions of the drive winding needs to be large to minimize extra coupling of the magnetic field between the drive winding and the sense coils since this extra coupling is a source of element-to-element variability for the array response. Figure 1 shows the primary winding structure with the lower resolution 1 in. square sensing elements configured in an eight-element array. Figure 2 shows one of the new sense elements.
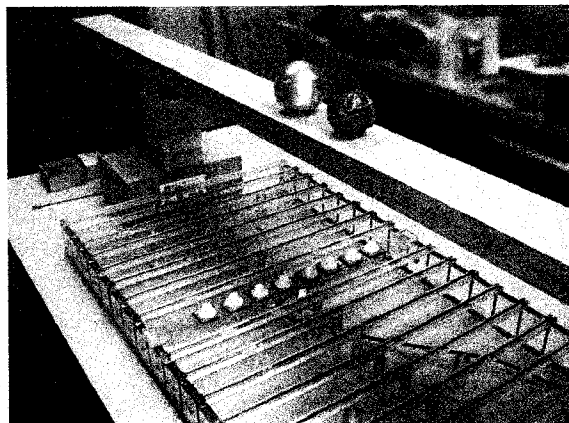

Figure 1. Photograph of the "old" sensing array consisting of 2.54 cm (1 in.) square sense element coils located within the primary winding structure. The beam suspended above the sensor was used for initial manual scans of the blue bomblet (right) and a 7.6 cm (3 in.) diameter aluminum sphere (left).
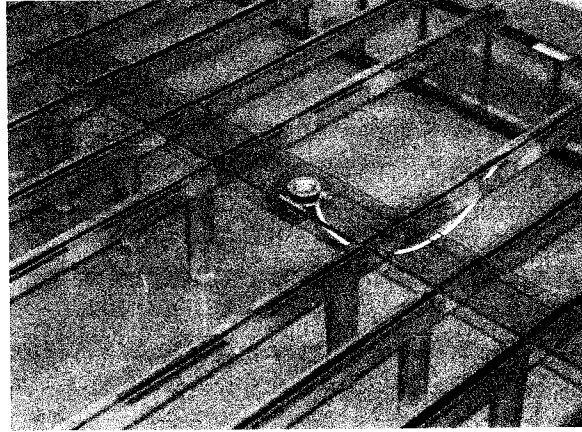
Figure 2. Photograph of a "new" 12.7 cm (0.5 in.) diameter sense element coil placed in the drive winding structure for initial testing.

A second linear array of 16 sense coils is being considered for fabrication in the follow-on program. The arrays would then be placed at different locations in the drive winding footprint and could provide complementary information about the object properties. The second array could also be placed next to first array, but offset a half-sense element in the array direction, to provide an even higher resolution image. Other sense coil orientations (such as vertical versus horizontal) can also be used to provide complementary information about the object properties. The tradeoffs associated with these various approaches, such as the information gained from the additional elements versus the increased complexity of the electronics, will be explored further in the follow-on program. Also, in the follow-on effort we expect to use a second drive winding oriented perpendicular to the original drive winding as conceived by Goldfine, et.al., in the mid 1990's for UXO and landmine detection.

Initial testing was performed on a single element of the array. Initial tests with single sensing elements have demonstrated improved sensitivity. Three single element configurations were tested: the "old" 2.54 cm (1 in.) square coil, the "new" 12.7 cm (0.5 in.) diameter round coil and the "new" coil with an enhanced drive winding construct. A model for estimating the signal-to-noise ratio (SNR) was adapted to the MWM-Array and indicated that modest modifications to the drive winding can help enhance sensitivity to buried objects. The two objects used in the initial tests, as shown in Figure 1, were a 7.6 cm (3 in.) diameter aluminum sphere and a 6.4 cm (2.5 in.) diameter blue bomblet from a cluster bomb. These objects were manually scanned along the beam (see Figure 12) at a rate of approximately 0.46 m/s (1.5 ft/s) over the various single sensing element configurations. Figure 2 shows the placement of a "new" sensing element coil placed at the center of the drive winding.

Measurements were made as the bomblet and aluminum sphere were scanned over the sensing element at various heights. These results are expressed in terms of the signal-to-noise ratio determined from

$$SNR = \sqrt{\left(\frac{Z_r - Z_{rb}}{\Delta Z_r}\right)^2 + \left(\frac{Z_i - Z_{ib}}{\Delta Z_i}\right)^2} \qquad (1)$$

where Z is the measured impedance, the subscript r denotes the real part, the subscript i denotes the imaginary part, the subscript b denotes the baseline response, and Δ denotes the noise level. The peak SNR value versus depth is plotted in Figure 3, with individual scans plotted in Figure 4 for the bomblet and Figure 5 for the aluminum sphere. In each case the peak in the SNR level occurs when the object is directly over the sense element. The variation in the position of the peak is a result of the manual scanning of the object.

These plots and the measurement scan show that the "old" 2.54 cm (1 in.) square coil and the "new" 12.7 cm (0.5 in.) diameter round coil have similar sensitivity to the objects. This is expected since the spatial variation of the secondary fields from objects of these sizes and at these distances will not be substantially different for sensing elements of this size. This indicates that there is no signal degradation due to the use of the smaller coils; the benefit of the smaller coils will be in the generation of higher resolution spatial images that should improve object discrimination. The use of the enhanced drive winding construct provides a substantial improvement in the sensitivity for both shallow and deep objects. The improvement in sensitivity is shown distinctly in several selected scans of Figure 4a and Figure 5a, where scans with the enhanced drive winding construct gives a larger signal at a deeper depth than the previous drive winding.
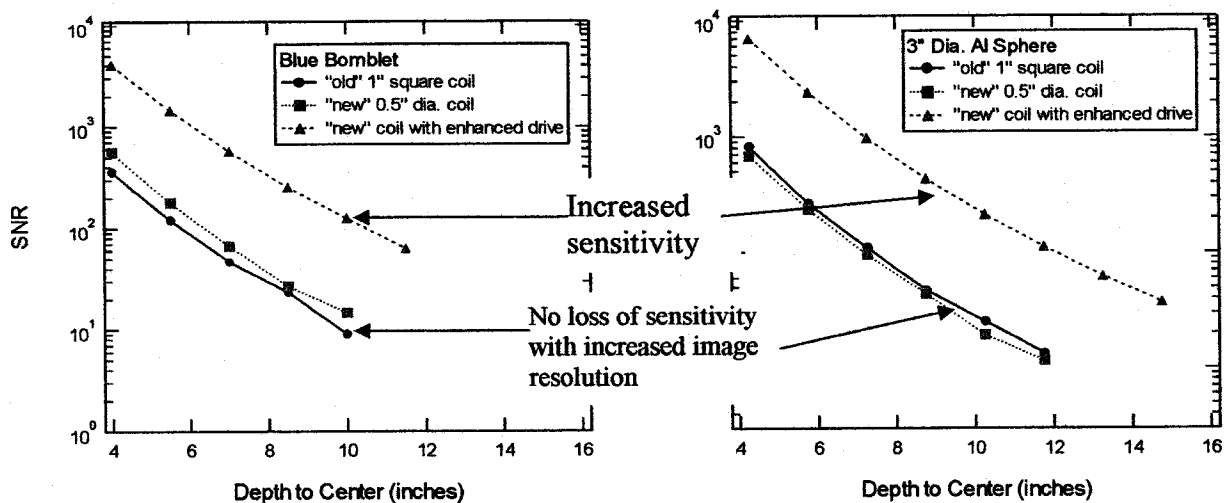

Figure 3. Peak signal-to-noise ratio versus depth for the blue bomblet and aluminum sphere.
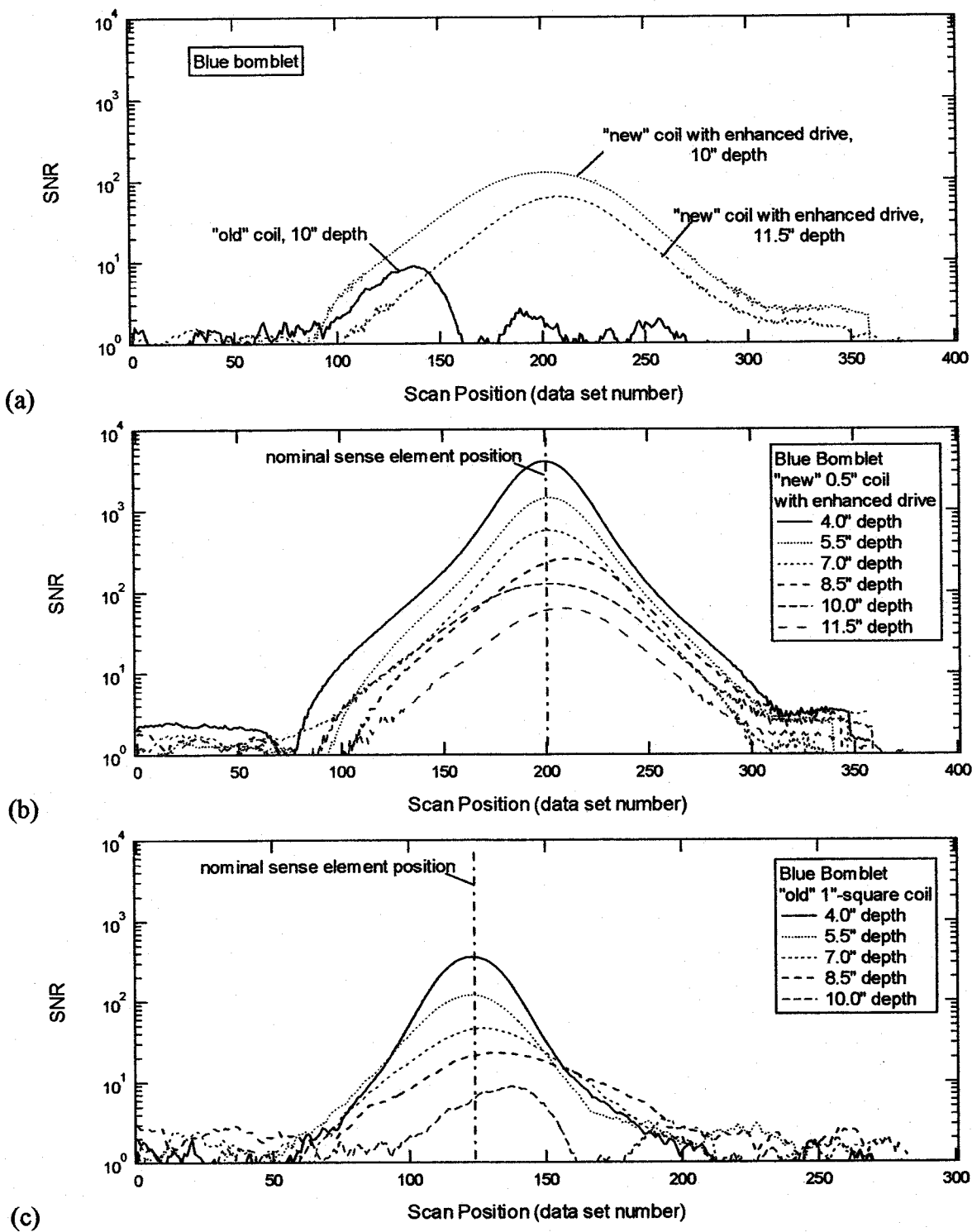
(a)

(b)

(c)

Figure 4. Signal-to-noise ratio plots for the blue bomblet. The scan position is the position of the bomblet as it is scanned over the sensing element. The dashed vertical line indicates the nominal position of the sense element.
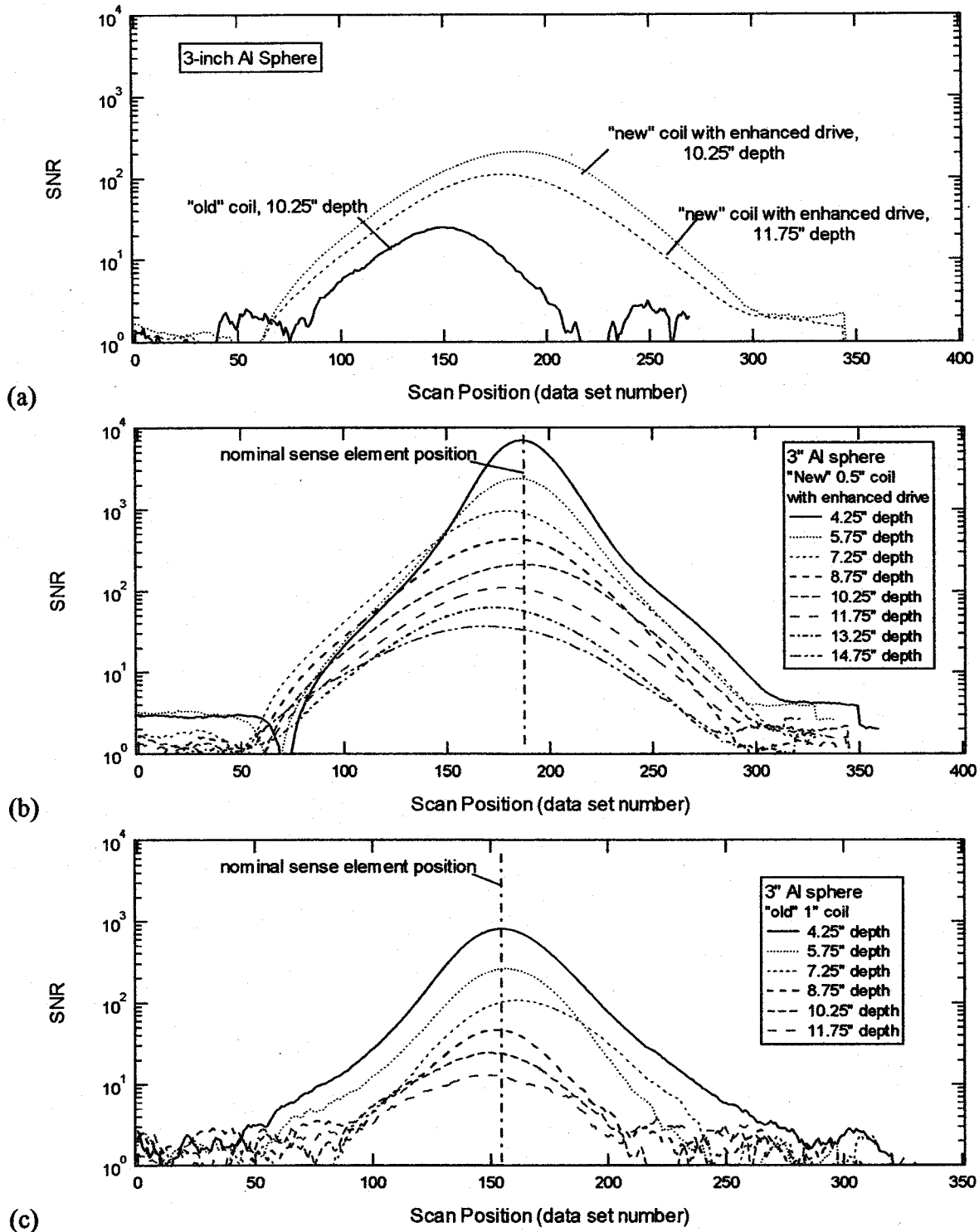
(a)

(b)

(c)

Figure 5. Signal-to-noise ratio plots for the 3 in. diameter aluminum sphere. The scan position is the position of the sphere as it is scanned over the sensing element. The dashed vertical line indicates the nominal position of the sense element.

The incorporation of the sensor array into a cart for scanning over objects is shown in Figure 6. For rapid imaging and measurements, individual connections are made to each individual sense coil. JENTEK's commercial parallel architecture impedance instrumentation can accommodate the simultaneous measurement of up to 39 measurement channels. The coils are connected to the instrumentation through an interface or probe electronics. These electronics provide amplification of the measurement signals and some signal filtering. Since the measurements with these sense coils and drive winding require gain settings different from our standard probe electronics, different internal circuit boards were used for the probe electronics. The data acquisition is controlled via a laptop computer. In this version, the laptop and support instrumentation were not placed onto the cart structure itself. Future designs are expected to have the support electronics and laptop in a more portable configuration, either incorporated into the cart itself or placed into backpacks.
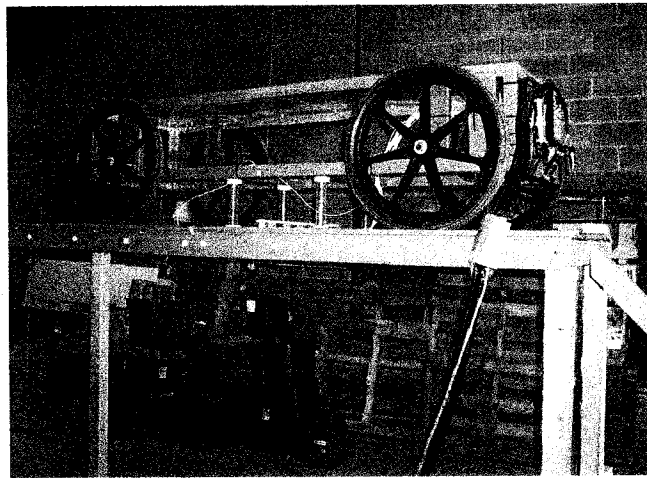

Figure 6. Photograph of the sensor array mounted onto a cart for scanning over objects and also the support instrumentation.

Models for system response

Modeling efforts have focused on improved representation of the drive windings, the interactions of multiple objects, and the effects of the surrounding media (soil) on the measurement response. New models account for both the drive winding enhancement and the effects of the return windings not addressed in our previous model[1,2]. Accurate models of the magnetic fields created by the drive winding structure have been used to calculate the secondary dipole fields excited for objects which can be represented by a polarization tensor; spherical objects have been specifically used in initial modeling and experiments. The sensing element response is then calculated from the secondary fields for spheres of various diameters, positions (depth and translation) and electrical properties (conductivity and permeability). Responses for spheres of fixed electrical properties located directly over the sensing element at varying depth and with varying diameter have been tabulated into depth-diameter measurement grids, allowing quick inversion from measured sensing element response (transimpedance) to depth-diameter parameters.

These models extend previous work by permitting interactions between multiple objects (spheres) and by permitting more realistic field calculations for the drive winding. The modeling approach here follows the approach of Braunisch *et al*[3] for distributions of conducting and permeable bodies of generic geometry in the presence of an imposed magnetoquasistatic field. The model accounts for the interactions of secondary fields generated by the objects. Solving this multi-region, arbitrary geometry problem with an exact analytic solution is currently impractical. Therefore the problem is simplified in several ways such that an approximate solution can be obtained.

The system is assumed to be magnetoquasistatic, which amounts to ignoring the wave nature of the fields by allowing the displacement current to be ignored in Maxwell's equations. The conductivity of the material separating the objects is assumed to be weakly conducting such that only the objects induce secondary magnetic fields. These two requirements can be expressed mathematically by requiring the magnitude of the complex wavelength to be much larger than the length scales of the system. The length scale of the system includes sizes of objects, distance to the sources, distance to observation points, and inter-object distance. The weakly conducting criteria also require the conductivity of the objects to be significantly larger than the background medium when the object has low permeability. Alternatively the permeability of the object should be significant for weakly conducting objects. Though difficult to quantify, this criteria helps assure that the object effect will be dominant over the diffusion effects.

The fields are also assumed to be spatially uniform over the region of each object. This requires the variation of the fields due to both the primary sources and due to the induced fields from neighboring objects, to be reasonably constant over the region of each object. The dominant

[1] N. Goldfine, A. Washabaugh, D. Schlicker, "High-Resolution Inductive Array Imaging of Buried Objects," SPIE AeroSense Conference, Orlando, FL; April 2000.

[2] N. Goldfine, D. Schlicker, A. Washabaugh, D. Clark, M. Zahn, "New Quasistatic Magnetic and Electric Field Imaging Arrays and Algorithms for Object Detection, Identification, and Discrimination," SPIE AeroSense Conference, Orlando, FL; April 1999. Proceedings vol. 3710; n.1, 1999, pp. 89-100.

[3] Henning Braunisch, Chi O. Ao, Kevin O'Neill, and Jin A. Kong, "Magnetoquasistatic Response of a Distibution of Small Conducting and Permeable Objects," Geoscience and Remote Sensing Symposium, 2000. Proceedings, vol. 4, 2000, pp. 1424-1426.

field from each object is assumed to be that of the far-field of a dipole. Most arbitrary objects would require higher order multipole responses for an exact representation, even with uniform excitation. Fortunately, these higher order poles have increasingly faster spatial decays and therefore can be neglected at sufficient distance. The dipole response has a derivative, which decays with distance and therefore becomes more spatially uniform. This allows the uniformity assumption to be achieved by forcing object spacing to be sufficiently large such that all higher pole responses are negligible and the dipole spatial dependence has slowed. Neglecting the higher order poles also requires that the fields only be observed at sufficient distance from the object, for objects which do not have a pure dipole response.

The sources induced in the objects are in general made up of both magnetization and diffusion currents. These currents are not necessarily in phase with the excitation field and therefore the dipole moment approximating these sources will be complex. The far field response of a z directed dipole located at the origin in spherical coordinates is as follows:

$$\overline{\mathbf{H}} = \frac{\mathbf{m}_z}{4\pi r^3}\left(2\cos\theta\mathbf{i}_r + \sin\theta\mathbf{i}_\theta\right)$$

(2)

By using the following Spherical-Cartesian coordinate relations:

$$x = r\sin\theta\cos\phi$$

$$y = r\sin\theta\sin\phi$$

$$z = r\cos\theta$$

(3)

$$\mathbf{i}_r = \sin\theta\cos\phi\mathbf{i}_x + \sin\theta\sin\phi\mathbf{i}_y + \cos\theta\mathbf{i}_z$$

$$\mathbf{i}_\theta = \cos\theta\cos\phi\mathbf{i}_x + \cos\theta\sin\phi\mathbf{i}_y - \sin\theta\mathbf{i}_z$$

Eq. (2) can be expressed as:

$$\overline{\mathbf{H}} = \frac{\mathbf{m}_z}{4\pi r^3}\left[3\left(\frac{x}{r}\frac{z}{r}\mathbf{i}_x + \frac{y}{r}\frac{z}{r}\mathbf{i}_y + \frac{z}{r}\frac{z}{r}\mathbf{i}_z\right) - \mathbf{i}_z\right]$$

(4)

The dipole moment of an object may have any orientation, subject to imposed fields and additional relations, which can be broken down into its mutually orthogonal components. The fields from the two additional components can be obtained simply by applying the following coordinate rotations to Eq. (4):

$$z \to x, \mathbf{i}_z \to \mathbf{i}_x \qquad z \to y, \mathbf{i}_z \to \mathbf{i}_y$$

$$y \to y, \mathbf{i}_y \to \mathbf{i}_y \qquad x \to x, \mathbf{i}_x \to \mathbf{i}_x$$

(5)

$$x \to z, \mathbf{i}_x \to -\mathbf{i}_z \qquad y \to z, \mathbf{i}_y \to -\mathbf{i}_z$$

The location of the dipole can be shifted to a location $\overline{r}_n = x_n\mathbf{i}_x + y_n\mathbf{i}_y + z_n\mathbf{i}_z$ while the fields are observed at $\overline{r}_m = x_m\mathbf{i}_x + y_m\mathbf{i}_y + z_m\mathbf{i}_z$ so that:

$$x = x_m - x_n, y = y_m - y_n, z = z_m - z_n$$

(6)

After applying the coordinate rotations, shifts, and summing the fields from each component of the dipole moment, the total H-field can be decomposed into components as follows:

$$\mathbf{H}_x = \frac{1}{4\pi r^3}\left[\mathbf{m}_x\left(3\frac{(x_m - x_n)}{r}\frac{(x_m - x_n)}{r} - 1\right) + 3\mathbf{m}_y\frac{(x_m - x_n)}{r}\frac{(y_m - y_n)}{r} + 3\mathbf{m}_z\frac{(x_m - x_n)}{r}\frac{(z_m - z_n)}{r}\right]$$

(7)

$$\mathbf{H}_y = \frac{1}{4\pi r^3}\left[3\mathbf{m}_x \frac{(y_m - y_n)}{r}\frac{(x_m - x_n)}{r} + \mathbf{m}_y\left(3\frac{(y_m - y_n)}{r}\frac{(y_m - y_n)}{r} - 1\right) + 3\mathbf{m}_z \frac{(y_m - y_n)}{r}\frac{(z_m - z_n)}{r}\right] \tag{8}$$

$$\mathbf{H}_z = \frac{1}{4\pi r^3}\left[3\mathbf{m}_x \frac{(z_m - z_n)}{r}\frac{(x_m - x_n)}{r} + 3\mathbf{m}_y \frac{(z_m - z_n)}{r}\frac{(y_m - y_n)}{r} + \mathbf{m}_z\left(3\frac{(z_m - z_n)}{r}\frac{(z_m - z_n)}{r} - 1\right)\right] \tag{9}$$

where

$$r = \left|\vec{r}_m - \vec{r}_n\right| \tag{10}$$

which is written compactly as:

$$\overline{\mathbf{H}}_n\left(\vec{r}_m\right) = \frac{3\left(\mathbf{i}_{mn}\right)^T \mathbf{i}_{mn} - \overline{\overline{I}}}{4\pi r_{mn}^3}\cdot\overline{\mathbf{m}}_n \tag{11}$$

where

$$\mathbf{i}_{mn} = \left(\vec{r}_m - \vec{r}_n\right)/r_{mn} \quad ; \quad r_{mn} = \left|\vec{r}_m - \vec{r}_n\right| \tag{12}$$

Eq. (11) is utilized in determining the contribution to the fields at object m of object n based on object n's effective dipole moment $\overline{\mathbf{m}}_n$.

The effective dipole moment of an object is dependent on the magnetization and diffusion currents present in the object, which are due to the external excitation fields. Since these excitation fields have been assumed uniform over the object's volume and the resulting fields from each object is described by a net dipole moment, a polarizability tensor can be used to relate the fields to the dipole moment. The generic polarizability tensor has the form below where the elements of the tensor $\overline{\overline{M}}$ may be complex due to the phase of the object's induced current. Since diffusion effects will be frequency dependent and the objects permeability may be dispersive, the tensor may also be a function of frequency.

$$\begin{bmatrix} \mathbf{m}_x \\ \mathbf{m}_y \\ \mathbf{m}_z \end{bmatrix} = \begin{bmatrix} \mathbf{M}_{xx} & \mathbf{M}_{xy} & \mathbf{M}_{xz} \\ \mathbf{M}_{yx} & \mathbf{M}_{yy} & \mathbf{M}_{yz} \\ \mathbf{M}_{zx} & \mathbf{M}_{zy} & \mathbf{M}_{zz} \end{bmatrix}\begin{bmatrix} \mathbf{H}_x \\ \mathbf{H}_y \\ \mathbf{H}_z \end{bmatrix} \tag{13}$$

Each column of $\overline{\overline{M}}$ represents the dipole moment that would be excited by uniform magnetic field in the corresponding coordinate vector direction. Performing the matrix multiplication on the right essential superimposes the individual moments excited by each vector component of the field.

The polarizability tensor for an object can be determined in several ways. Some geometries such as spheres and spheroids allow for analytic solution. Other more complex geometries may utilize numerical techniques such as MAS (Method of Auxiliary Sources), TSA (Thin Skin Approximation), BEM (boundary integral method), or FEM. Instruments can also be setup to determine the polarizability tensor empirically, allowing characteristics of objects which may be difficult to simulate, to be captured. All these techniques allow a library of tensors to be compiled, which can be quickly accessed even if the initial computation or measurement required significant time.

The relations for the fields induced by the objects' dipole moments and the relation for the objects' dipole moments induced by the fields can now be applied for each object within the system. The primary magnetic fields, from the sources external to the objects, needs to be

specified at each object location. The only requirement is that again these fields are approximately uniform over the region of each object. It is also assumed that the secondary object fields will not affect the sources of the primary field.

At each object location the polarization tensor relates the total magnetic field at the objects location to the object's induced dipole moment by Eq. (13). The total field at an object's location is the sum of the contributions from the primary field and all other objects. In block matrix notation the equation is:

$$
\begin{bmatrix} \bar{m}_1 \\ \vdots \\ \bar{m}_N \end{bmatrix} = \begin{bmatrix} \bar{\bar{M}}_1 & 0 & 0 \\ 0 & \ddots & 0 \\ 0 & 0 & \bar{\bar{M}}_N \end{bmatrix} \left(\begin{bmatrix} \bar{H}_i(\bar{r}_1) \\ \vdots \\ \bar{H}_i(\bar{r}_N) \end{bmatrix} + \begin{bmatrix} 0 & \bar{\bar{h}}_2(\bar{r}_1) & \cdots & \bar{\bar{h}}_N(\bar{r}_1) \\ \bar{\bar{h}}_1(\bar{r}_2) & 0 & \ddots & \vdots \\ \vdots & \ddots & 0 & \bar{\bar{h}}_N(\bar{r}_{(N-1)}) \\ \bar{\bar{h}}_1(\bar{r}_N) & \cdots & \bar{\bar{h}}_{(N-1)}(\bar{r}_N) & 0 \end{bmatrix} \begin{bmatrix} \bar{m}_1 \\ \vdots \\ \bar{m}_N \end{bmatrix} \right) \quad (14)
$$

where, $\bar{H}_i(\bar{r}_n)$ is the incident (primary) field at location $\bar{r}_n$ of the nth object, $\bar{m}_n$ is the dipole moment of the nth object, $\bar{\bar{M}}_n$ is the polarization tensor of the nth object, and

$$
\bar{\bar{h}}_n(\bar{r}_m) = \frac{3(i_{mn})^T i_{mn} - \bar{\bar{I}}}{4\pi r_{mn}^3} \quad (15)
$$

is a tensor relating the magnetic field at location $\bar{r}_m$ to a dipole at $\bar{r}_n$. The zeros in the matrix, containing the polarization tensors, are present because the dipole moment for each object is not directly dependent on the fields at other object locations. The zeros in the matrix containing the $\bar{\bar{h}}_n(\bar{r}_m)$ are present because the induced dipole moment for each object only contributes to the field for other objects and not the object itself. The solution is now obtained by rearranging Eq. (14) into the standard $Ax = b$ form of Eq. (15) and solving for the dipole moments of the objects.

$$
\begin{bmatrix} 1 & -\bar{\bar{M}}_1\bar{\bar{h}}_2(\bar{r}_1) & \cdots & -\bar{\bar{M}}_1\bar{\bar{h}}_N(\bar{r}_1) \\ -\bar{\bar{M}}_2\bar{\bar{h}}_1(\bar{r}_2) & 1 & \ddots & \vdots \\ \vdots & \ddots & 1 & -\bar{\bar{M}}_{(N-1)}\bar{\bar{h}}_N(\bar{r}_{N-1}) \\ -\bar{\bar{M}}_N\bar{\bar{h}}_1(\bar{r}_N) & \cdots & -\bar{\bar{M}}_N\bar{\bar{h}}_{(N-1)}(\bar{r}_N) & 1 \end{bmatrix} \begin{bmatrix} \bar{m}_1 \\ \vdots \\ \bar{m}_N \end{bmatrix} = \begin{bmatrix} \bar{\bar{M}}_1\bar{H}_i(\bar{r}_1) \\ \vdots \\ \bar{\bar{M}}_N\bar{H}_i(\bar{r}_N) \end{bmatrix} \quad (16)
$$

For computational purposes it is useful to note that $\bar{\bar{h}}_n(\bar{r}_m) = \bar{\bar{h}}_m(\bar{r}_n)$. It is also useful to examine the affects of changing system parameters on the system equation, for the purpose of optimizing computation during parametric sweeps. The following table summarizes the quantities effected by changing the listed properties and whether the A matrix and/or b vector of Eq. (19), in $Ax = b$ form, is affected and to what extent.

In all cases the "b vector" is affected, while others only require a change to the "A matrix" and in many cases only part of the elements will need to be recalculated. Even in the cases where all elements need recalculation, many of the components of the products that appear in the elements of Eq. (16), can be stored to reduce repetitive computation during parameter sweeps.

Once the dipole moments have been solved, it is a simple matter to determine the total field at any location $\bar{r}$. This is accomplished by applying Eq. (11) with $\bar{r}_m = \bar{r}$ for each object and summing the resulting fields with the primary field at $\bar{r}$.

Parameter Changed	Affected Quantities	A Matrix Affected	b Vector Affected
nth Object Location	$\bar{\bar{h}}_n(\bar{r}_m),\ \bar{H}_i(\bar{r}_n)$	Part	Part
nth Object Property	$\bar{\bar{M}}_n$	Part	Part
Primary Source Change	$\bar{H}_i(\bar{r}_n)$	None	All
Equal Translation of All Objects	$\bar{H}_i(\bar{r}_n)$	None	All
Frequency	$\bar{\bar{M}}_n,\ \bar{H}_i(\bar{r}_n)*$	All**	All

$* \ \bar{H}_i(\bar{r}_n)$ is only changed if the primary source has a frequency dependence.

** Except for the obviously constant diagonal elements

Several simulations were performed to demonstrate the utility of the model and the effects of object interaction. In these simulations a square coil was chosen as a realistic and common excitation source. (A distributed drive winding has also been simulated with this method for generation of the measurement grids below.) Assuming that the wires are infinitely thin "current sticks" and carry a constant current, then the field can be determined from the Biot-Savart Law as[4]

$$\bar{H} = \frac{I}{4\pi} \frac{\bar{c} \times \bar{a}}{|\bar{c} \times \bar{a}|^2} \left(\frac{\bar{a} \cdot \bar{c}}{|\bar{c}|} - \frac{\bar{a} \cdot \bar{b}}{|\bar{b}|} \right) \tag{20}$$

where, I is the current in the current stick, $\bar{b}$ is a vector from the observation point to the start of the stick, $\bar{c}$ is a vector from the observation to the end of the stick and $\bar{a} = \bar{c} - \bar{b}$. The excitation field at each object location is obtained by summing the contribution from each of the four legs of the square coil.

Figure 7 shows the resulting induced or secondary magnetic field intensity parallel to the coil axis and at the center of the coil as the coil is scanned over one or more spheres. The excitation frequency was 15 kHz, the coil was a square with 10 cm sides, and the sphere conductivity was 10^7 S/m. The configurations considered were 1) a single 1 cm diameter sphere, 2) a single 1.48 cm diameter sphere, and 3) three 1 cm diameter spheres stacked vertically with a 3 cm center-to-center distance. The effects of ignoring the interactions are especially noticeable in the imaginary part of the response. The size of the large sphere was choosen to produce a real response equal to that of the three interacting smaller spheres. **The imaginary response is very different though between these two configurations, indicating that there is information that can be used to discriminate between a large object and multiple smaller objects (e.g., using a Grid Method or other model based approach).**

---

[4] H.A. Haus and J.R Melcher, "Electromagnetic Fields and Energy," Prentice Hall, Englewood Cliffs, NJ, 1989.
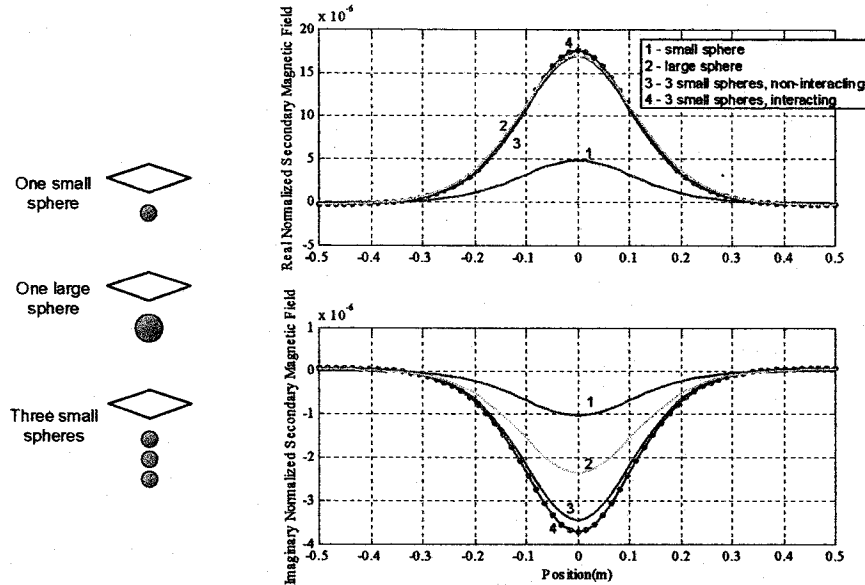
Figure 7. Real and imaginary induced magnetic field for several sphere configurations translated across a square coil operating at 15 kHz.

Another model has been explored as a method for determining the secondary magnetic fields produced by a sphere excited by a locally uniform time harmonic magnetic field. This model follows the approach of Wait[5] and is not limited to the purely magnetoquasistatic situation. The restriction on the conductivity of the region external to the sphere is also less severe, which allows some degree of magnetic diffusion in the external region to be accounted for. The restriction placed on the conductivity, frequency, and permeability of the external region is completely based on making the assumption of a locally uniform excitation field valid. This means that the spatial variation of the excitation due to both the wave nature of the fields and the diffusion affects needs to be small relative to the sphere. This is quantified in terms of the propagation constant and radius as $|\gamma_2 R| \ll 1$ where R is the radius of the sphere and the propagation constant is defined as

$$\gamma = \left(i\sigma\mu\omega - \varepsilon\mu\omega^2\right)^{1/2} \tag{21}$$

The subscript 2 refers to the quantities in the external region, while a subscript 1 refers the quantities inside the sphere. There is no restriction on the propagation constant on the sphere's interior since both the wave nature and the diffusion effects are fully accounted for in the solution.

To solve for the field distribution, the magnetic field is defined in terms of a vector potential $\bar{F}$ as:

$$\bar{H} = -(\sigma + i\omega\varepsilon)\bar{F} + \frac{1}{i\mu\omega}\nabla\left(\nabla\cdot\bar{F}\right) \tag{22}$$

---

[5] J.R. Wait, "A Conducting Sphere in a Time Varying Magnetic Field," *Geophysics*, vol. 16, no. 1, January 1951, pp. 666-672.

which differs from the more common vector potential representation of the magnetic flux density $\bar{B} = \nabla \times \bar{A}$. To better understand Eq. (22), consider Ampere's Law for time-harmonic fields in a source-free region of uniform anisotropic conductivity:

$$\nabla \times \bar{H} = \bar{J} + (i\omega\varepsilon)\bar{E} = (\sigma + i\omega\varepsilon)\bar{E} \tag{23}$$

Taking the curl of Eq. 22 results in

$$\nabla \times \bar{H} = -(\sigma + i\omega\varepsilon)\nabla \times \bar{F} \tag{24}$$

By comparison with Ampere's Law in Eq. (23) it can be seen that the vector potential $\bar{F}$ is related to the electric field by

$$\bar{E} = -\nabla \times \bar{F} \tag{25}$$

Any arbitrary solenoidal electric field can be described as the curl of another vector field in this way. Since the regions of interest are composed of uniform electrical properties and Eq. (25) guarantees that the electric field will be solenoidal; the requirement that there is neither volume charge nor any divergence in the current density will always be satisfied. From Eq. (24), $\bar{H}$ and $\bar{F}$ can only be equated to each other within the gradient of a scalar potential and a constant, which has been set to zero, as:

$$\bar{H} = -(\sigma + i\omega\varepsilon)\bar{F} + \nabla U \tag{26}$$

The divergence of $\bar{H}$ must be zero in the region of constant magnetic permeability, while the divergence of $\bar{F}$ has yet to be defined. With $\bar{E}$ and $\bar{H}$ related to $\bar{F}$ and U by Eq. (25) and Eq. (26), Ampere's Law is always satisfied. Faraday's Law for time-harmonic fields is as follows:

$$\nabla \times \bar{E} = -i\omega\mu\bar{H} \tag{27}$$

Substitution into Faraday's Law and the application of a vector identity for $\nabla \times \nabla \times \bar{F}$ results in:

$$\nabla^2 \bar{F} - \nabla\left(\nabla \cdot \bar{F}\right) = \gamma^2 \bar{F} - i\omega\mu\nabla U \tag{28}$$

Since the divergence of $\bar{F}$ can be defined in terms of the scalar U as:

$$U \equiv \frac{1}{i\mu\omega}\nabla \cdot \bar{F} \tag{29}$$

Eq. (28) simplifies to

$$\nabla^2 \bar{F} = \gamma^2 \bar{F} \tag{30}$$

which is a single differential equation for the vector $\bar{F}$ in each region. However, before proceeding with the solution, the problem can be further simplified by analyzing the required components of $\bar{F}$ based on the symmetry of the problem and boundary conditions that must be met.

The imposed field is assumed as uniform and z directed and therefore contains only $\hat{r}$ and $\hat{\theta}$ components. Since the fields are rotationally symmetric about the z axis all derivatives with respect to $\hat{\phi}$ will be zero. Therefore by using Ampere's Law in spherical coordinates it can be shown that it is necessary for the electric field to contain a $\hat{\phi}$ component in order to satisfy normal and tangential boundary conditions. Faraday's Law can also be applied to an electric field with only a $\hat{\phi}$ component, which in combination with the axial symmetry, produces a magnetic field with only $\hat{r}$ and $\hat{\theta}$ components. It is therefore reasonable to assume that a valid solution can be found with a $\hat{\phi}$ directed electric field. By analyzing Eq. (25), it can be shown that the vector $\bar{F}$ must contain an $\hat{r}$ or $\hat{\theta}$ component in spherical coordinates, or a $\hat{\rho}$ or $\hat{z}$

component in cylindrical coordinates, in order for the associated electric field to contain a $\hat{\phi}$ component.

For a solution, it is convenient to choose an $\overline{F}$ vector with a $\hat{z}$ component, even though it may seem more preferable to choose an $\overline{F}$ vector with spherical components rather than cylindrical components. However, the choice of spherical components can be shown to make the problem more complex since the vector Laplacian of (30) in spherical coordinates results in multiple vector components. This is true even in the case where $\overline{F}$ contains only a single spherical component. Solving the problem completely in cylindrical coordinates would also prove to be difficult since the surface on which the boundary conditions are to be imposed is described more simply in spherical coordinates as is the normal and tangential components of the field on the boundary. Consequently both spherical and cylindrical coordinate systems are used by assuming an $\overline{F}$ vector solution of the form

$$\overline{F} = F_z(r,\theta)\hat{z} \tag{31}$$

This expression can now be substituted into equation Eq. (30) and the vector operators applied to produce

$$\frac{1}{\rho}\frac{\partial}{\partial\rho}\left(\rho\frac{\partial F_z}{\partial\rho}\right) + \frac{\partial^2 F_z}{\partial z} = \gamma^2 F_z \tag{32}$$

Since the partial derivatives are with respect to cylindrical coordinates, but F_z is a function of spherical coordinates, the chain rule must be applied using the following partial derivative relations between cylindrical and spherical coordinate systems

$$\frac{\partial r}{\partial\rho} = \sin\theta, \quad \frac{\partial r}{\partial z} = \cos\theta, \quad \frac{\partial\theta}{\partial\rho} = \frac{\cos\theta}{r}, \quad \frac{\partial\theta}{\partial z} = -\frac{\sin\theta}{r} \tag{33}$$

This results in

$$r^2\frac{\partial^2 F_z}{\partial r^2} + 2r\frac{\partial F_z}{\partial r} - r^2\gamma^2 F_z = -\frac{\partial^2 F_z}{\partial\theta^2} - \cot\theta\frac{\partial F_z}{\partial\theta} \tag{34}$$

This can be converted into two regular differential equations by separation of variables, with

$$F_z(r,\theta) = F_r(r)F_\theta(\cos\theta) \tag{35}$$

The first differential equation, which has solutions related to Bessel functions, is

$$r^2 F_r''(r) + 2rF_r'(r) - \left(r^2\gamma^2 + n(n+1)\right)F_r(r) = 0 \tag{36}$$

The second, which is Legendre's Equation, is

$$\left(1-x^2\right)F_\theta''(x) - 2xF_\theta'(x) + n(n+1)F_\theta(x) = 0 \tag{37}$$

where $x = \cos\theta$. The solutions to these two differential equations, in the form of product solutions for F_z are

$$F_z(r,\theta) \propto \begin{array}{c} \dfrac{\hat{I}_n(\gamma r)}{r}P_n(\cos\theta) \\[2ex] \dfrac{\hat{K}_n(\gamma r)}{r}P_n(\cos\theta) \end{array} \tag{38}$$

with $\hat{I}_n(\gamma r)$ and $\hat{K}_n(\gamma r)$ defined in terms of the standard Bessel Functions as

$$\hat{I}_n(\gamma r) = \sqrt{\pi\gamma r/2}\, I_{n+\frac{1}{2}}(\gamma r) \qquad (39)$$

and

$$\hat{K}_n(\gamma r) = \sqrt{2\gamma r/\pi}\, K_{n+\frac{1}{2}}(\gamma r) \qquad (40)$$

In the vicinity of the sphere the excitation has been assumed as a uniform z directed magnetic field of magnitude H_0. This can be related to the $\overline{F}$ vector using Eq. (22) as

$$\overline{F}_0 = F_0\hat{z} = -\frac{1}{(\sigma_2 + i\omega\varepsilon_2)}H_0\hat{z} \qquad (41)$$

The subscript 2 is used on the electrical properties to indicate the region exterior to the sphere. Therefore this is the representation of the locally uniform excitation fields by the $\overline{F}$ vector, valid in the exterior region.

The total $\overline{F}$ vector on the interior of the sphere can now be expressed as a superposition of the solutions to Eq. (32), which have no singularities at the origin and weighted with yet undetermined coefficients b_n as

$$\overline{F}_1 = F_1(r,\theta)\hat{z} = \sum_{n=0}^{\infty} b_n \frac{\hat{I}_n(\gamma_1 r)}{r} P_n(\cos\theta) i\mu_1\omega\hat{z} \qquad (42)$$

where the subscript 1 indicates parameters on the interior of the sphere. The total $\overline{F}$ vector on the exterior of the sphere can be expressed as the superposition of the solutions to Eq. (32), which have no singularities at infinity and weighted with yet undetermined coefficients a_n, and the excitation $\overline{F}$ vector of Eq. (41) as

$$\overline{F}_2 = F_2(r,\theta)\hat{z} = \left[\sum_{n=0}^{\infty} a_n \frac{\hat{K}_n(\gamma_2 r)}{r} P_n(\cos\theta) i\mu_2\omega\right]\hat{z} - \frac{1}{(\sigma_2 + i\omega\varepsilon_2)}H_0\hat{z} \qquad (43)$$

In order to determine the coefficients a_n and b_n, Eqs. (42) and (43) must satisfy the boundary condition on the surface of the sphere. The boundary conditions require continuity of normal magnetic flux density and continuity of the tangential magnetic field expressed respectively as

$$\hat{r}\cdot(\mu_1\overline{H}_1 - \mu_2\overline{H}_2)\big|_{r=R} = 0 \qquad (44)$$

$$\hat{r}\times(\overline{H}_1 - \overline{H}_2)\big|_{r=R} = 0 \qquad (45)$$

In order to apply the boundary conditions, the magnetic field must be determined from Eq. (22) in terms of F_z. Since the spherical components of the magnetic fields are desired in the evaluation of Eqs. (44) and (45), $\overline{F}$ is first represented in spherical components as $\overline{F} = F_z\cos\theta\hat{r} - F_z\sin\theta\hat{\theta}$ after which Eq. (22) can be evaluated as

$$\overline{H} = \left[-\gamma^2\cos\theta F_z + \cos\theta\frac{\partial^2 F_z}{\partial r^2} - \frac{\sin\theta}{r}\frac{\partial^2 F_z}{\partial r\partial\theta} + \frac{\sin\theta}{r^2}\frac{\partial F_z}{\partial\theta}\right]\frac{1}{i\mu\omega}\hat{r}$$
$$+ \left[\gamma^2\sin\theta F_z - \frac{\sin\theta}{r}\frac{\partial F_z}{\partial r} + \frac{\cos\theta}{r}\frac{\partial^2 F_z}{\partial r\partial\theta} - \frac{\sin\theta}{r^2}\frac{\partial^2 F_z}{\partial\theta^2}\right]\frac{1}{i\mu\omega}\hat{\theta} \qquad (46)$$

On the surface of the sphere at $r = R$ the source fields have an $\hat{r}$ component with a $\cos\theta$ dependence and a $\hat{\theta}$ component with a $\sin\theta$ dependence. It can be shown by substituting either Eq. (42) or (43) into Eq. (46), that only the $n = 0$ terms of the series have the correct θ dependence at $r = R$, and are the only terms required for the solution. Since $P_0(\cos\theta) = 1$, F_z has no θ dependence and all of the terms in Eq. (46) that contain partial derivative with respect to θ can be removed. By utilizing Eqs. (44), (45), and (46) the boundary condition can be expressed as

$$\left[\frac{\partial^2 F_1}{\partial r^2} - \gamma_1^2 F_1\right] = \left[\frac{\partial^2 F_2}{\partial r^2} - \gamma_2^2 F_2\right]$$

$$\frac{1}{\mu_1}\left[\frac{1}{r}\frac{\partial F_1}{\partial r} - \gamma_1^2 F_1\right] = \frac{1}{\mu_2}\left[\frac{1}{r}\frac{\partial F_2}{\partial r} - \gamma_2^2 F_2\right]\Bigg|_{r=R} \qquad (47)$$

The coefficients a_0 and b_0 can now be determined by simultaneously solving the equations produced by substituting Eqs. (42) and (43) into Eq. (47) and eliminating terms containing positive powers of $(\gamma_2 R)$, which are assumed to be much less than one. The resulting coefficients are

$$a_0 = \frac{R^3 H_0}{\hat{K}_0(\gamma_2 R)}\left[\frac{\mu_1\alpha^2\hat{I}_0''(\alpha) - (2\mu_1 + \mu_2)\alpha\hat{I}_0'(\alpha) + (2\mu_1 + \mu_2)\hat{I}_0(\alpha) - (\mu_1 - \mu_2)\alpha^2\hat{I}_0(\alpha)}{\mu_1\alpha^2\hat{I}_0''(\alpha) - 2(\mu_1 - \mu_2)\alpha\hat{I}_0'(\alpha) + 2(\mu_1 - \mu_2)\hat{I}_0(\alpha) - (\mu_1 + 2\mu_2)\alpha^2\hat{I}_0(\alpha)}\right] \qquad (48)$$

$$b_0 = R^3 H_0\left[\frac{3\mu_2}{\mu_1\alpha^2\hat{I}_0''(\alpha) - 2(\mu_1 - \mu_2)\alpha\hat{I}_0'(\alpha) + 2(\mu_1 - \mu_2)\hat{I}_0(\alpha) - (\mu_1 + 2\mu_2)\alpha^2\hat{I}_0(\alpha)}\right] \qquad (49)$$

where $\alpha = \gamma_1 R$. The functions $\hat{I}_0$ and $\hat{K}_0$ can be represented in terms of hyperbolic and exponential functions[6] as

$$\hat{I}_0(z) = \sinh(z) \qquad (50)$$

$$\hat{K}_0(z) = e^{-z} \qquad (51)$$

These can be used to further simplify the coefficients to:

$$a_0 = H_0 R^3\left[\frac{2\mu_1(\sinh\alpha - \alpha\cosh\alpha) + \mu_2(\sinh\alpha - \alpha\cosh\alpha + \alpha^2\sinh\alpha)}{2\mu_1(\sinh\alpha - \alpha\cosh\alpha) - 2\mu_2(\sinh\alpha - \alpha\cosh\alpha + \alpha^2\sinh\alpha)}\right] \qquad (52)$$

$$b_0 = H_0 R^3\left[\frac{3\mu_2}{2\mu_1(\sinh\alpha - \alpha\cosh\alpha) - 2\mu_2(\sinh\alpha - \alpha\cosh\alpha + \alpha^2\sinh\alpha)}\right] \qquad (53)$$

The magnetic fields on both the interior and exterior of the sphere can be evaluated by utilizing relations (50) and (51) in Eqs. (42) and (43) for $\bar{F}_1$ and $\bar{F}_2$, independently substituting these expressions into Eq. (46), and further expressing them in cylindrical coordinates to produce:

---

[6] Abramowitz, Milton, and Irene A. Stegan, *Handbook of Mathematical Functions*, Dover Publications, 1964, pp. 443-444.

$$\bar{H}_1 = b_0 \frac{\rho z}{r^5}\left[\sinh\beta_1\left(\beta_1^2 + 3\right) - 3\beta_1\cosh\beta_1\right]\hat{\rho}$$

$$+ b_0 \frac{1}{r^3}\left[\left(\frac{3z^2}{r^2} - 1\right)\left(\sinh\beta_1 - \beta_1\cosh\beta_1\right) - \frac{\rho^2}{r^2}\beta_1^2\sinh\beta_1\right]\hat{z} \qquad (54)$$

$$\bar{H}_2 = a_0 e^{-\beta_2}\frac{\rho z}{r^5}\left(\beta_2^2 + 3\beta_2 + 3\right)\hat{\rho} + a_0 e^{-\beta_2}\frac{1}{r^3}\left[\left(\frac{3z^2}{r^2} - 1\right)\left(\beta_2 + 1\right) - \frac{\rho^2\beta_2^2}{r^2}\right]\hat{z} \qquad (55)$$

where $\beta_1 = \gamma_1 r$ and $\beta_2 = \gamma_2 r$. The single $\hat{\phi}$ component of the electric field can also be evaluated from $\bar{F}_1$ and $\bar{F}_2$ by using Eq. 25 and expressing the results in cylindrical coordinates as follows

$$E_{1\phi} = b_0 i\mu_1\omega\frac{\rho}{r^3}\left[\beta_1\cosh\beta_1 - \sinh\beta_1\right] \qquad (56)$$

$$E_{2\phi} = -a_0 i\mu_2\omega\frac{\rho}{r^3}e^{-\beta_2}\left[\beta_2 + 1\right] \qquad (57)$$

This model can then be used to plot the magnetic field lines or induced current densities resulting from the simulated response of a sphere. The following simulations assumed a sphere of radius 5 cm, conductivity 10^5 S/m, relative permeability 1, and relative permittivity 1. They also assumed an external medium of conductivity 0, relative permeability 1, and relative permittivity 1. The frequency was assumed to be 15 kHz, and the primary field amplitude was assumed to be 1 A/m. This results in a skin depth which is approximately one quarter of the sphere's radius. It should also be noted that even though the displacement currents were not explicitly set to zero (i.e., $\varepsilon_1 = \varepsilon_2 = 0$), their affect on the fields and the currents in the region plotted, is negligible.

The plots in Figure 8 through Figure 11 show the magnetic field lines for the total field (primary and secondary) and the internal current densities for a cross-section of the sphere. Each set of plots shows the field lines and current distribution for a particular phase of the periodic cycle in increments of $\pi/4$ radians. The plots only include the phases: $\omega t = 0, \pi/4, \pi/2, 3\pi/4$, however the cycle is completed by simply reversing the field and current directions of the first four phases.

The general cyclic behavior of the current can be visualized as a movement of a concentration of ϕ directed current, originating at the surface, into the sphere. These surface currents tend to form a pocket of current as they move inward toward the sphere's center, while simultaneously becoming more diffuse. The magnetic fields tend to circulate around these pockets of current and also move inward until the centers of the circulations connect and the cycle repeats. Figure 10 ($\omega t = \pi/2$) has a magnetic field distribution similar to that associated with a dipole field, which appears significantly different from the other phases plotted. This is a result of the primary field intensity being zero for $\omega t = \pi/2, 3\pi/2$, while the secondary fields are generated from the circulating eddy currents which would appear as the fields from a loop or dipole.
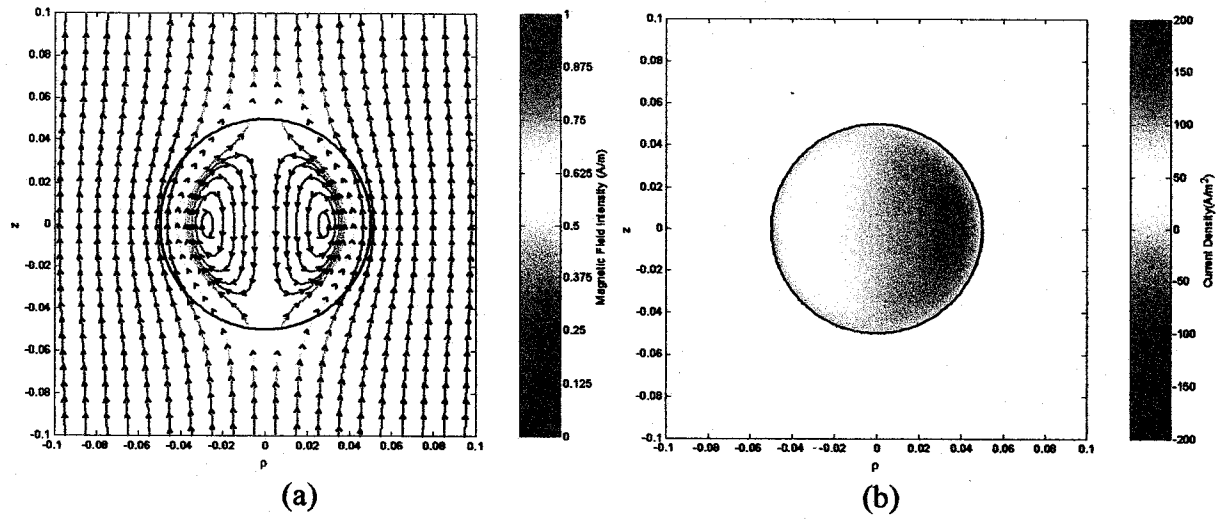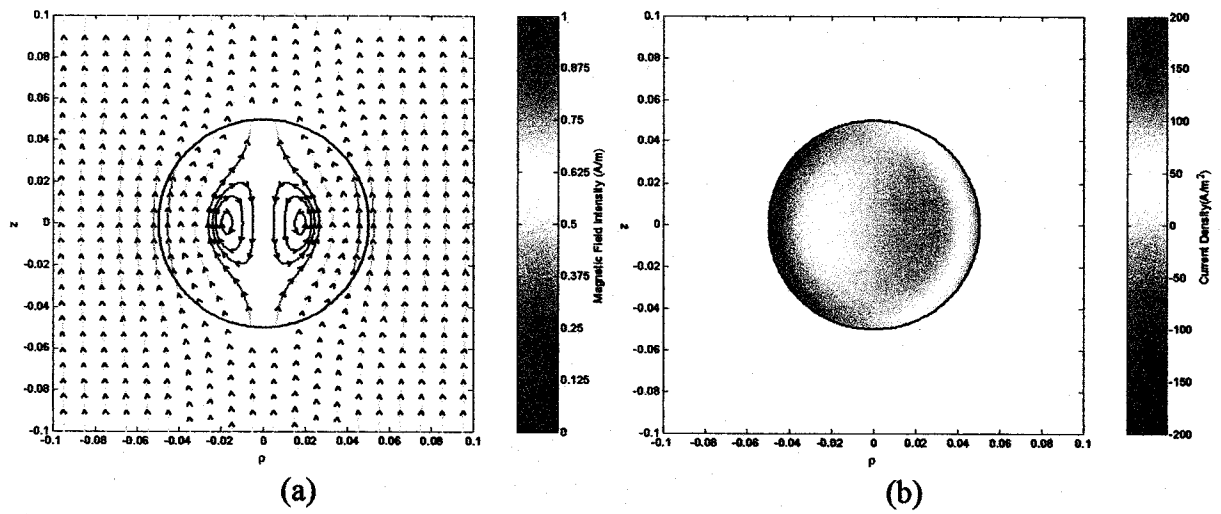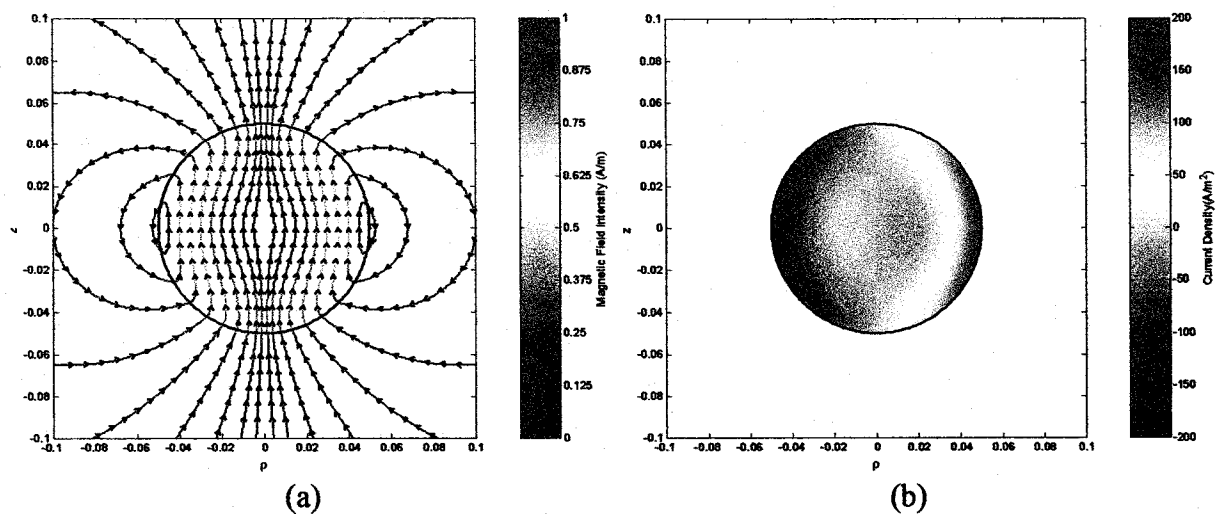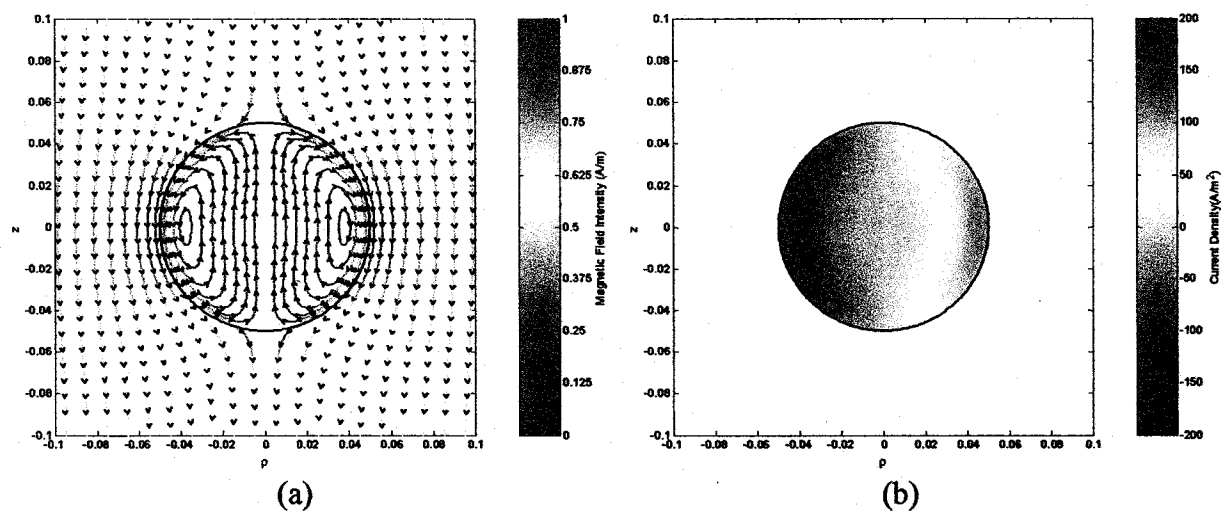
Figure 8. Simulated magnetic field lines (a) and current density (b) for a nonmagnetic conducting sphere in a locally uniform imposed magnetic field at a fixed phase ($\omega t=0$) of the periodic excitation cycle.

Figure 9. Simulated magnetic field lines (a) and current density (b) for a nonmagnetic conducting sphere in a locally uniform imposed magnetic field at a fixed phase ($\omega t=\pi/4$) of the periodic excitation cycle.

Figure 10. Simulated magnetic field lines (a) and current density (b) for a nonmagnetic conducting sphere in a locally uniform imposed magnetic field at a fixed phase ($\omega t = \pi/2$) of the periodic excitation cycle.

Figure 11. Simulated magnetic field lines (a) and current density (b) for a nonmagnetic conducting sphere in a locally uniform imposed magnetic field at a fixed phase ($\omega t = 3\pi/4$) of the periodic excitation cycle.

Laboratory Tests

Numerous tests were performed in a laboratory setting to demonstrate the basic operation of the sensor and grid measurement methods. Initial validation of the models for the sensor response and for the imaging approach was obtained through testing over known objects. These tests included measurements over aluminum spheres and known UXO.

Initial testing was performed on an assortment of aluminum spheres ranging from 3.8 to 20.3 cm (1.5 to 8 in.) in diameter in addition to representative munitions and clutter. **Since an existing drive winding was used in this program, which has a depth limitation of roughly 0.45 m (18 in.), including the standoff distance to the ground surface, the focus has been on objects located within approximately 0.4 m (16 in.) of the surface.** Since only the smaller UXO were within this depth at the Aberdeen Proving Grounds Test Site, only the smaller UXO were ordered. A new drive is to be designed in the follow-on effort to extend depth of sensitivity to greater than 0.6 m (24 in.) with a goal of a 0.9 m (36 in.) depth of sensitivity. (Note that the object or sphere size has not yet been determined for this requirement.)

Figure 12 shows representative scans of objects over the older version of the array (with 8 sensing elements). These scans simulated a scan rate of approximately 1.2 m/sec (4 ft/sec) and a distance to the array of 15 cm (6 in.). The bomblet appears as a discrete object while the dimensions of the cylinder are large compared to the width of the array. Even in this simple case, the image readily shows the shape and differences for the two objects and the orientation variation for the cylinder. The non-uniformity of the cylinder image is attributed to the variations in the magnetic field intensity across the array. This can be corrected with model-based methods that correctly account for the field variations at the sides of the drive winding, by widening the drive winding, or by improving the drive winding designs to reduce this field variation.

Figure 13 shows the data and measurement grids from one of the channels beneath the object. This grid was generated for the bomblet using the revised sphere model and illustrates how the bomblet properties (size and depth) can be estimated from the grid. The cylinder data does not even fall on the grid. This illustrates the basic capability for object identification/discrimination and clutter suppression but more robust procedures still need to be developed. For example, different measurement grids need to be used for the different sensing elements to account for the variations in the magnetic field intensity across the array.
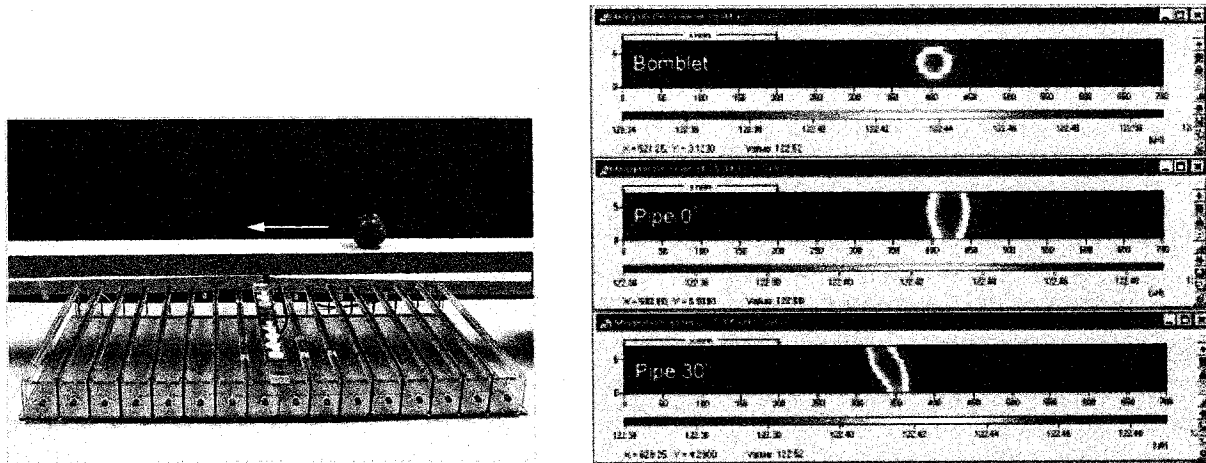
Figure 12. Representative images of data taken with the old array.
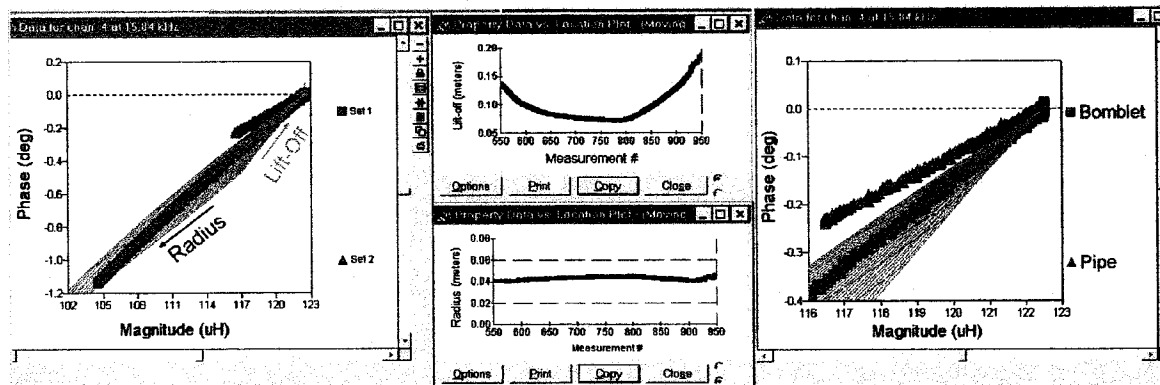
Figure 13. Representative measurement grid, data, and depth/size estimates for a bomblet and cylinder scanned across the "old" sense coil.

After fabrication of the higher resolution array of sense elements and integration with the impedance measurement instrumentation, tests were performed on single objects at various locations beneath the sensor array. Figure 14 shows the basic configuration for the array along with the numbering for the sense elements and the locations of the aluminum spheres. Tests were also performed with 0.9 m (36 in.) long pipes and several UXO.

Figure 15 shows the response of several sense elements as different size aluminum spheres are lowered beneath sense element 8. The model was used to calculate an appropriate measurement grid for the sphere location and properties (e.g., size and electrical conductivity) and for the sense element position and orientation within the drive winding. When the sense element is directly over the object, in this case element 8, the grid indicates reasonable sensitivity to the size and depth of the object, as indicated by the relatively large spacing between the grid lines. For each sphere, the model and data show a nonlinear response and the data follows a line of constant size as the depth is varied. The response of offset sense elements, in this case elements 4 and 12, show similar behavior to sense element 8, but with a reduced sensitivity to the object properties. This indicates that the adjacent sense elements provide complementary information about the object properties. The data does not fall on the grids for these preliminary

measurements because the sphere location beneath the sense elements was only controlled by hand, the thickness of the sphere walls is not accounted for in the model and the model does not currently account for the field variations over the footprint of the sense elements. However, even so, the data is relatively close to the grid and follows predicted behavior as lift-off is varied.

In this case, the measurement grid is plotted as the imaginary part of the signal against the real part of the signal. This is more convenient (in some cases) than the magnitude and phase for data plotting, particularly when the measurement signal is small and comparable to the measurement noise. This is because the drive winding enhancement shifts the air point to the origin and measurement noise, particularly near the air point, can give rise to any phase angle between -180 and +180 degrees. The result is a spread of data points over all phase angles, for small magnitudes, instead of a clustering of data points near the origin. Plots of the magnitude itself are still convenient, though, since it combines the real and imaginary parts of the signal into a single value that can be displayed.

Figure 16 shows the estimated properties obtained from sense element 8 as aluminum spheres of different size are lower beneath it. The depth estimates are generally within approximately 2 cm to a depth of approximately 20 cm, which is where the noise in the measurements causes some of the data to fall off of the measurement grid and the standard deviation of the measurement, indicated by the vertical error bars, increases substantially. The associated estimates of the sphere sizes are in reasonable agreement with the known sphere sizes for shallow depths. These estimates become less reliable at depths of around 20 cm because of the decay of the imposed magnetic field intensity with depth. Use of a larger drive winding wavelength would reduce this decay, extending the field depth of penetration. Also, better size estimates at deeper depths possible with the larger objects. Figure 17 shows the sensor response and measurement grids for spheres beneath sense elements that are closer to the edges of the array. Similar to Figure 15, there is good sensitivity to both the sphere size and depth.

Figure 18 shows the effect of an offset of the sphere on the measurement response. This would typically result from a scan of an array over an object or when sense elements are placed at various locations within the footprint of the drive winding and exposed to different magnetic field intensities. In this case, the aluminum spheres are offset by 15.2 cm (6 in.) on either side of the linear row of sense elements (y direction), but aligned with sense element 8 in the x direction. The measurement grids, which account for the offset in object and sense element positions, indicate that the response should be symmetric, since the sense elements are placed at the center of the drive winding construct. However, the data is not symmetric, indicating differences in either the actual positions of the spheres (e.g., misalignment with element 8) or an unmodeled asymmetry in the drive winding.

This shows that the model captures the basic response of the sensors to spheres under the footprint of the array and with various positions of the sphere relative to the sense elements. Each of the sense elements provide information about the object properties; the capability for using this information is related to the sensitivity, which can be determined from the model, and the measurement noise, which is determined empirically. In follow-on efforts more systematic methods will be applied for using information from multiple sensing elements to estimate multiple properties of objects such as size, depth, shape and orientation.
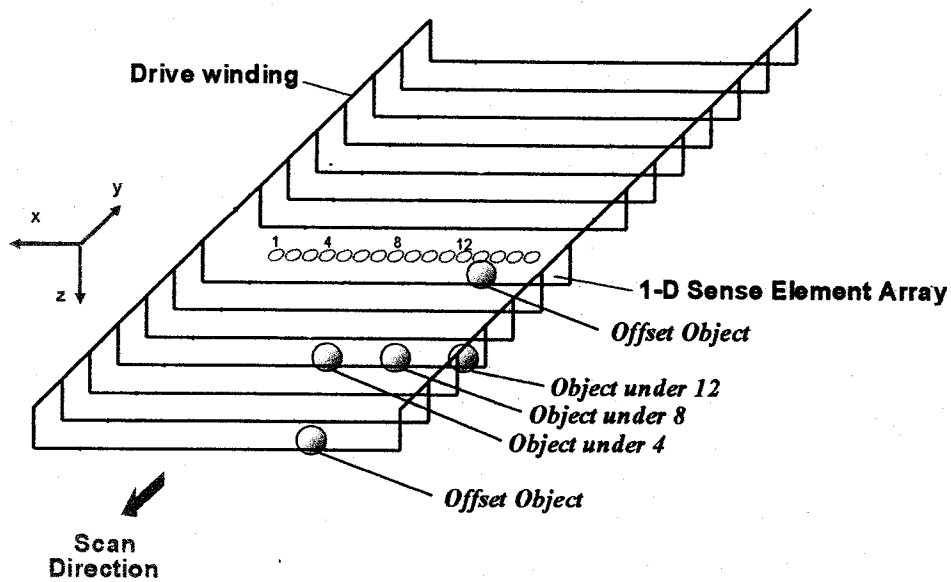
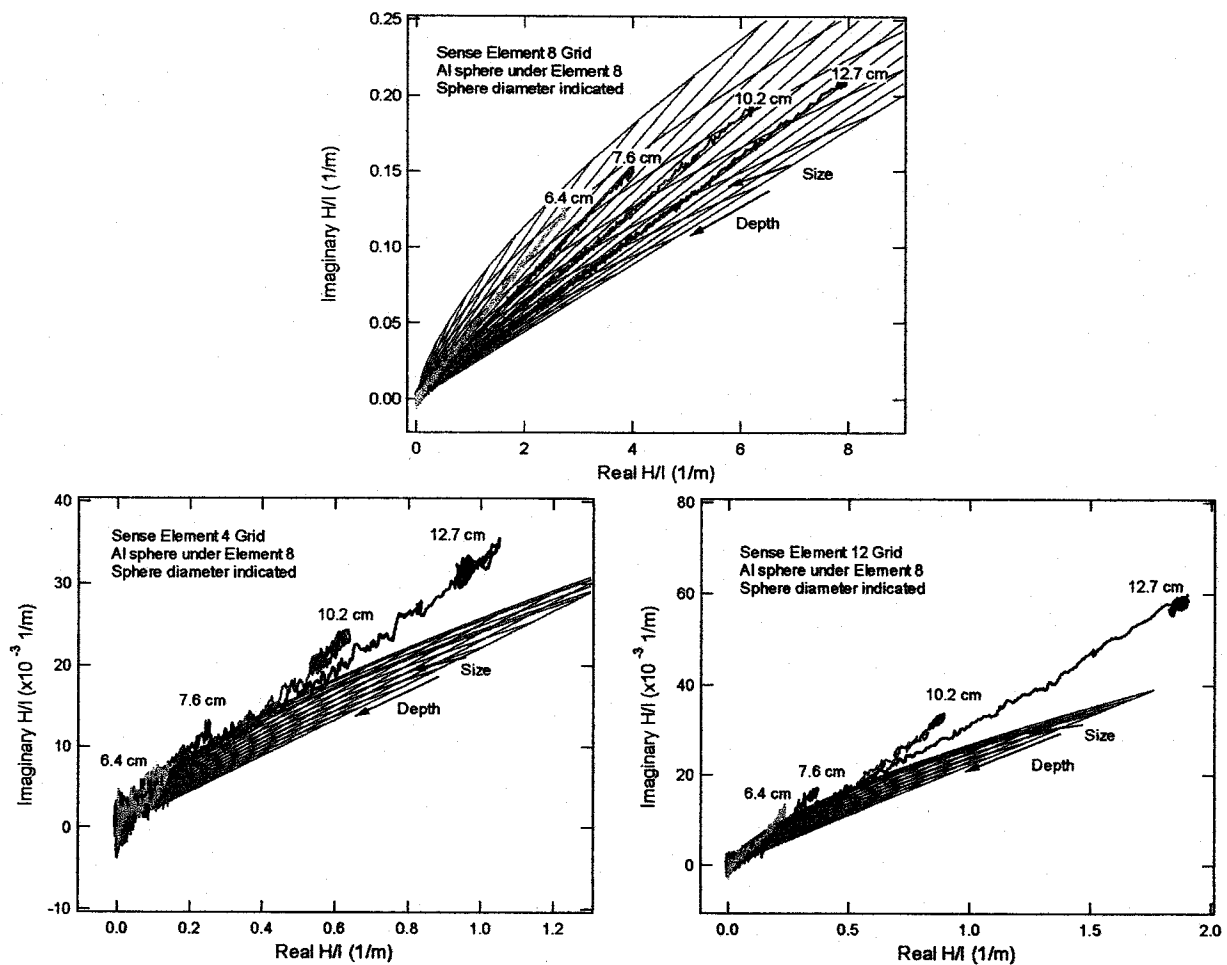Figure 14. Schematic for single object measurements with only depth varied.

Figure 15. Response of a single sense element (number 4, 8, or 12) as the depth of several aluminum spheres, placed beneath sense element 8, is varied.
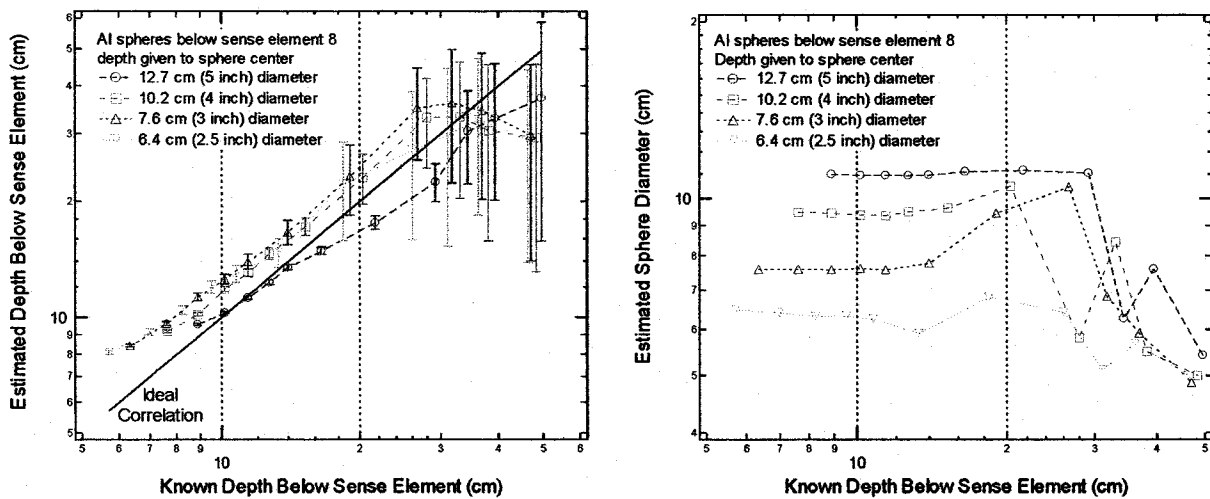
Figure 16. Estimated depth and size from element 8 for aluminum spheres placed beneath the element.
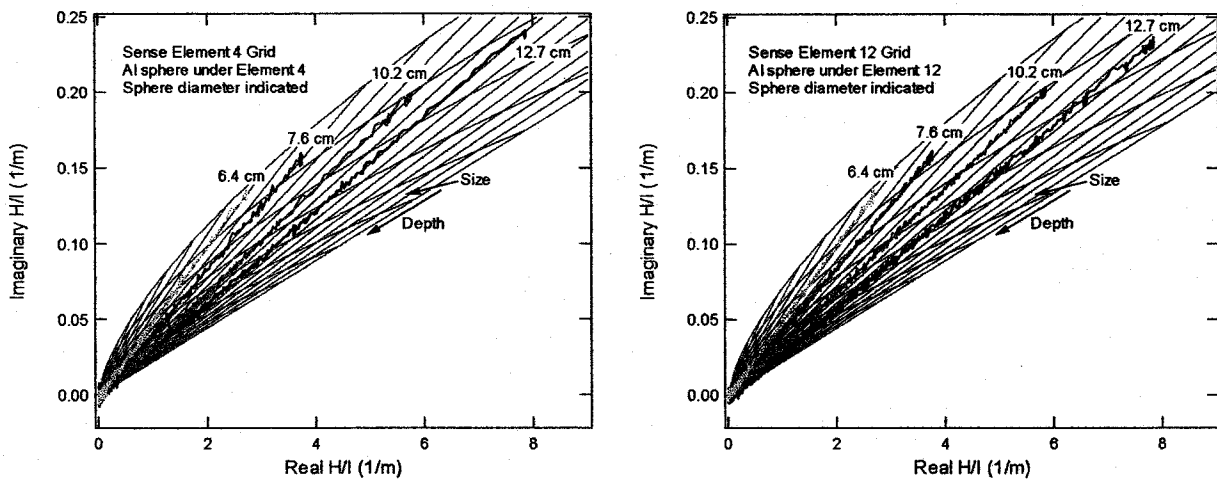

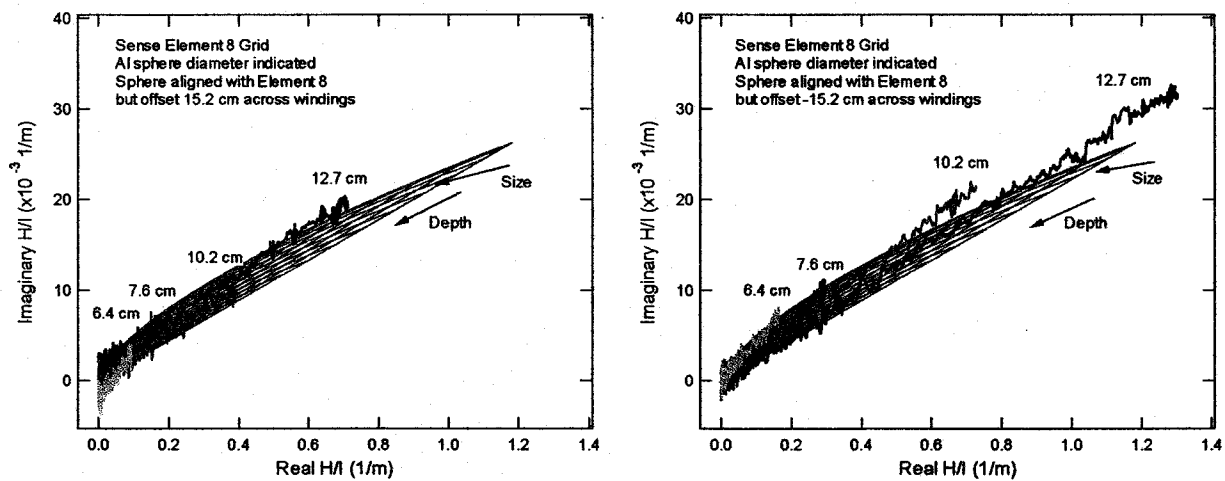Figure 17. Response of an element as the depth of several aluminum spheres beneath the element is varied.

Figure 18. Response of sense element 8 as the depth of several aluminum spheres is varied. The spheres are aligned with element 8 but offset by 6 in. across the drive windings.

Measurements of objects beneath a sense element as the object depth is varied also indicate that the real and imaginary parts of the signal can be used to discriminate between objects. Figure 19 shows the response as the depth of several UXO is varied from approximately 3.8 cm (1.5 in.) from the array to the top of the object, to greater than 30.5 cm (12 in.). Except for the spherical BLU-26 the response was measured for several orientations of the major axis (longest dimension) either parallel or perpendicular to the linear array of sense elements, or vertical with the UXO pointed down (tail up) or up (tail down). In each case, the response converges to the air point when the object is sufficiently far from the array to be detected. For the M385, all three orientations provide essentially the same response, with a large real component and a small imaginary component. For the BLU-26, the real and imaginary components are comparable. For the higher aspect ratio M86 and the MK2, the parallel and perpendicular orientations are similar but the vertical orientation provides a noticeable shift in the response. Note that the vertical M86 was pointed up in an attempt to better align the UXO with the sense element. The response shift is larger for the larger M86 UXO. Some of the reduction in signal associated with the vertical orientation is due to the center of the object being effectively deeper for the vertical orientation. The similarities in the responses for the M86 and MK2, at least in the parallel and perpendicular orientations, along the depth variation line indicates potential non-uniqueness issues for a single sense element and a simple sphere model response; the objects give a similar response at different depths, even though they are different sizes. Other information, for example from other sense elements (e.g., images), other sense element orientations, or multiple frequencies, would be needed to properly discriminate between these objects. **This further supports the value of a two-dimensional array of sensing elements.**

Additional tests were performed by scanning the array over known objects to demonstrate the imaging capability of the array. In the laboratory, this was performed using the test configuration of Figure 6, which has the sensor array mounted within a cart structure. A rotary position encoder provides the linear position of the array along the scan path. Objects were then placed at a fixed location and orientation beneath the array while a scan was performed.
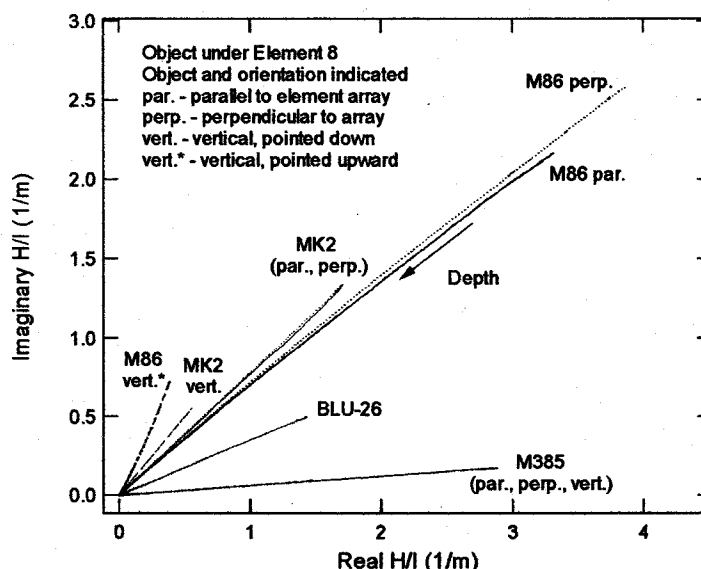
Figure 19. Response of sense element 8 as the depth of several objects is varied.

As a preliminary baseline measurement, a scan was taken without any objects beneath the array. The results are shown in Figure 20 and indicate modest variation of the sensor response between the elements. Ideally the response is zero in air and any variations in the response can be attributed to the instrument noise. Vertical stripes (common to all sense elements) corresponds to effects from the cart motion while the gradual variation in response along the length of the scan corresponds to drift in the response. The array was calibrated just prior to performing this scan. Figure 21 provides a comparison plot between the sense elements. Note that the units for the plots are different than the units for the images, which were obtained directly from the GridStation software, because the signal from the coils was unconventionally calibrated to be in terms of the field intensity instead of a voltage.
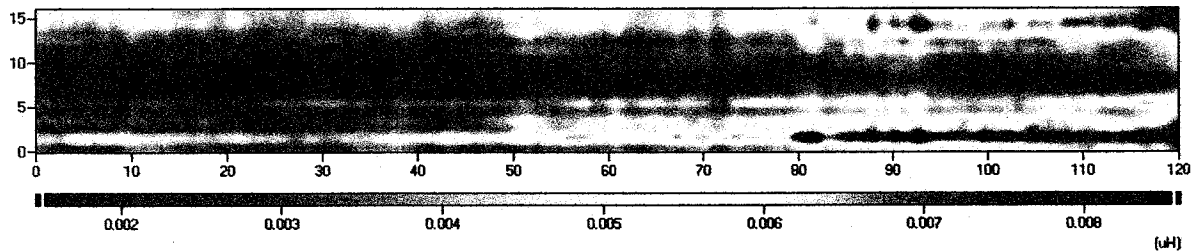
Figure 20. Array magnitude response in air, approximately 1.2 m (48 in.) above a cement floor. The horizontal axis gives the scan distance in inches. The vertical axis gives the distance across the sense element array in inches.
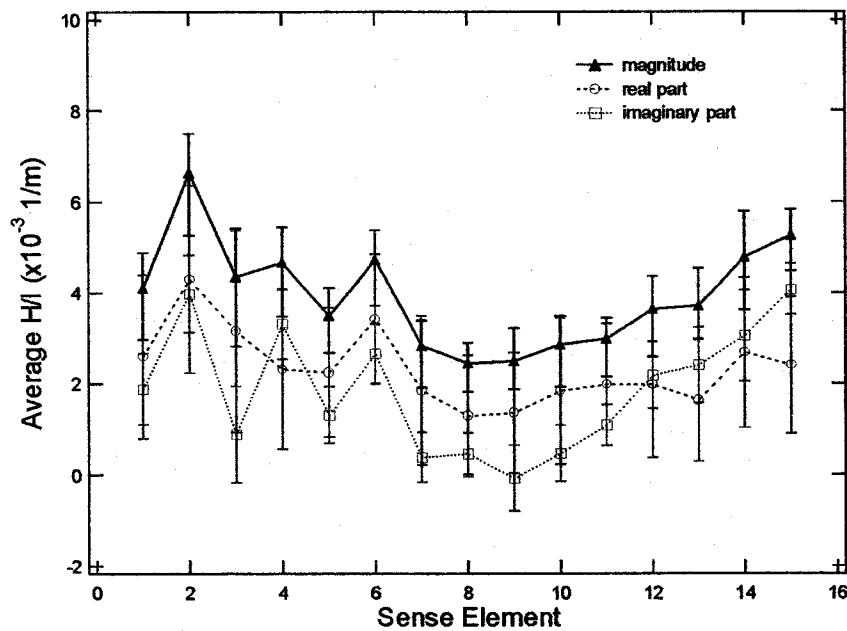
Figure 21. Plots of the average response of each element of the array for the scan in air of Figure 20. The error bars provide the standard deviation of the measurement.

Representative scan images over a 12.7 cm (5 in.) diameter aluminum sphere are shown in Figure 22 for a 5 cm (2 in.) depth. This depth is given to the top of the sphere. The figure shows images of the raw data in the form of the magnitude, real part, and imaginary part of the signal. In this case the real part of the signal is substantially larger than the imaginary part so that the magnitude tends to reflect the real part of the signal. The sphere is readily discerned from any background variations.
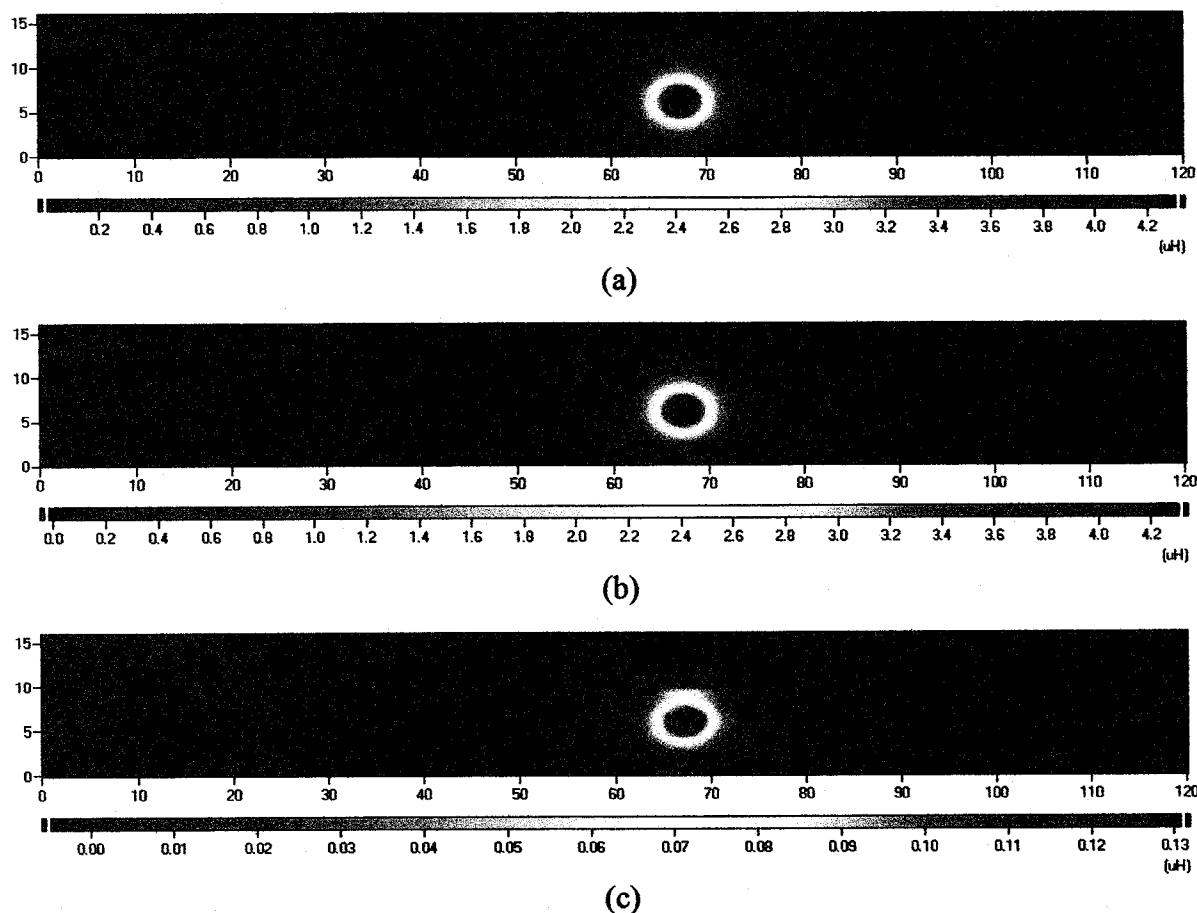
Figure 22. Array response over a 12.7 cm (5 in.) diameter aluminum sphere at a depth of 5 cm (2 in.). (a) Magnitude. (b) Real part. (c) Imaginary part. The horizontal axis gives the scan distance in inches. The vertical axis gives the distance across the sense element array in inches.

These measurements also demonstrate the diffusion or spreading of the field response as objects get farther away from the sensor array. The deeper sphere has a larger effective spatial image than the closer objects. This is illustrated clearly in Figure 23 for images taken for several depths of the 12.7 cm (5 in.) diameter sphere. The contrast is also evident in Figure 25, where the smaller but deeper sphere provides a larger spatial image than the larger but shallower sphere. Thus, the image by itself cannot be used to determine the object size and other information, such as the magnitude scaling, is necessary to correctly differentiate the object properties. If the depth is known, then the image size directly reflects the object size, as shown in Figure 26 for several different sized spheres at a fixed depth, which is taken as the distance to the top of the spheres.

The measurement grid can be used in conjunction with the image scans to determine effective properties for hidden objects. This is illustrated in Figure 24 for the 12.7 cm (5 in.) diameter aluminum sphere. The data points were taken from the peaks in the images in the real and imaginary components of the impedance. Note that Figure 23 only shows the magnitude response. This data compares favorably with the measurements taken as the aluminum sphere was lowered by hand beneath sense element 8. Differences in the measurements can be attributed to hand held measurements being slightly off the center line of the sense element.
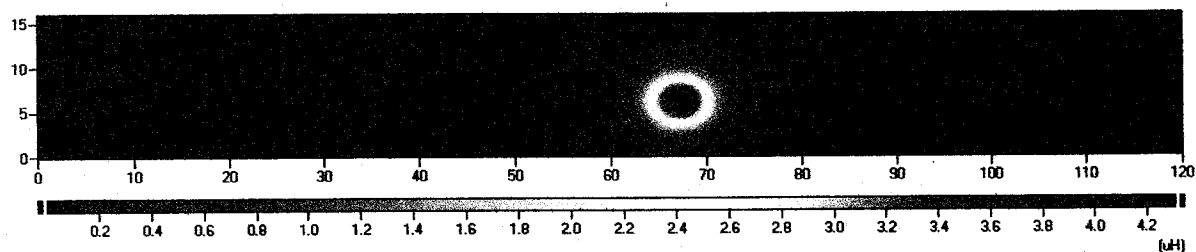
(a)
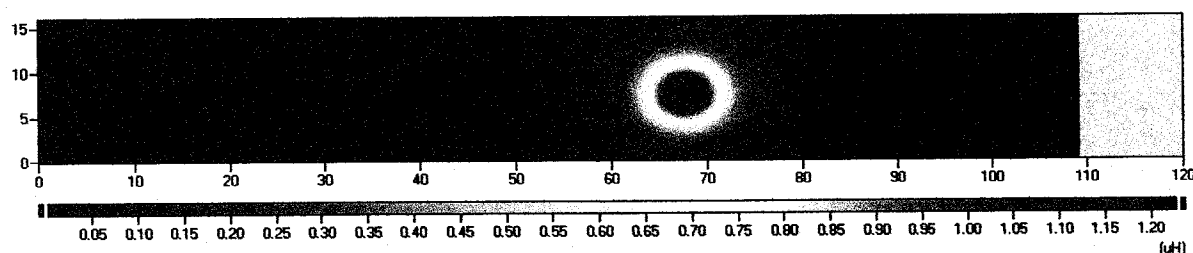
(b)
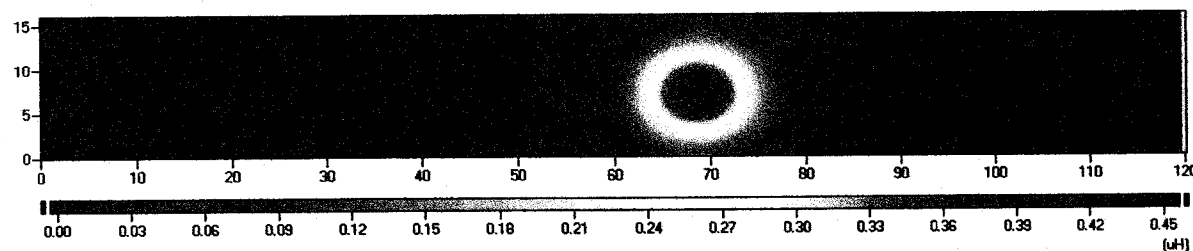
(c)
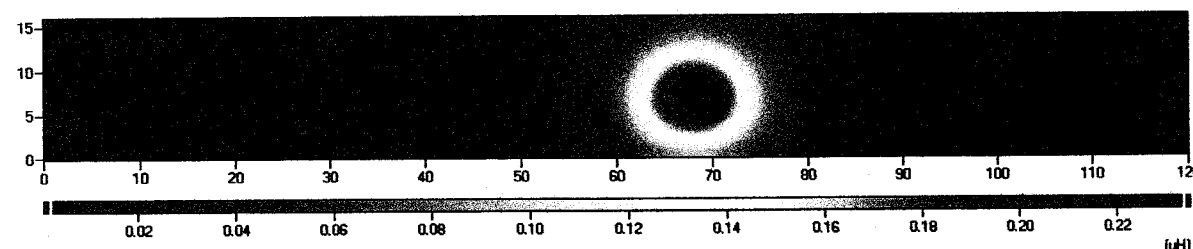
(d)

Figure 23. Array magnitude response over a 12.7 cm (5 in.) diameter aluminum sphere at a depth of (a) 5 cm (2 in.), (b) 10 cm (4 in.), (c) 15 cm (6 in.), and (d) 20 cm (8 in.).
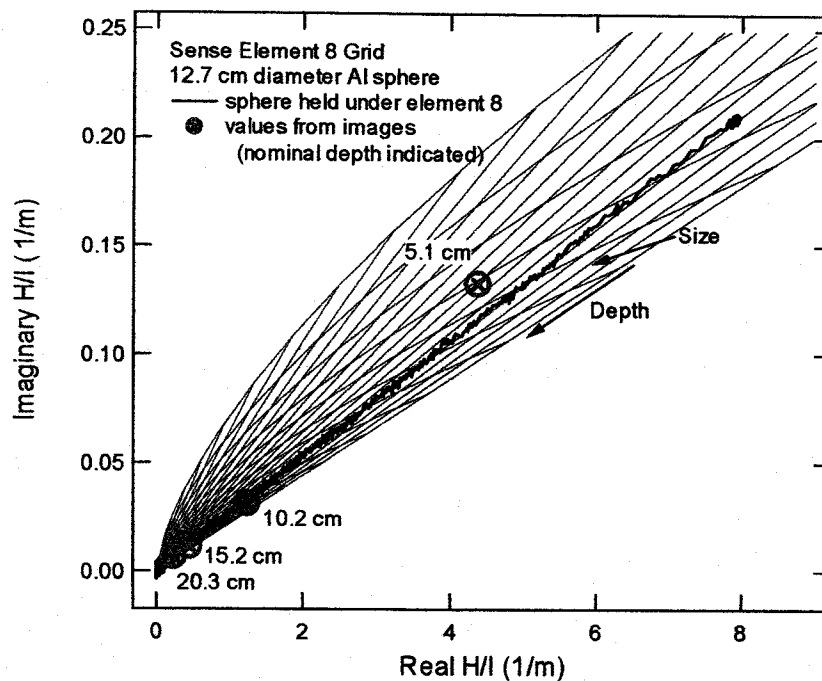
Figure 24. Response of the sensor array to the 12.7 cm (5 in) diameter aluminum sphere. The grid is for sense element 8. The stationary cart data, where the sphere was held beneath element 8 and lowered by hand is plotted along with impedance values taken from the peak signal responses in the image scans.
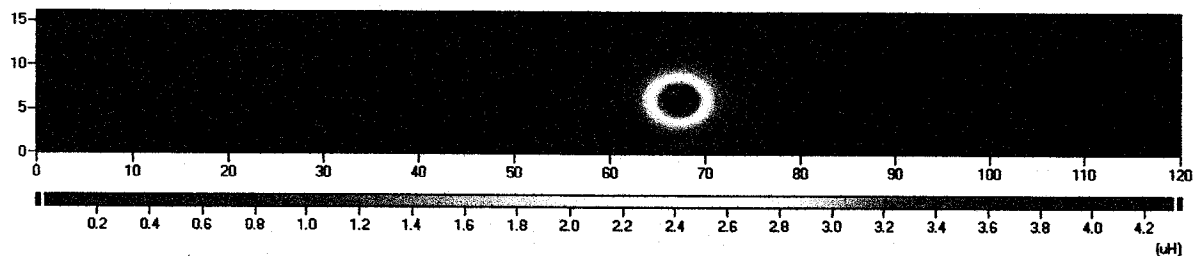
(a)
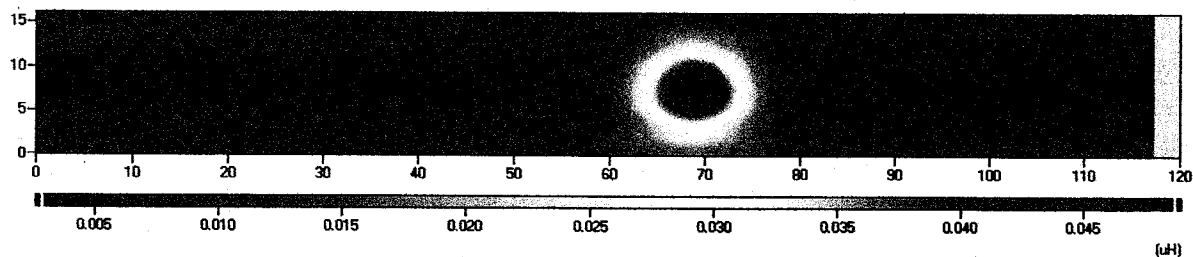
(b)

Figure 25. Array magnitude response over aluminum spheres of (a) 12.7 cm (5 in.) diameter and a depth of 5 cm (2 in.) and (b) 6.4 cm (2.5 in.) diameter and a depth of 20 cm (8 in.).
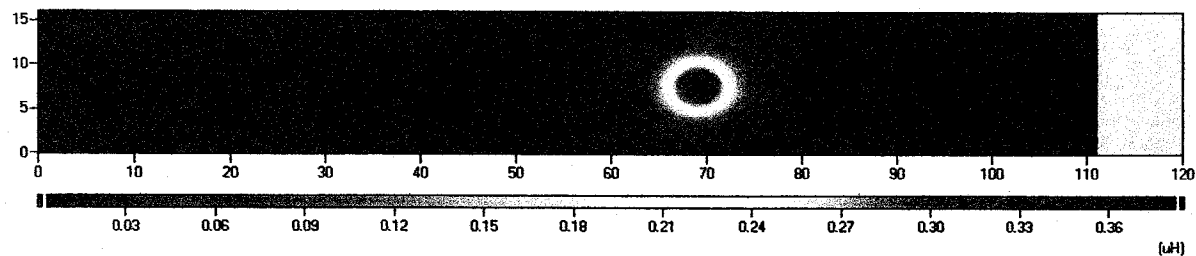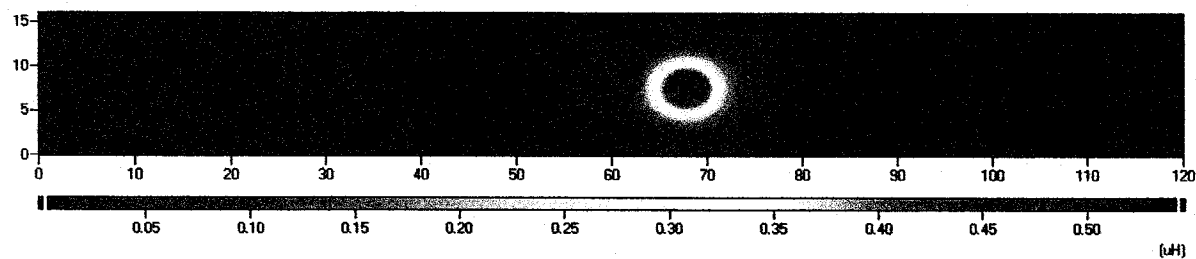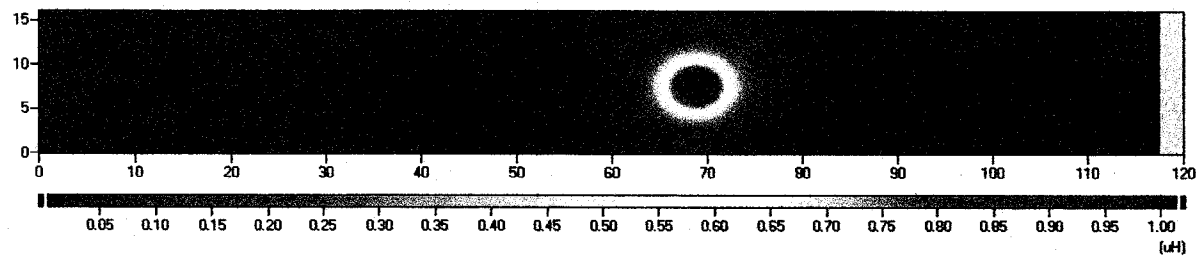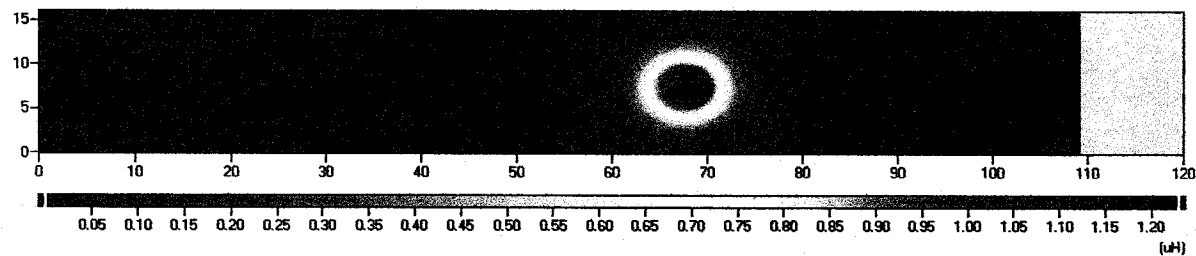
Figure 26. Array magnitude response over aluminum spheres at a depth of 10 cm (4 in.) for diameters of (a) 6.4 cm (2.5 in.), (b) 7.6 cm (3 in.), (c) 10.2 cm (4 in.), and (d) 12.7 cm (5 in.).

Scan images from the array can also reflect the orientation of hidden objects. To demonstrate this effect, two 0.9 m (36 in.) long pipes were placed at various orientations and scanned with the array. A representative set of measurement images is shown in Figure 27 for a 63.8 cm (1.5 in.) diameter pipe oriented parallel to the drive winding segments and perpendicular to the scan direction. The impedance data (magnitude, real part, and imaginary part) shows an approximately equal response for each of the array elements, except for the outermost elements. This indicates that each sense element sees essentially the same magnetic field; the outermost sense elements are most likely influenced by the return legs of the drive windings. **Extending the drive winding segments further past the sense element array and modifying the drive winding design to reduce the effect of these return segments should improve the quality of the images.**


(a)

(b)

(c)
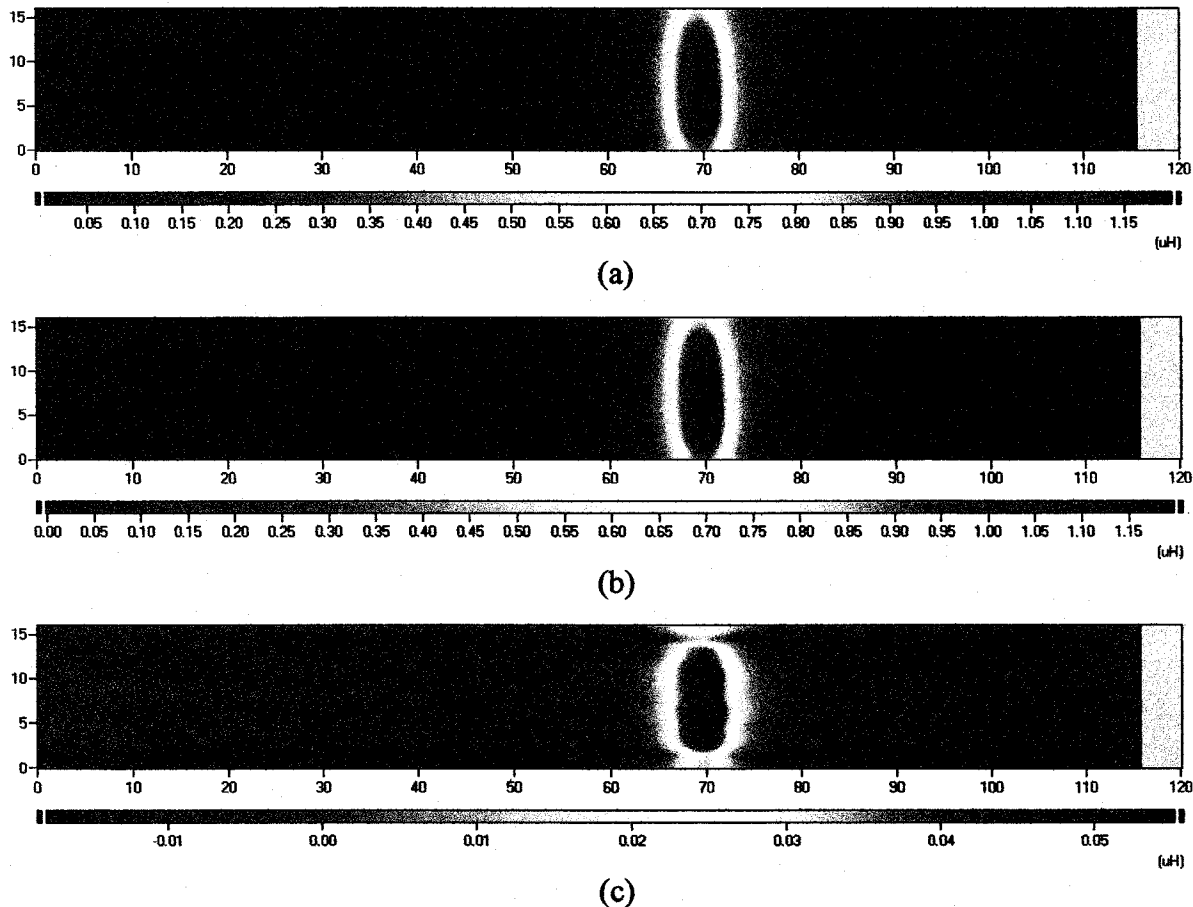
Figure 27. Array response over a 91 cm (36 in.) long 3.8 cm (1.5 in.) diameter pipe oriented parallel to the drive windings and at a depth of 10 cm (4 in.). (a) Magnitude. (b) Real part. (c) Imaginary part. The horizontal axis gives the scan distance in inches. The vertical axis gives the distance across the sense element array in inches.

Similar results are obtained with other orientations and other depths. For example, Figure 28 shows the magnitude response for three different orientations of the pipe: parallel, perpendicular, and at 45 degrees to the sense element array. The parallel and 45 degree orientation images show a reasonably uniform response except for the end effects at the edges of the array. Figure 29 shows the images for a deeper pipe. Note again that the spatial width of the images increases with object depth, corresponding to the greater diffusion of the magnetic fields from the deeper object. Figure 30 and Figure 31 show the corresponding data for the larger diameter pipe at two depths. The width of the detected object is larger, as expected, since the pipe is larger in this case while the depths were kept the same.
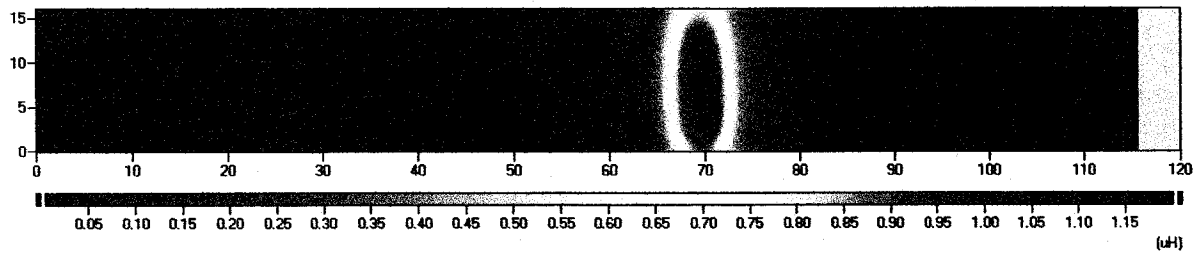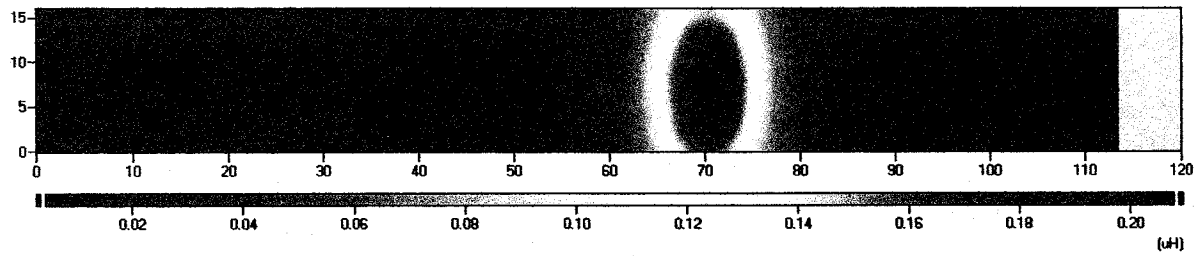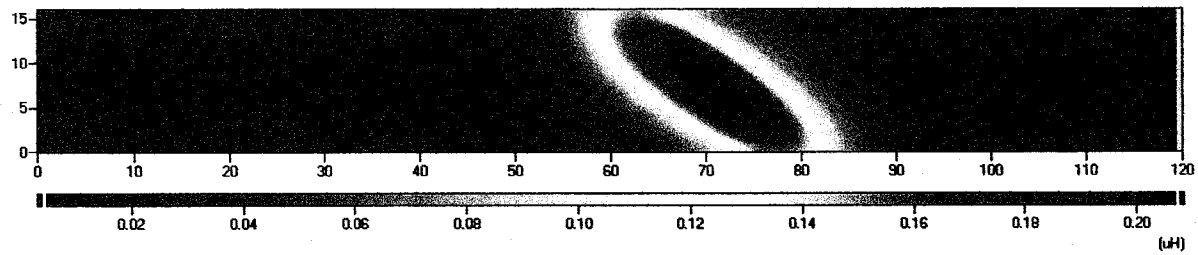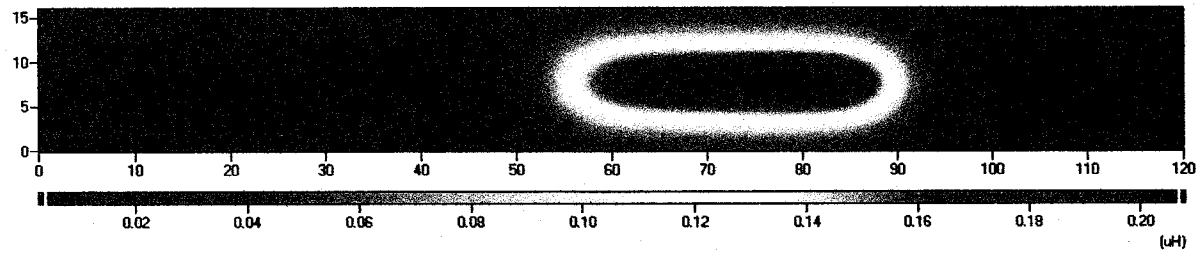

(a)
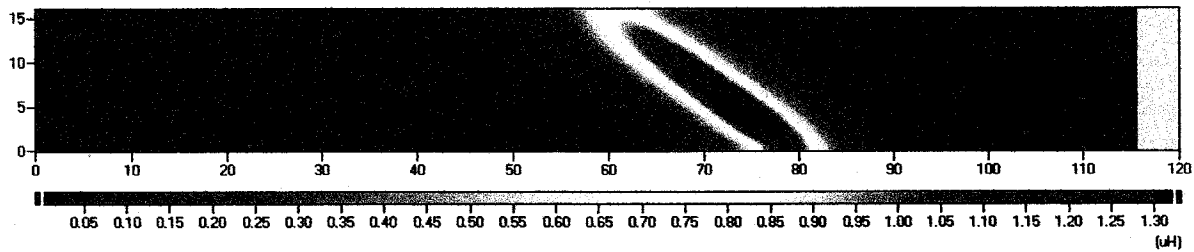
(b)
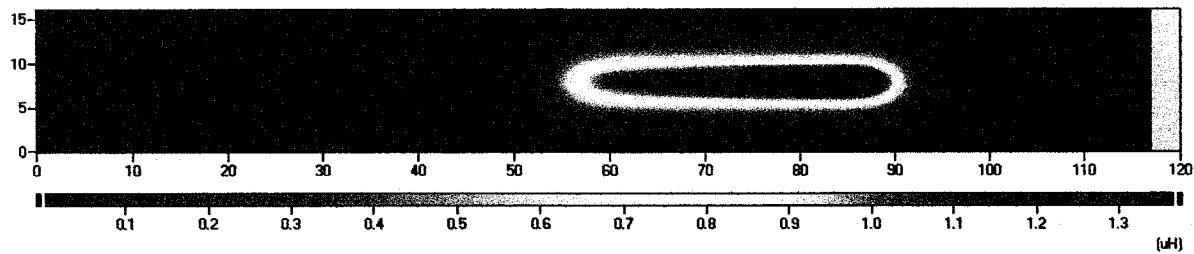
(c)

Figure 28. Array magnitude response over a 91 cm (36 in.) long 3.8 cm (1.5 in.) diameter pipe at a depth of 10 cm (4 in.) oriented (a) parallel to the sense element array, (b) at 45 degrees to the sense element array, and (c) perpendicular to the sense element array.
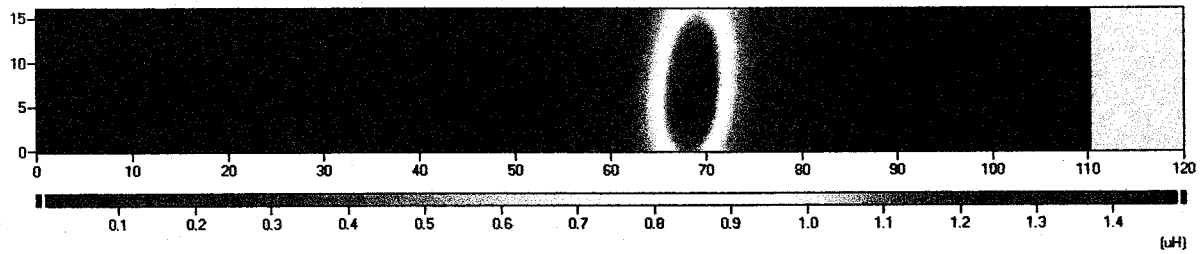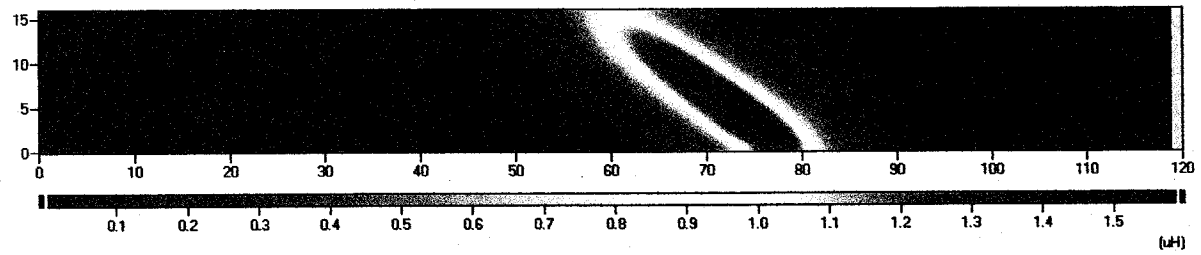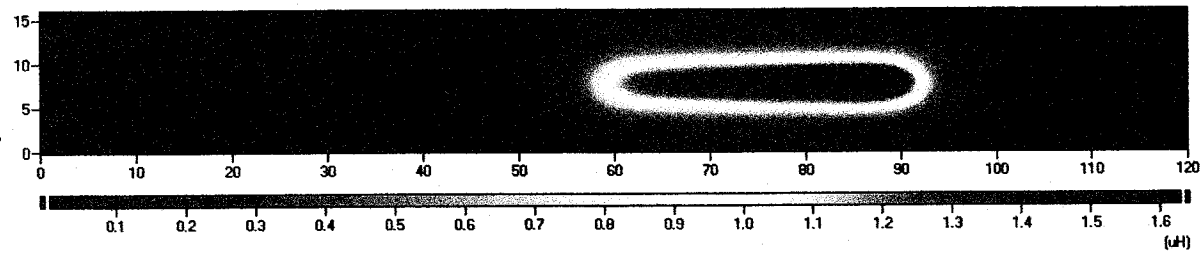
Figure 29. Array magnitude response over a 91 cm (36 in.) long 3.8 cm (1.5 in.) diameter pipe at a depth of 20 cm (8 in.) oriented (a) parallel to the sense element array, (b) at 45 degrees to the sense element array, and (c) perpendicular to the sense element array.

Figure 30. Array magnitude response over a 91 cm (36 in.) long 5.1 cm (2 in.) diameter pipe at a depth of 10 cm (4 in.) oriented (a) parallel to the sense element array, (b) at 45 degrees to the sense element array, and (c) perpendicular to the sense element array.
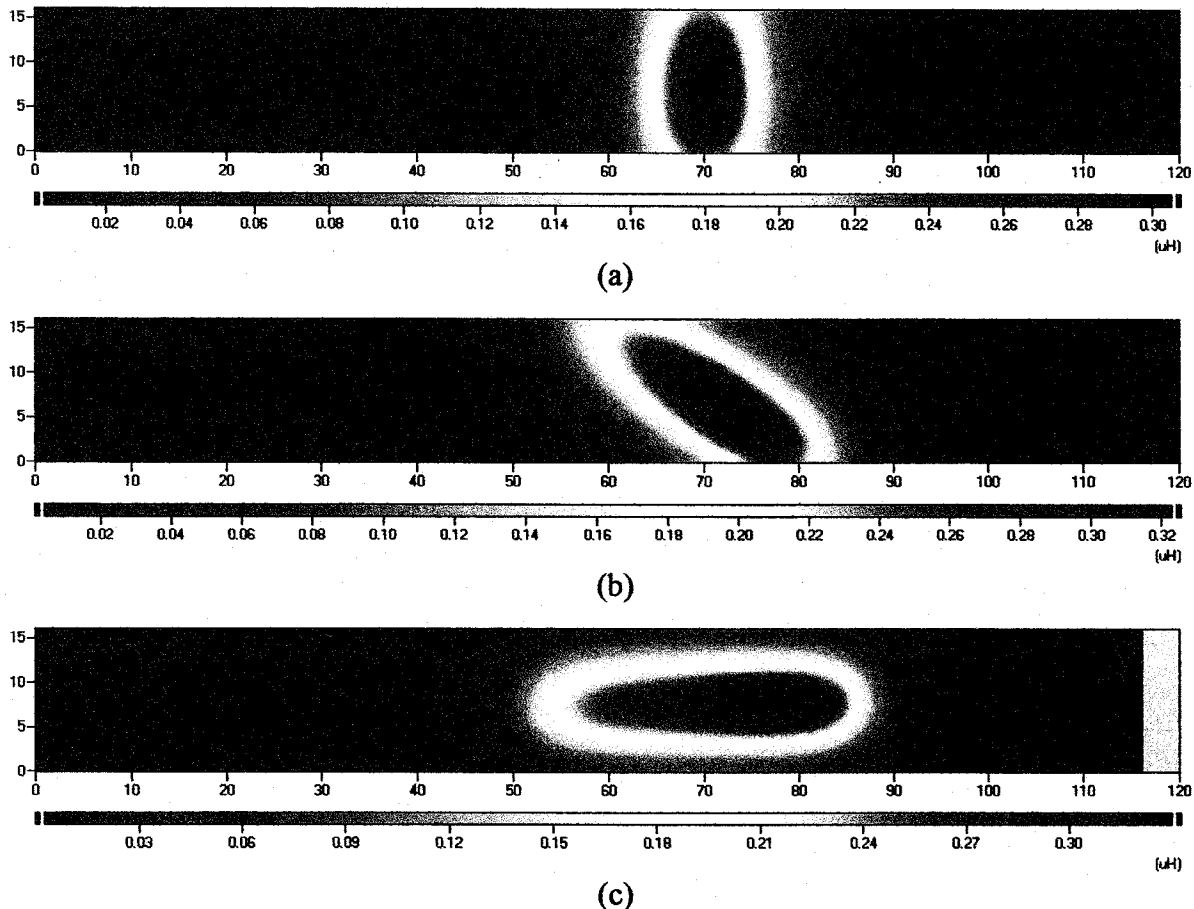
(a)

(b)

(c)

Figure 31. Array magnitude response over a 91 cm (36 in.) long 5.1 cm (2.0 in.) diameter pipe at a depth of 20 cm (8 in.) oriented (a) parallel to the sense element array, (b) at 45 degrees to the sense element array, and (c) perpendicular to the sense element array.

Figure 32 through Figure 35 show some scan images over several UXO having different orientations at a fixed depth. In this images, the depth is the distance from the sensor array to the top of the UXO. Figure 32 shows the basic response for a bomblet which does not change substantially with orientaions. The other UXO (MK2 for Figure 33, M86 for Figure 34, and MK118 Rockeye for Figure 35) have a longer axis that appears in the 45° angle images and is most evident when the UXO is perpendicular to the array of sense elements. The parallel orientation does not show an elongation of the image because the end effects at the edges of the array cause an effective narrowing of the object image. This narrowing effect is illustrated in the parallel orientation images over long pipes of Figure 27 through Figure 31. Extending the lengths of the drive winding segments and using other drive winding configurations that reduce the inhomogeneity across the sense element array should provide images that show the object orientation in the parallel direction. Alternative, compensation techniques can be applied to the images themselves, as illustrated in Figure 36, to correct for unmodeled inhomgeneneities. Another difference is the spatial resolution of the image. In the scan direction, the increment between data points is typically less than 1 mm (0.039 in.). In contrast, in the array direction, the distance between elements is 25.4 mm (1.0 in.) and the image resolution is lower. **Thus, use of**

an even higher resolution array (e.g., 32 instead of 16 elements) would further improve capability to determine object shape.
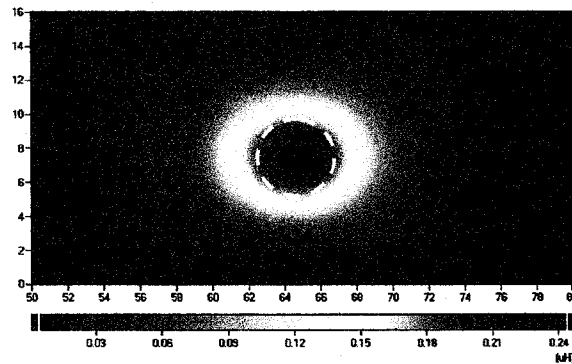

Figure 32. Array magnitude response over an BLU-26 with the distance from the array to the top of the UXO 10.2 cm (4 in.). The axes give the scan dimensions in inches. The dashes indicate a circular response.

Figure 33. Array magnitude response over an MK2 for several orientations with respect to the sense element array with the distance from the array to the top of the UXO 10.2 cm (4 in.). The axes give the scan dimensions in inches. The dashes indicate a circular response

Figure 34. Array magnitude response over an M86 for several orientations with respect to the sense element array with the distance from the array to the top of the UXO 10.2 cm (4 in.). The axes give the scan dimensions in inches. The dashes indicate a circular response.
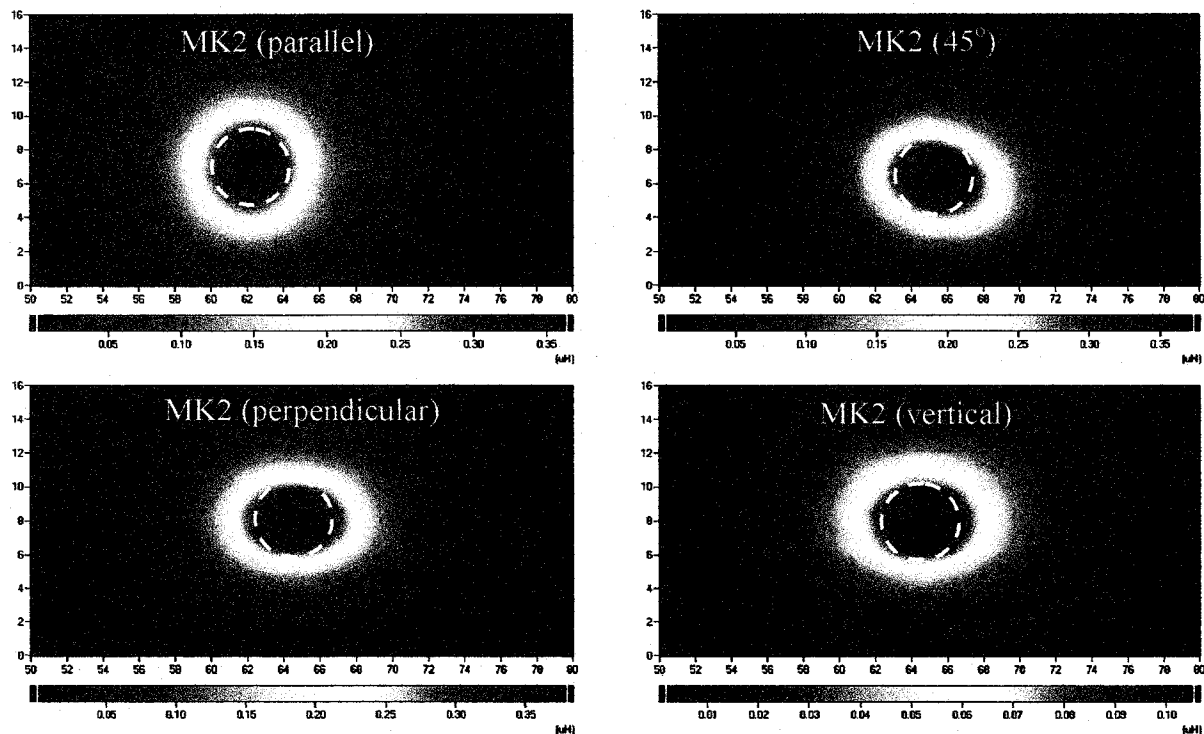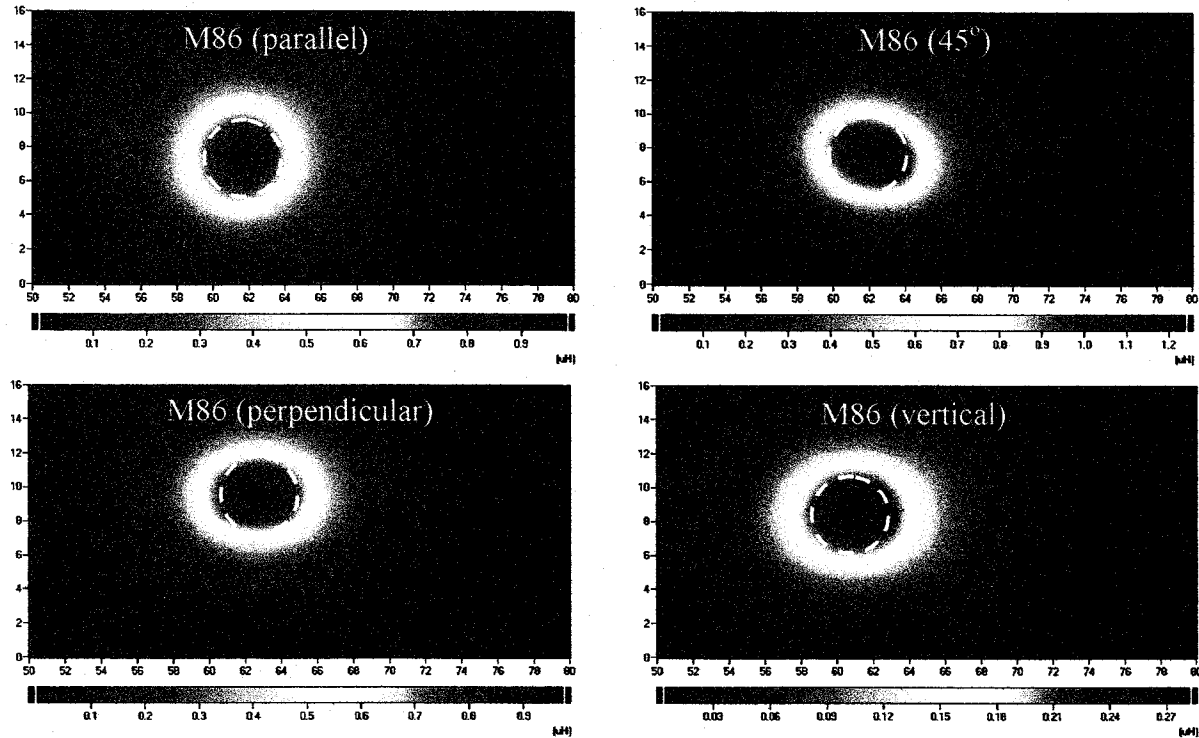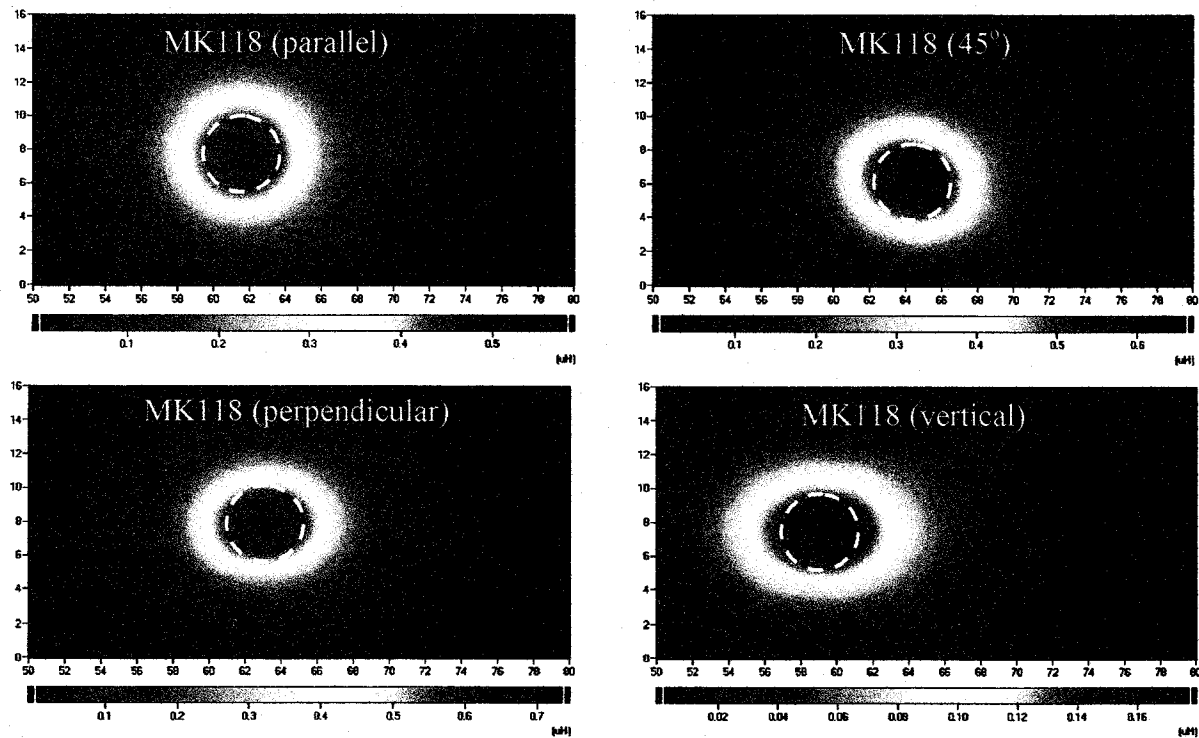

Figure 35. Array magnitude response over an MK118 Rockeye for several orientations with respect to the sense element array with the distance from the array to the top of the UXO 10.2 cm (4 in.). The axes give the scan dimensions in inches. The dashes indicate a circular response.
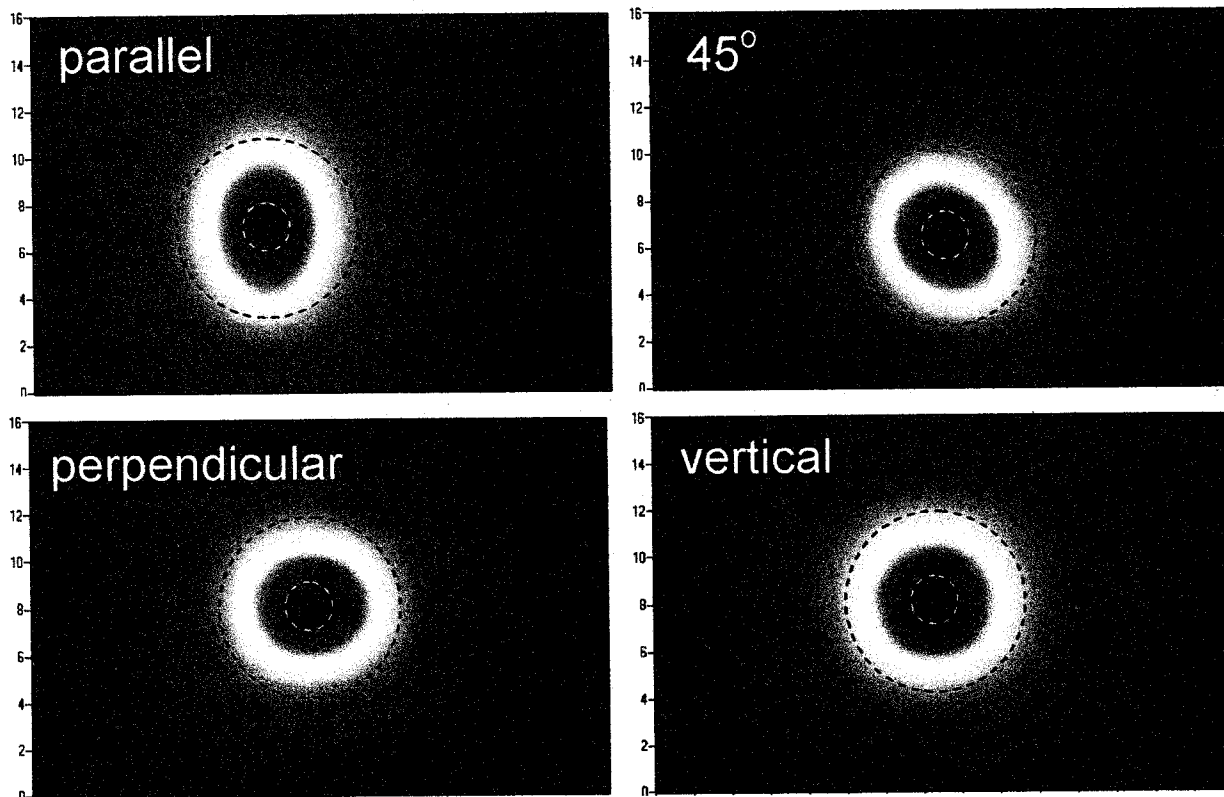
Figure 36. Compensated array magnitude response over an MK2 for several orientations which correspond to Figure 33.

The magnitude images of Figure 32 through Figure 35 have embedded within them the impedance images and data that can provide information about the object characteristics. The peak values of the real and imaginary portion of the response were taken from the scan images and plotted in Figure 37. The lines indicate the response of the sense element if the sense element was centered and raised over the object from Figure 19. The different UXO have different base impedance values, consistent with the measurements taken as the UXO are dropped below a specific sense element, as in Figure 19. The only significant difference in responses occurs for the vertical M86, which was pointing upward in Figure 19 and downward in Figure 37. Note that scan images also tend to have slightly smaller values for the peak response because the image is providing a spatial average of values in two directions (x and y) while the single element measurement do not have any spatial averaging of the measurement signal. This confirms that the scan images can provide some impedance information for providing object discrimination.

These values for the measured response were then processed using sphere model grids to determine the effective size and depth of the object. The same grid was used for each orientation of an object. Different grids, based on nominal electrical properties, were used for each object, except for the MK2 and the M86 which used the same grid. These results, given in Table 1, are in reasonable agreement with the nominal object sizes. Note that the UXO are generally not spherical so that the sphere model is not truly appropriate; however, it does provide a reasonable estimate of the object properties. Furthermore, this is a simple use of a model for estimating

properties. Only a single value from the scan image is used to estimate the object properties. **Better estimates are expected when the nonspherical shape is accounted for and the responses from multiple sense elements are used. Thus, the use of ellipsoid models, multiple sensing elements to discriminate object features (shape, size, orientation) should be investigated in the follow-on effort.**
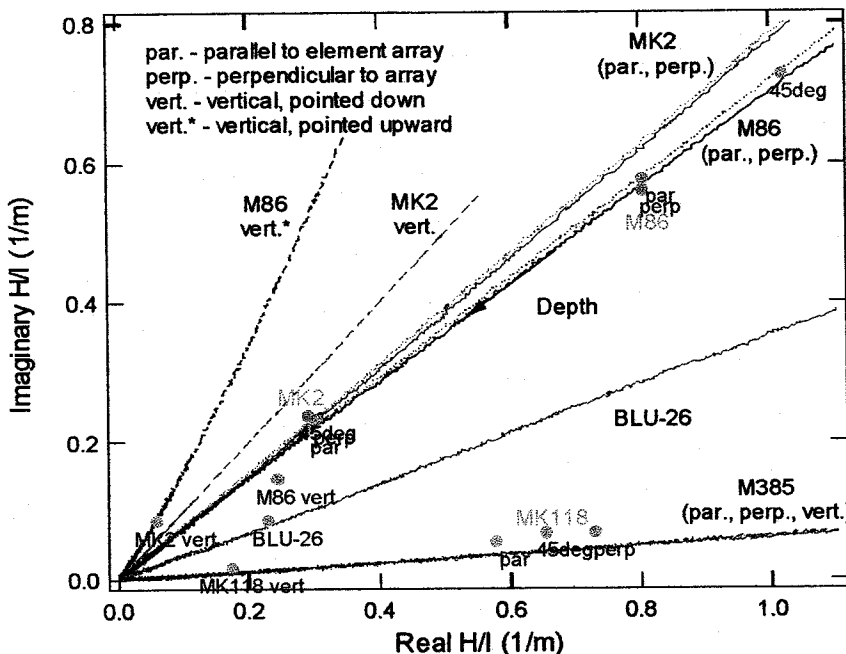

Figure 37. Impedance response for several UXO taken from scan images with the distance from the array to the top of the UXO 10.2 cm (4 in.).

Table 1. Estimated properties for the UXO measurements of Figure 37.

UXO	Orientation	Nominal Properties			Image Response		Estimated Properties	
		Diameter (cm)	Length (cm)	Depth (cm)	Real (1/m)	Imag. (1/m)	Diameter (cm)	Depth (cm)
BLU-26		6.4		13.2	0.2304	0.0853	5.50	13.38
MK2	parallel	4.0	15.9	12.0	0.2916	0.2192	6.69	13.54
MK2	perpendicular	4.0	15.9	12.0	0.3028	0.2333	6.59	13.14
MK2	45 deg	4.0	15.9	12.0	0.2931	0.2374	6.39	12.82
MK2	vertical	4.0	15.9	17.9	0.0609	0.0864	4.82	14.09
M86	parallel	5.7	16.0	12.9	0.8059	0.5769	6.90	10.41
M86	perpendicular	5.7	16.0	12.9	0.8058	0.5604	7.03	10.62
M86	45 deg	5.7	16.0	12.9	1.0200	0.7264	6.92	9.71
M86	vertical	5.7	16.0	18.0	0.2448	0.1465	7.78	16.60
MK118	parallel	4.5	21.6	12.3	0.5776	0.0548	4.44	9.11
MK118	perpendicular	4.5	21.6	12.3	0.7304	0.0690	4.46	8.51
MK118	45 deg	4.5	21.6	12.3	0.6547	0.0675	4.10	8.07
MK118	vertical	4.5	21.6	20.8	0.1760	0.0178	4.18	12.42

Measurements have also been performed over multiple objects in order to show the benefit of high resolution imaging. Figure 38 shows several response images for the bomblets aligned parallel to the sense element array. Figure 39 shows several response images for the bomblets aligned perpendicular to the sense element array. At shallow depths and with large separation distances, the response of each bomblet is distinct. For deeper depths and smaller separation distances, the interactions between the objects become more apparent and the diffusion of the magnetic field response leads to an overlap of the effective response and an apparent "single" object response. This response has an effective orientation associated with alignment of the objects and also local maxima that are associated with the center of the objects. For very deep objects and for very small separations, the effective orientation of the response becomes less apparent and symmetric responses result. The use of a high resolution imaging array allows the spatial variations of the response from the objects to be captured, including orientation and local maxima and minima in the response that may permit separation of object responses. **Combining information from high resolution images with property estimates from measurement grids at multiple sensing elements should be addressed in the follow-on effort.**
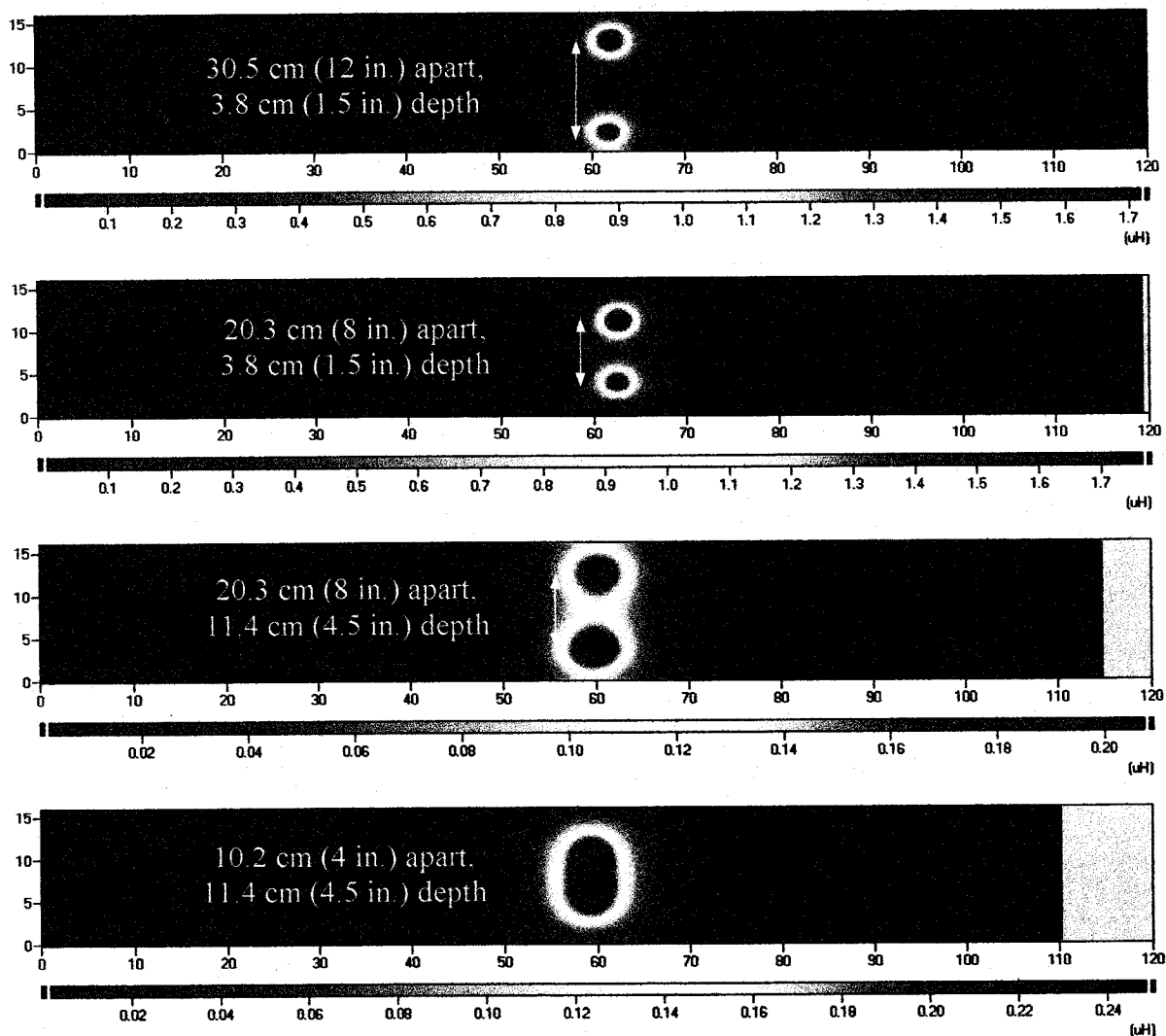

Figure 38. Array response over two BLU-26 bomblets aligned parallel to the sense element array. The axes give the image dimensions in inches.
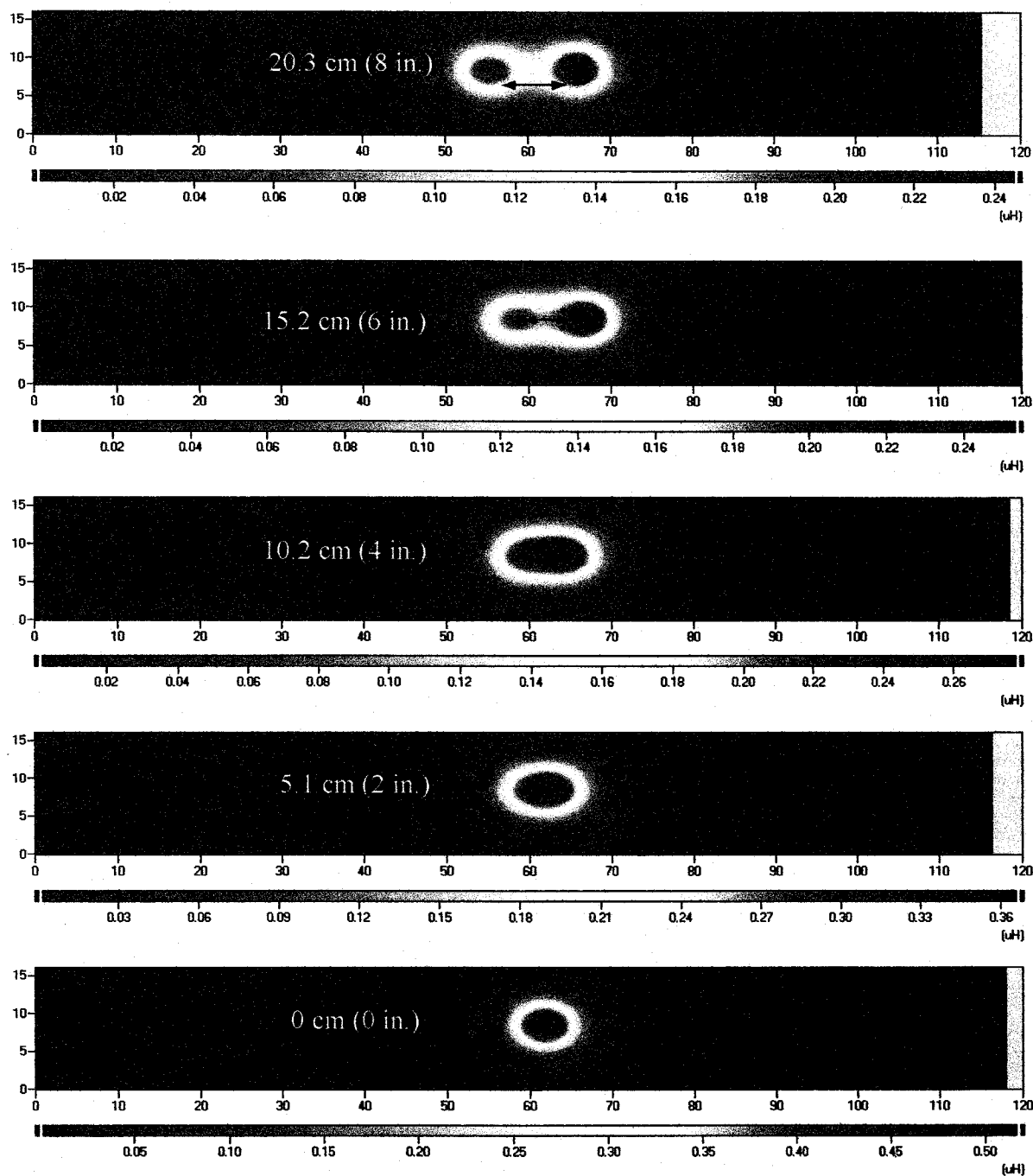
Figure 39. Array response over two BLU-26 bomblets 10.2 cm (4 in.) below the array. The inside spacing between the bomblets is indicated. The axes give the image dimensions in inches.

Field Tests

Preliminary tests were performed on the calibration grid of the Aberdeen Proving Grounds Standardized Test Site in December, 2002. The goal of these measurements was to obtain initial field experience at a test site, which would provide input for enhancement criteria and recommendations. The focus of these tests was on the objects located nearer the surface, with a depth less than 0.4 m, which was generally the smaller objects.

A schematic diagram of the objects and their locations on the test grid is shown in Figure 41. The test grid is divided into 1 m sections with letters denoting the grid column and numbers denoting the grid lane. An object is placed near the center of various grid cells with depths and orientations varying. Eight pound shot put markers are placed around the edge of the calibration grid and at several locations within the grid. The distance between objects is generally 2 m or greater.
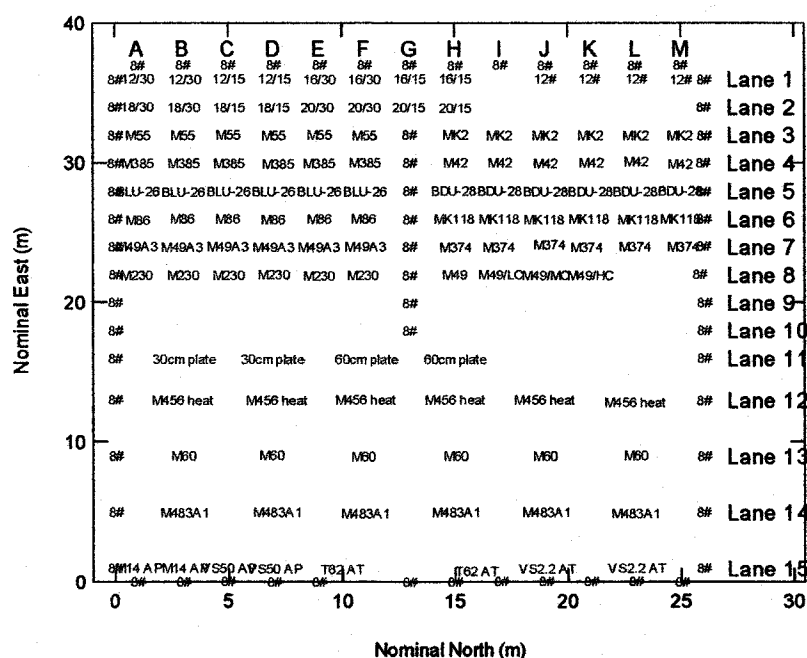

Figure 40. Schematic diagram of the calibration grid.

Measurements were performed at various locations in the grid using the instrument configuration shown in Figure 43. This was essentially the same as the configuration used in the laboratory. Power was supplied by a portable generator located at a distance from the equipment, near the vehicles. The original intent for the measurements was to position the table with the support instrumentation (impedance instrument and laptop) near several grid cells. Then, measurements would be performed by scanning the cart over these cells without moving the table. However, it was decided in the field that it would be more convenient for covering larger areas to simply move the table along with the cart so that longer measurement scans could be obtained. As a result, for measurement scans covering distances less than approximately 2 m the table was not moved, but for longer scans, the table was moved along side of the cart. Scan distances were monitored with a rotary position encoder on the rear wheel axel of the cart. The encoder was calibrated with a tape measured and periodically checked during the trial.
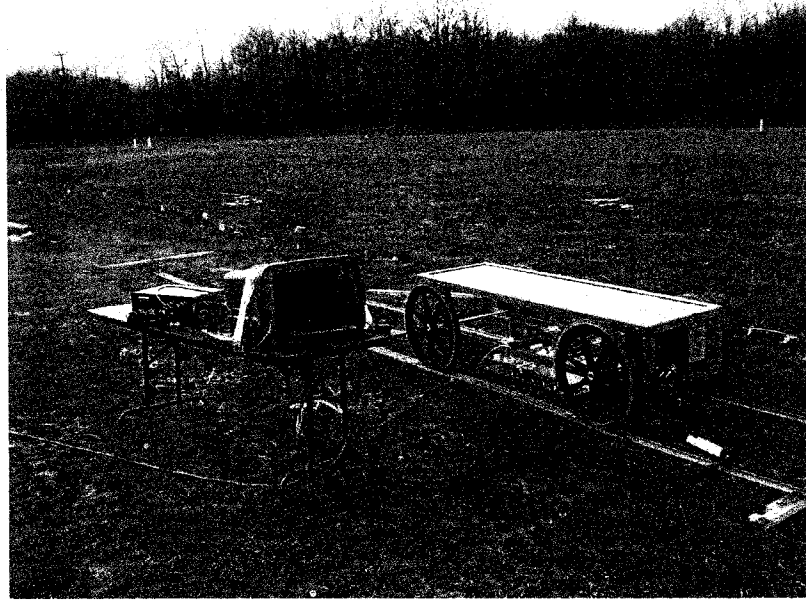
Figure 41. Photograph of the cart with sensor array and support instrumentation used during the field test.

The site was relatively wet during these tests. The week prior to these field tests, they had received several inches of snow, which was followed by several days of rain. The ground had a day or two to dry out slightly before our arrival. During the testing the mornings were cold enough that the ground was basically frozen, but in the afternoons it had warmed enough so that some areas had free standing water and the ground was a relatively soft mud. Fortunately, most of the shallower objects of interest were located in lanes 1 through 8 which were on relatively dryer and flat ground. Figure 41 shows that the ground was relatively flat in some areas. Some of the other objects, particularly those in the lower left corner of the grid were under water or in relatively rough terrain, as shown in Figure 42. When possible, attempts were made to scan over the objects in these areas.
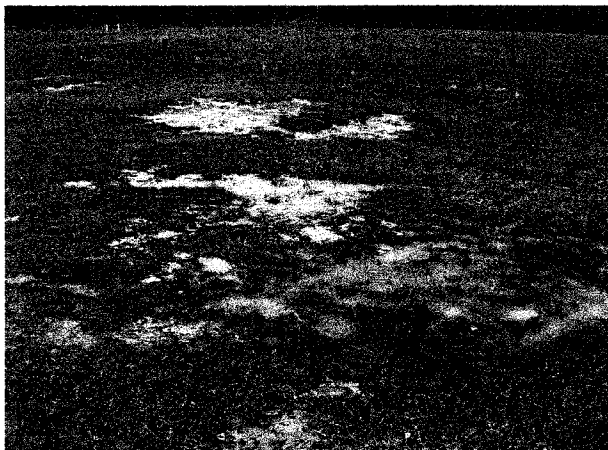

Figure 42. Photographs of some of the areas of rough terrain, some of which were also under water.

Measurements were generally performed in a scanning mode, where the cart was pushed along the test lane. Figure 43 provides a schematic for the scan of the cart along the center of a path.

The sense elements only span a portion of the cell so complete coverage of the cell was obtained with multiple scan passes. Typical offsets of the array were approximately 0.36 m (14 in.) on either side of the center scan path width from the center so that there were several elements of overlap with the "center" scan path. The positions of the grid cell markers were confirmed visually with the row and column flags and the other cell markers. They were also confirmed with a tape measure to be in approximately the correct location.
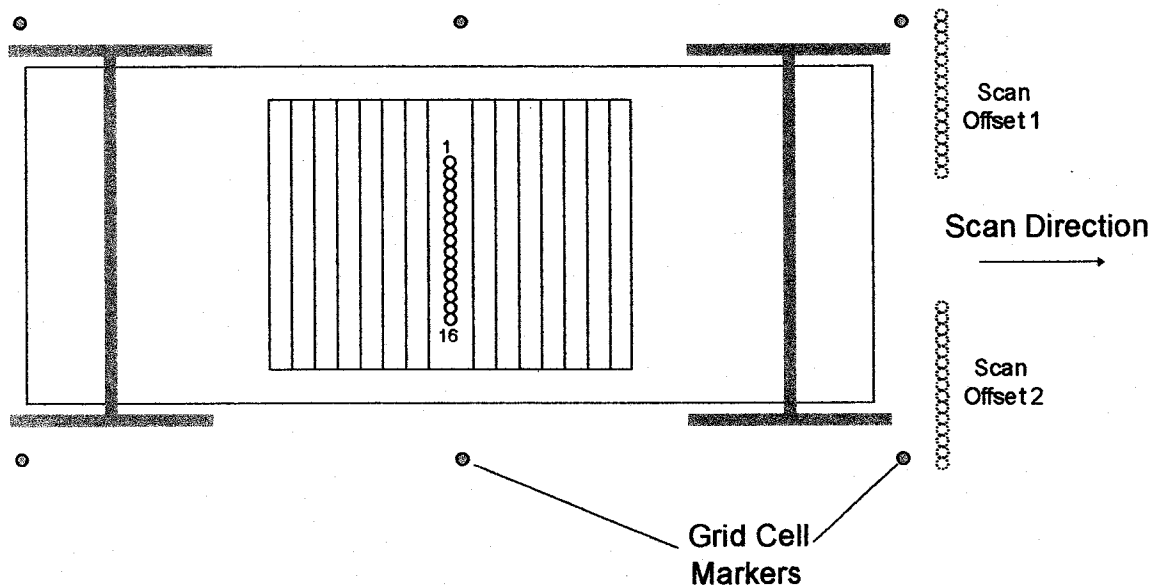

Figure 43. Schematic diagram for the cart and sensor array orientation for a scan along the center of a grid cell.

For these scans over the ground surface, the typical standoff distance or lift-off between the sensor array and the ground surface was about 5 cm (2 in.) but was increased or decreased as indicated for individual scans. The nominal distance changed as the array was scanned over the surface since the ground was rough, with some deep ruts that led in some case to ~ 10 cm (4 in.) air gaps and also caused some tilt in the cart holding the array. There was also some settling in the areas where objects were buried.

A representative "vertical" scan down a column is shown in Figure 44. **As expected from the laboratory measurements, the different objects had distinguishable signature responses.** The M55 appears in the imaginary part image, but not in the real part image. In contrast, the M385 appears predominantly in the real part image, with a relatively weak response in the imaginary part image. The BLU-26 provides a strong response in both the real and imaginary part images, while the deep M86 is not apparent. When only the magnitude of the response is plotted, which in this case is dominated by the real part of the response, the indication for the M55 is not obvious. However, a logarithmic color scale accentuates the low signals and compresses the high signals, which allows the M55 to be revealed in the magnitude image, as shown in Figure 45. A drawback is that more of the noise is also visible in the image. For convenience in plotting the large number of scans over the test grids, much of the scan data will be presented as magnitude images using the logarithmic color scale. The repeatability of the scans is demonstrated in Figure 46.
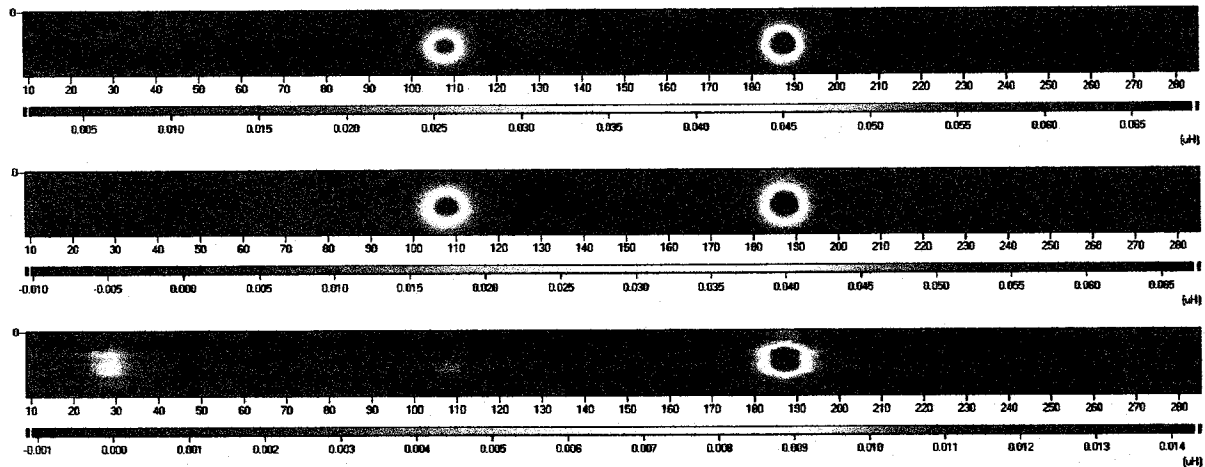
Figure 44. Vertical scan down the center of cells A3-A6. The horizontal axis gives the scan distance in inches. The vertical axis gives the distance along the sense element array and spans 0.41 m (16 in.). The object type, depth, azimuth angle, dip angle and approximate position are: M55 (0.1 m, 0°, 45°) at ~28 in., M385 (0.1 m, 0°, 45°) at ~106 in., BLU-26 (0.1 m, 0°, 0°) at ~184 in., and M86 (0.4 m, 0°, 45°) at ~262 in. The top image gives the magnitude, the middle gives the real part, and the bottom gives the imaginary part.
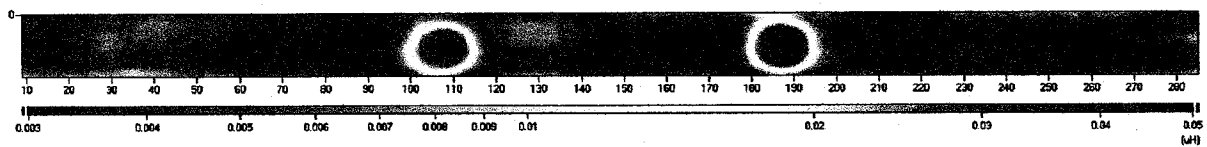

Figure 45. A plot of the magnitude response from Figure 44 using a logarithmic color scale.
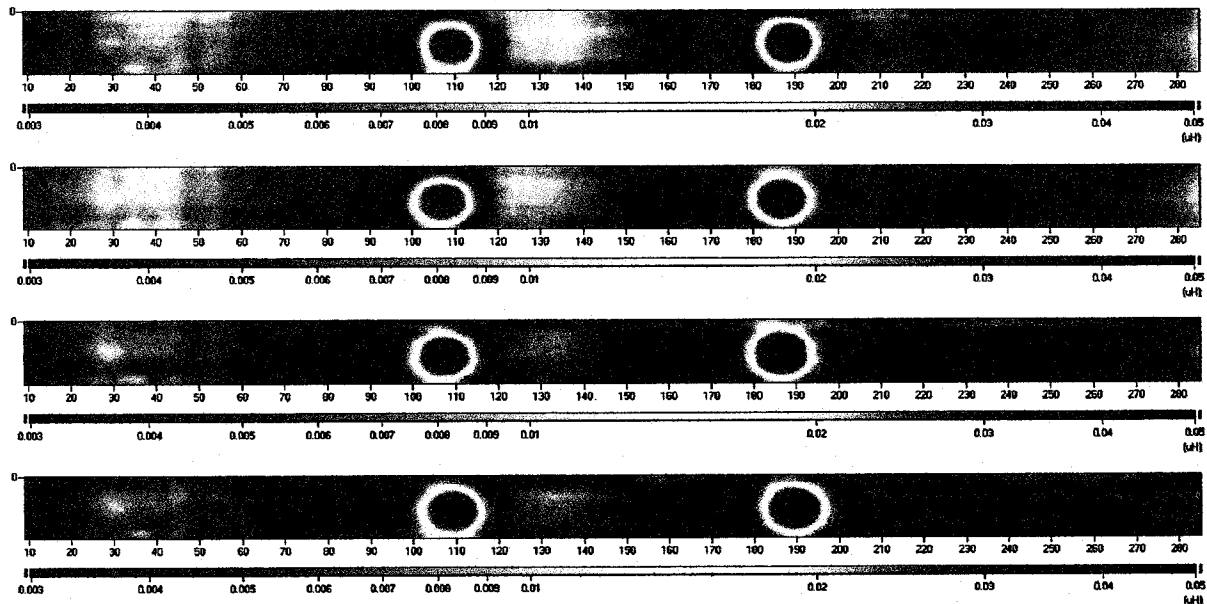
Figure 46. Repeatability of magnitude images for vertical scans down the center of cells A3-A6. The horizontal axis gives the scan distance in inches. The vertical axis gives the distance along the sense element array and spans 0.41 m (16 in.). The object type, depth, azimuth angle, dip angle and approximate position are: M55 (0.1 m, 0°, 45°) at ~28 in., M385 (0.1 m, 0°, 45°) at ~106 in., BLU-26 (0.1 m, 0°, 0°) at ~184 in., and M86 (0.4 m, 0°, 45°) at ~262 in. A calibration was only performed prior to the first scan.

Similar measurement scans were performed with the array offset from the center of the objects, as shown in Figure 47. In this case the array was moved in approximately 0.15 m (6 in.) increments from the left side of the grid cells to the right side of the grid cells. Again, the M385 and BLU-26 are distinct, particularly when they are near the center of the array. When they are underneath the outermost (left or right side) sense elements, edge effects due to the proximity of the sides or return legs of the drive winding distort the object images.

| 0.3 m left shift | 0.15 m left shift | middle scan | 0.15 m right shift | 0.3 m right shift |
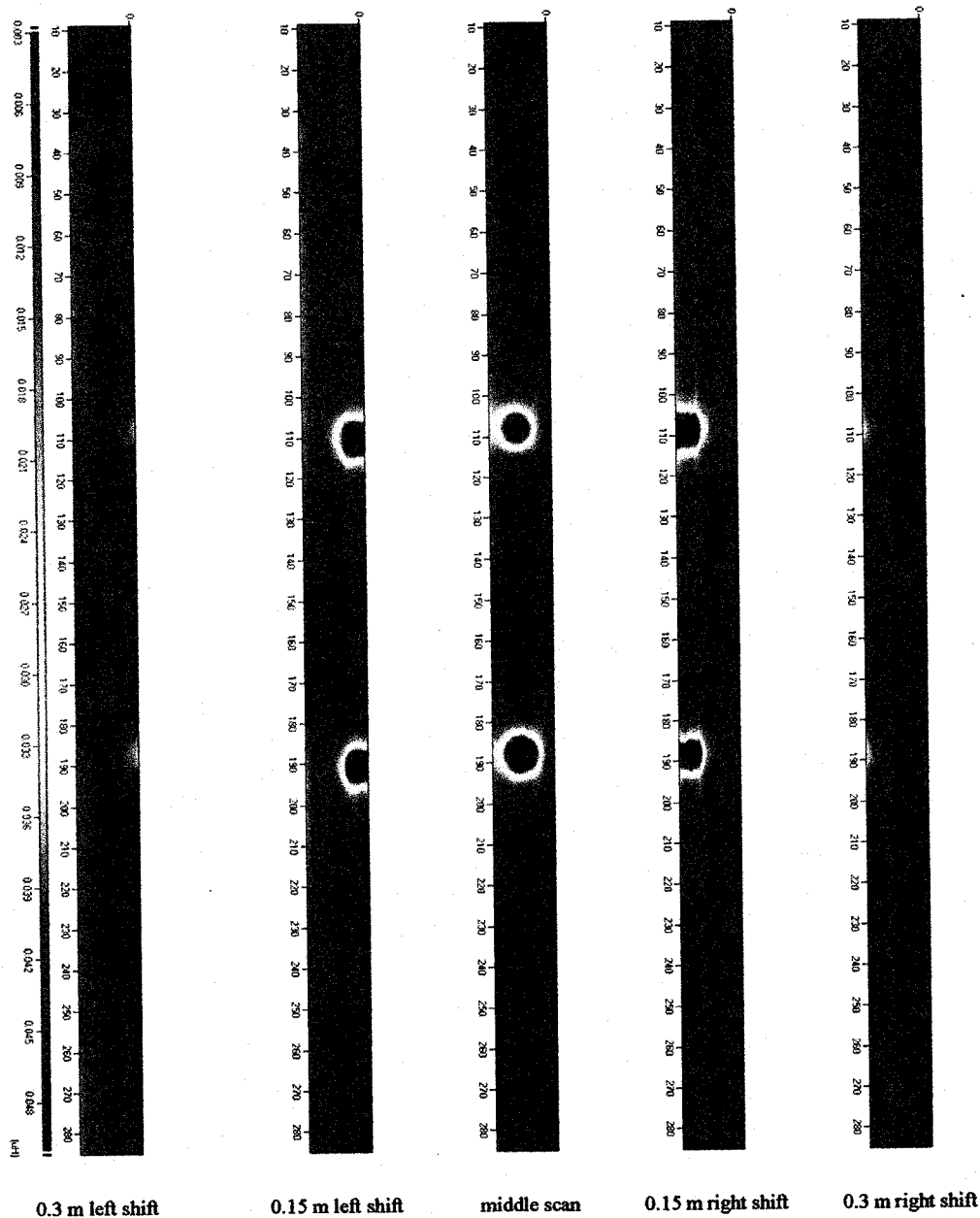
Figure 47. Effect of array offset on image response for vertical scans down cells A3-A6. The vertical axis gives the scan distance in inches. The horizontal axis gives the distance along the sense element array and spans 0.41 m (16 in.). The object type, depth, azimuth angle, dip angle and approximate position are: M55 (0.1 m, 0°, 45°) at ~28 in., M385 (0.1 m, 0°, 45°) at ~106 in., BLU-26 (0.1 m, 0°, 0°) at ~184 in., and M86 (0.4 m, 0°, 45°) at ~262 in.

Measurements were also performed at several different lift-offs or stand-off distances from the ground. Images of the real and imaginary parts of the response, shown in Figure 48, show the decreasing sensitivity to the presence of the objects as the array is raised higher above the ground. In this case, the objects were nominally 10 cm beneath the surface except for the M86, which was buried to a depth of 40 cm. Note that the nominal stand-off distance was 5.1 cm (2 in.) and the stand-offs for the images of Figure 48 go from 2.5 cm (1 in.) to 10.2 cm (4 in.).

Real Part   Imaginary Part

Stand-off: 2.5 cm   5.1 cm   7.6 cm   10.2 cm   2.5 cm   5.1 cm   7.6 cm   10.2 cm
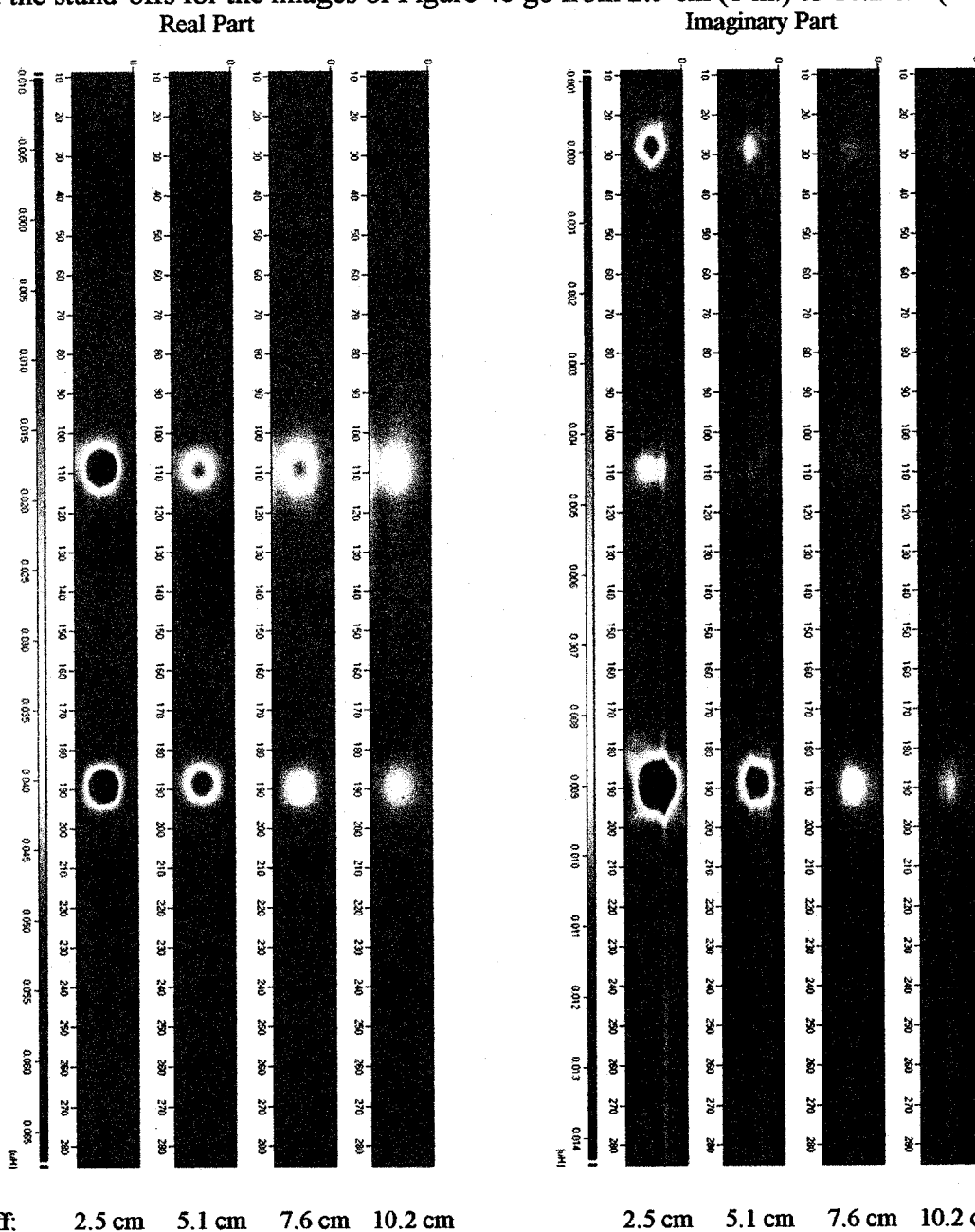
Figure 48. Effect of stand-off distance or lift-off on array response for vertical scans down the middle of cells A3-A6. The vertical axis gives the scan distance in inches. The horizontal axis gives the distance along the sense element array and spans 0.41 m (16 in.). The object type, depth, azimuth angle, dip angle and approximate position are: M55 (0.1 m, 0°, 45°) at ~28 in., M385 (0.1 m, 0°, 45°) at ~106 in., BLU-26 (0.1 m, 0°, 0°) at ~184 in., and M86 (0.4 m, 0°, 45°) at ~262 in.

From the scan images, the values for the real and imaginary parts of the response can be extracted for the center of the object. This corresponds to the object location directly beneath a sense element. These values, plotted in Figure 49, show how the response approaches the "no object" point, which is the origin (0,0) in this plot, as the standoff is increased. The response for the BLU-26 is approximately linear, similar to the laboratory measurements. For the M385, which tends to have a small imaginary response at this measurement frequency, there is more sensitivity to noise in the imaginary part of the signal. Similarly, for the M55, which tends to have a small real response at this measurement frequency, there is more sensitivity to noise in the real part of the signal. Furthermore, as will be shown later, the sensor proximity to the ground tends to have a greater effect on the real part than the imaginary part, which helps to explain the negative values obtained for the real part of the M55 response. **This motivates the use of an additional short spatial wavelength sensor in the follow-on that will allow the local effects of the ground (i.e., standoff distance) to be determined so that it can be compensated for in the characteristic response of the object.**
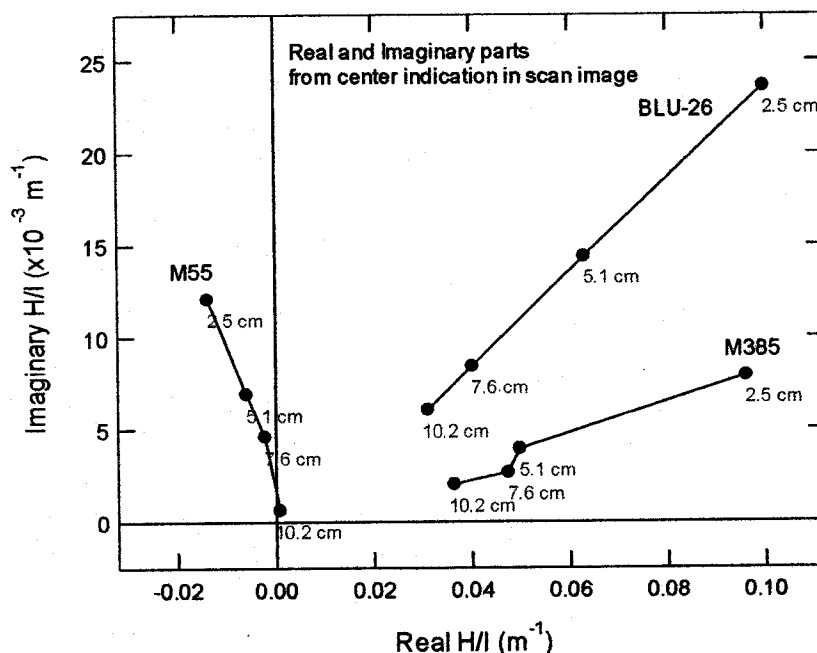

Figure 49. Plot of response from the center of the objects using the scan images of Figure 47.

Measurement scans were performed over a number of the other grid cells as well. Magnitude images resulting from horizontal scans across columns are shown in Figure 50 and Figure 51. Magnitude images resulting from vertical scans across lanes are shown in Figure 55. The emphasis of these preliminary scans was on the shallower objects to demonstrate the imaging capability of the array and to determine sensitivity to objects using a prototype drive winding.

From the horizontal scans of Figure 50 and Figure 51, shallow objects tend to be detectable with this array. The M385 and BLU-26 are evident at depths of 0.1 m and 0.2 m while the BDU-28 is apparent at the 0.1 m depth. Although UXO deeper than 0.2 m tend to be less apparent with this

drive construct, some of the larger objects are apparent at deeper depths. For example, the M49A3 is visible at a depth of 0.25 m, as indicated by Figure 53.
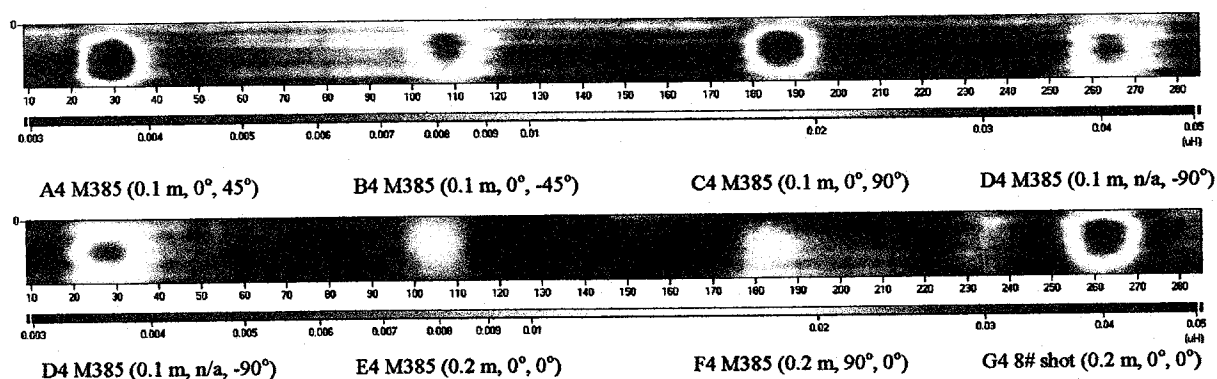

A4 M385 (0.1 m, 0°, 45°)   B4 M385 (0.1 m, 0°, -45°)   C4 M385 (0.1 m, 0°, 90°)   D4 M385 (0.1 m, n/a, -90°)

D4 M385 (0.1 m, n/a, -90°)   E4 M385 (0.2 m, 0°, 0°)   F4 M385 (0.2 m, 90°, 0°)   G4 8# shot (0.2 m, 0°, 0°)

Figure 50. Horizontal scans over the middle of cells in Lane 4. A logarithmic color scale for the magnitude images is shown. The depth, azimuth angle, and dip angle for each object is indicated. The horizontal axis gives the scan distance in inches. The vertical axis gives the distance along the sense element array and spans 0.41 m (16 in.).

A5 BLU-26 (0.1 m, 0°, 0°)   B5 BLU-26 (0.1 m, 0°, 0°)   C5 BLU-26 (0.1 m, 0°, 0°)   D5 BLU-26 (0.1 m, 0°, 0°)

D5 BLU-26 (0.1 m, 0°, 0°)   E5 BLU-26 (0.2 m, 0°, 0°)   F5 BLU-26 (0.2 m, 0°, 0°)   G5 8# shot (0.2 m, 0°, 0°)

G5 8# shot (0.2 m, 0°, 0°)   H5 BDU-28 (0.1 m, 0°, 45°)   I5 BDU-28 (0.1 m, 0°, -45°)   J5 BDU-28 (0.1 m, 0°, 90°)

J5 BDU-28 (0.1 m, 0°, 90°)   K5 BDU-28 (0.1 m, n/a, -90°)   L5 BDU-28 (0.2 m, 0°, 0°)   M5 BDU-28 (0.2 m, 90°, 0°)
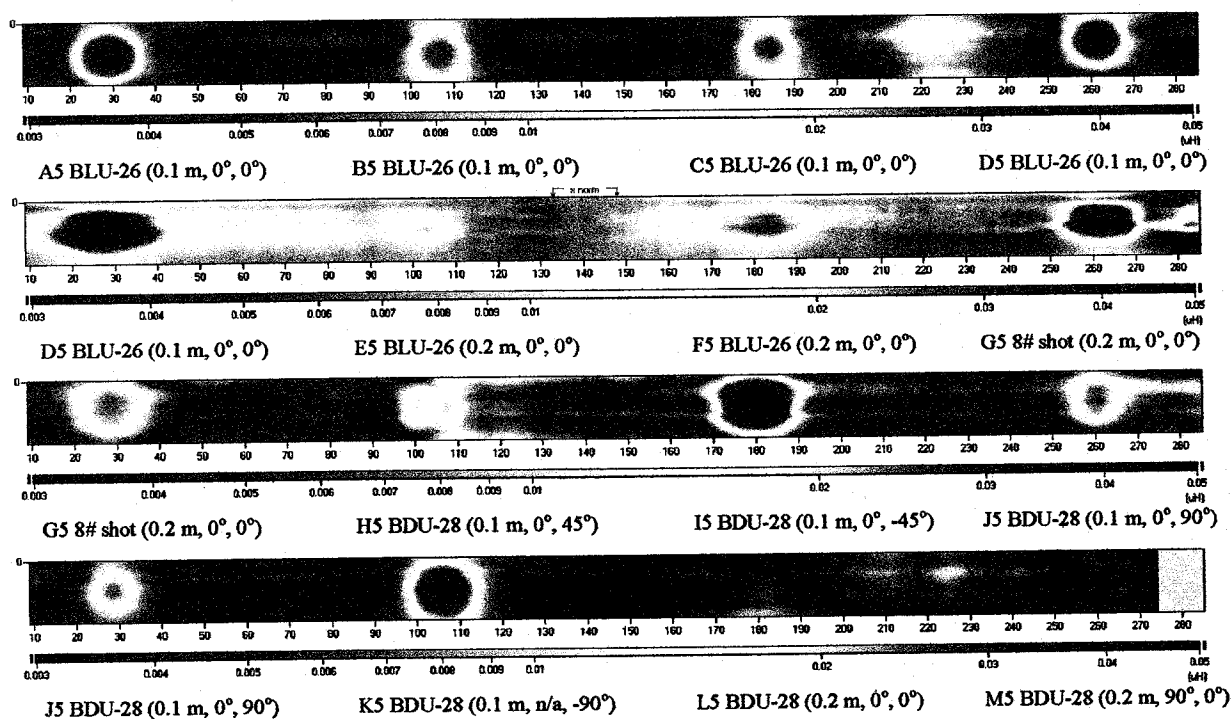
Figure 51. Horizontal scans over the middle of cells in Lane 5. A logarithmic color scale for the magnitude images is shown. The depth, azimuth angle, and dip angle for each object is indicated. The horizontal axis gives the scan distance in inches. The vertical axis gives the distance along the sense element array and spans 0.41 m (16 in.).

Scans were also performed over the grid cells containing clutter. Figure 52 shows the results of one scan across the center region of the cells, containing an M49A3 shell and different levels of clutter. The intensity of the measurement signal increases with the amount of material in the grid cell and is greatest for the cell with high clutter. The color scales of the images are also

dominated by the high clutter response so that the response from the M49A3, which is relatively deep for this sensor to detect, is not readily visible.
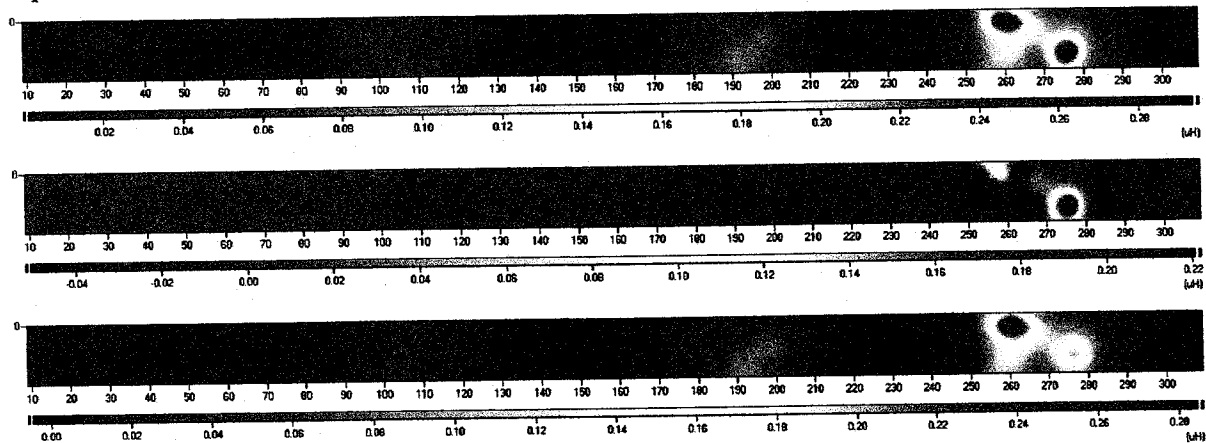

Figure 52. Horizontal scan over the middle of cells H8-K8. All include M49A3 (0.25 m depth, 0° azimuth, 0° dip), with no clutter, low clutter, medium clutter, high clutter spaced approximately 2 m (78 in.) apart. Top: magnitude; Middle: Real part; Bottom: Imaginary part. The axes give the scan dimensions in inches. The vertical axis gives the distance along the sense element array and spans 0.41 m (16 in.)

Figure 53 shows the results of repeated scans over the areas with clutter and uses a logarithmic color scale. This color scale lets the relatively weak signal from the M49A3 itself as well as the strong signals from the clutter to be visible. The color scaling also accentuates any measurement noise and element-to-element variation in the array to be more noticeable. The scans over the cells are repeatable but also show some drift in the response as the time from calibration (e.g., after repeated scans without recalibration) increases.
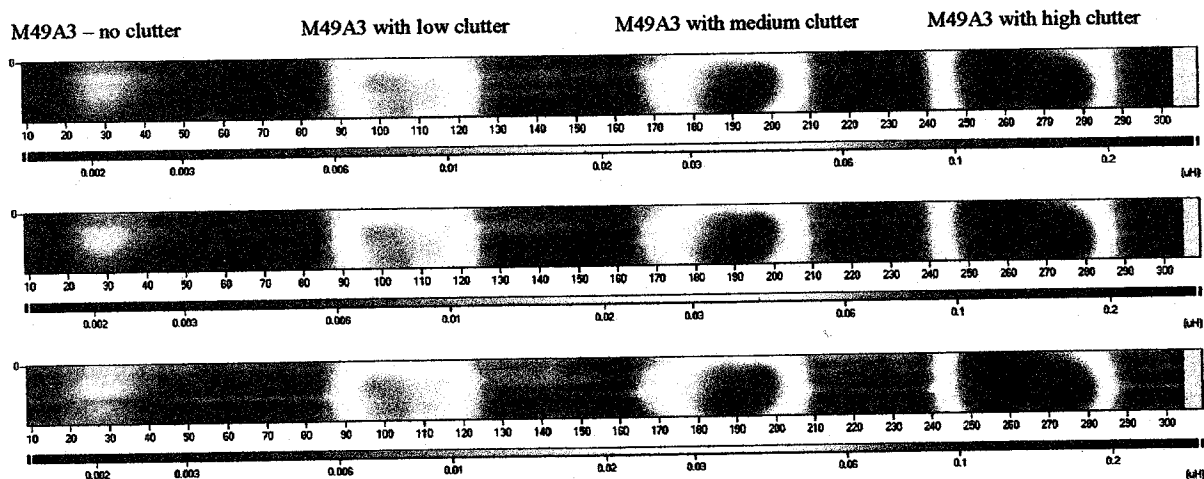

Figure 53. Magnitude scans only, logarithmic scale, for repeated scans over the grid cells with clutter.

The calibration area containing the 0.3 m steel plates was basically underwater and inaccessible for the preliminary measurements with this system. While portions of the area around the 0.6 m steel plates also contained water, this area was more readily accessible. Figure 54 shows the results of several measurement scans over the 0.6 m steel plates. The shallower plate, at a depth of 0.5 m, is readily visible and provides a large spatial response. Offset scans over the top and bottom section of the grid cells capture the spatial extent of the plate response perpendicular to the scan direction. For imaging of large spatial responses such as this a wider array of sensing elements is preferred.
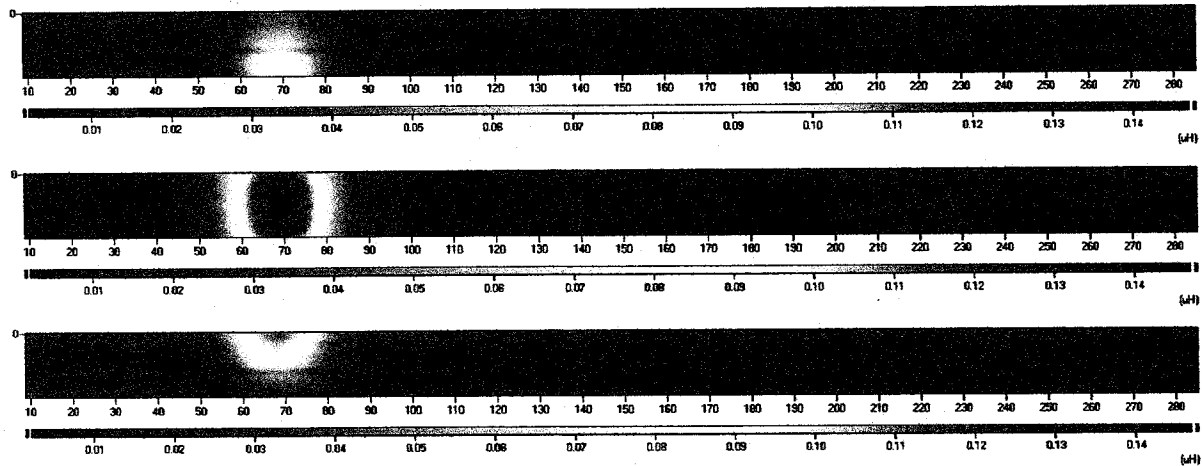

Figure 54. Horizontal scans over cells F11-H11. 0.6 m steel plates were buried to a depth of 0.5 m (near a horizontal position of 70 inches) and to a depth of 1.0 m near a horizontal position of 236 inches.) The middle image was a scan down the center of the lane. The top and bottom images had the array offset by 0.3 m (12 in.). The axes give the scan dimensions in inches. The vertical axis gives the distance along the sense element array and spans 0.41 m (16 in.)

Vertical scans down a column were also performed over some of the objects since the MWM-Array is directional and there can be additional information gained from scanning in other orientations. **In the follow-on efforts, two or three drive orientations will be used in an integrated approach.** This was demonstrated in the laboratory measurements showing the orientation of the several objects. The results of some of these scans are shown in Figure 55. Note that the color scale was chosen for these figures to highlight weak responses (e.g., M55 at 0.1 m) along with stronger responses (M385 at 0.1 m), even though this highlights ground variations and noise effects as well. Figure 56 shows the real and imaginary parts of the response for several offset scans over the high clutter cell. These images are consistent with the horizontal scans of Figure 52. The response of the clutter is much stronger than the response of the single objects, but also spans a large portion of the grid cell. Additional scans were performed with the array offset to the left and right sides as well. Even though these offset scans were not registered very well with respect to the scan down the middle of the lanes, they provide an indication of the spatial extent of the clutter. **JENTEK often uses spatial signatures to suppress background and instrument noise. These should be used in the follow-on effort for UXO.**
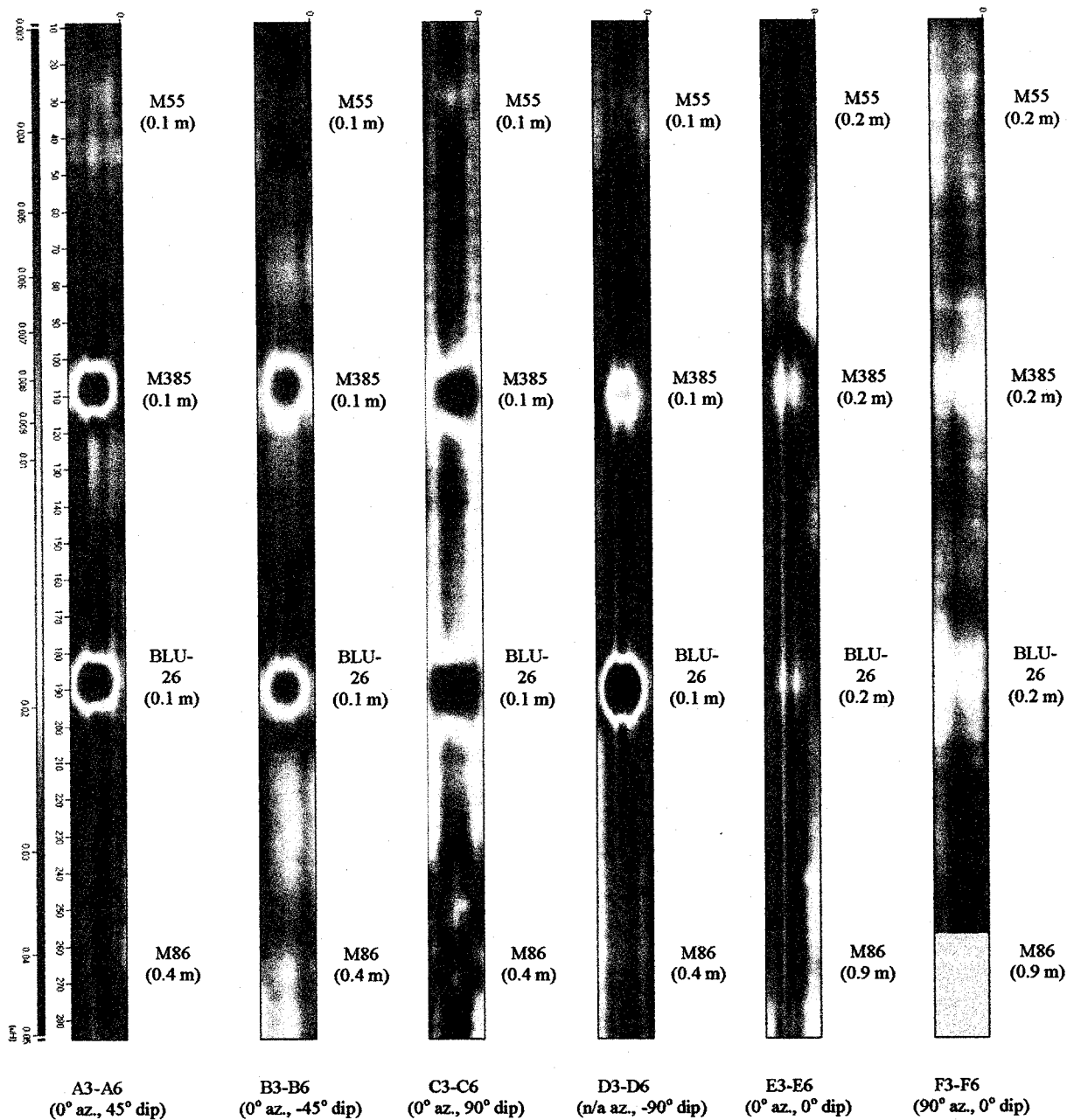
Figure 55. Vertical scans down the middle of several grid cells. Object type, depth, azimuth angle, and dip angle are specified. The axes give the dimensions in inches. The horizontal axis gives the distance along the sense element array and spans 0.41 m (16 i.n).
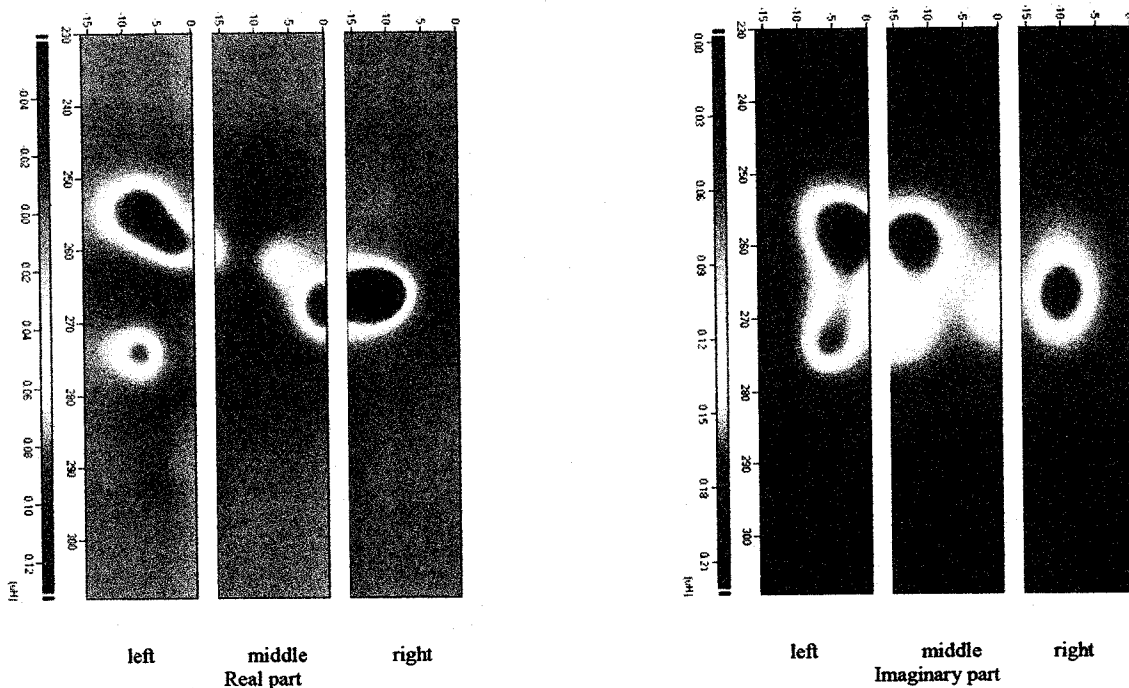
Figure 56. Results of three vertical scans over the high clutter cell (K8), which also contains an M49A3 at a depth of 0.25 m, 0° azimuth, 0° dip. The scans down the middle, left, and right sides provide spatial information about the detected object over a wide area.

A variety of baseline or diagnostic measurements were also performed. As an example, Figure 57 shows the result of measurements performed with a stationary array over a grid cell that should not have any objects. The array was calibrated prior to performing the measurement of Figure 57a and the plot of the transient data versus element number shows that any drift and element-to-element variability is modest. Figure 57b shows a similar plot, without a recalibration, that was taken after a scan across several grid cells. While the drift, indicated by the error bars, remains modest, there is noticeable element-to-element variability. This element-to-element variability is attributed to the mechanical motion. **In the follow-on effort, methods to reduce drift and perform rapid recalibrations should be included.**

Measurements were also performed over grid cells that did not contain any objects. Figure 58 shows the scan data for one set of grid cells. The real part, and hence the magnitude, of the response shows relatively large variations near the center area of the scan. In contrast the imaginary part does not show significant variation along the scan; the striping in the image reflects the element-to-element variability of the response. The response near the center area is associated with variations in the sensor lift-off from the ground or with ground property variations. This response is repeatable. As a contrast, a scan performed over another group of grid cells without objects is shown in Figure 59 and does not have the gradual response near the center of the scan. This scan is relatively clear, except for some drift in the real part of the response and an occasional rapid change in the response for all of the sense elements. **This type**

of response can be removed using a filter that removes the common mode response at a particular measurement location.

For reference, Figure 60 shows the effect of lifting the array over a fixed grid cell location (without an object) so that the effects of proximity to the ground can be quantified. This indicates that the standoff from the ground can have a significant effect on the real part of the response, but a minimal effect on the imaginary part. The error bars in the plot denote the standard deviation of the measurements at each height and across all of the sense elements.
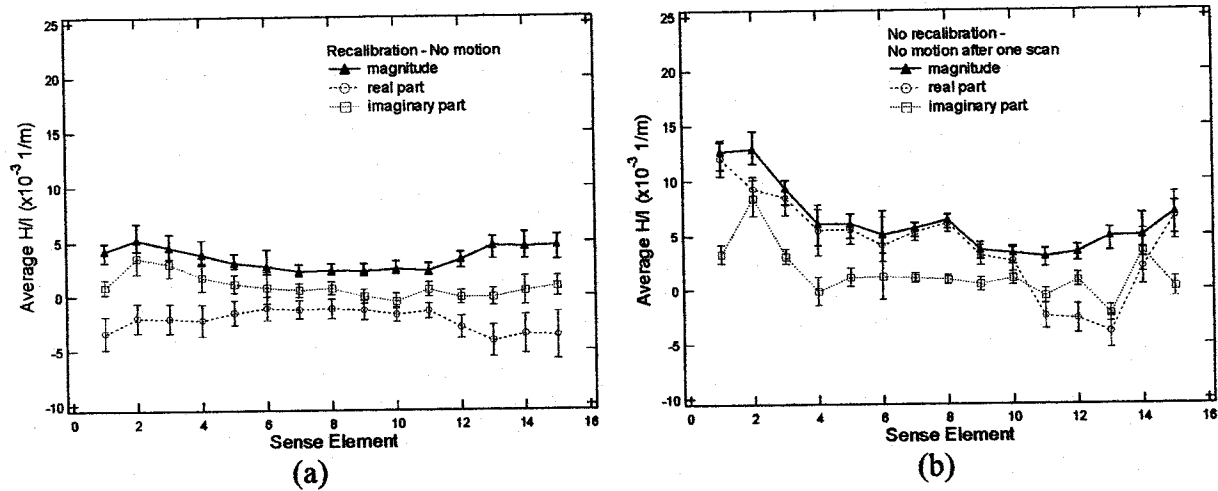

(a)   (b)

Figure 57. The variation in response between elements, where the error bars denote the standard deviation of the measurements. These plots reflect no motion, stationary, measurements. (a) The array was recalibrated prior to these measurements. (b) Data was taken after a scan over approximately four grid cells.
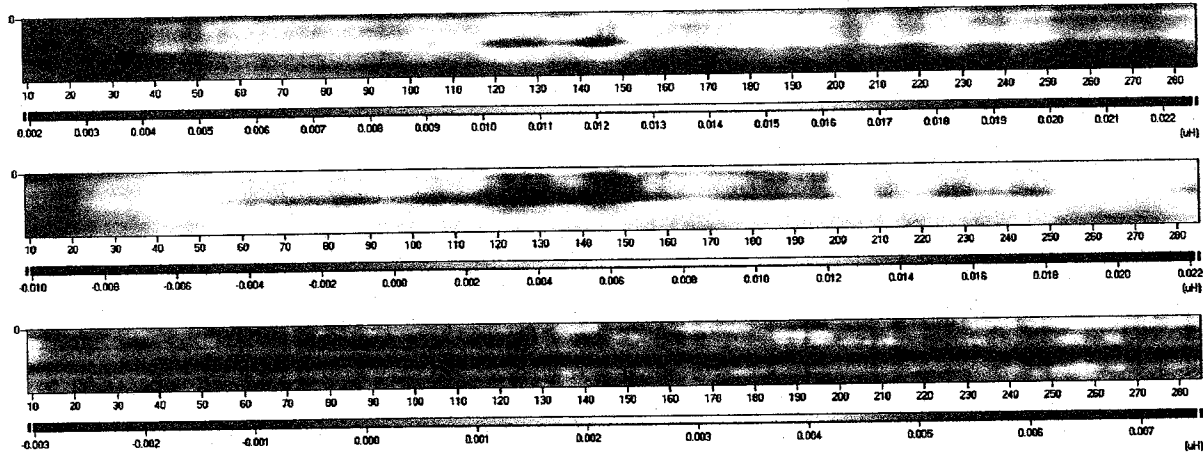
Figure 58. Scan over grid cells without objects, in the middle of cells between Lanes 12 and 13 from Column F to ~J. Top: magnitude; Middle: Real part; Bottom: Imaginary part. The horizontal axis gives the scan distance in inches. The vertical axis gives the distance along the sense element array and spans 16 inches (0.41 m).
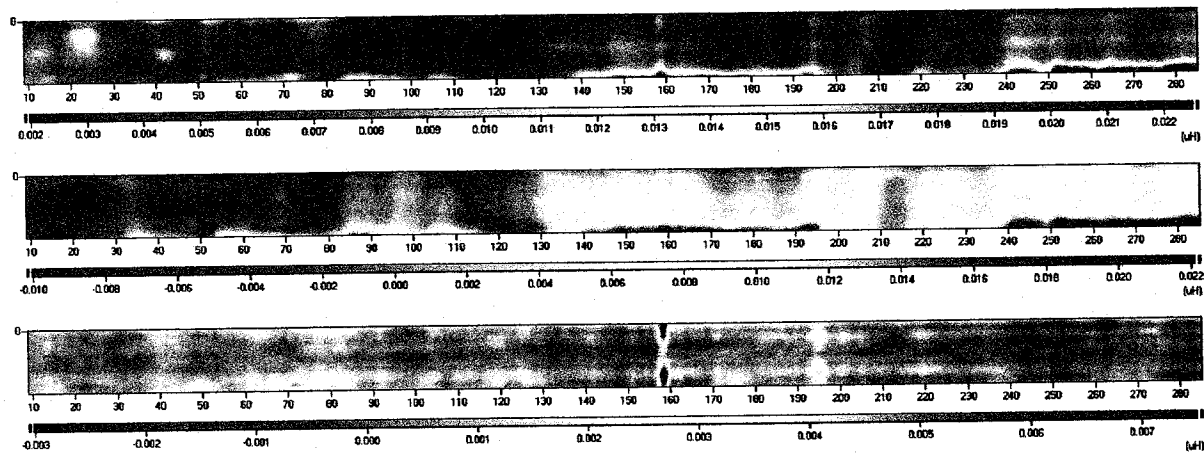

Figure 59. Scan over another group of grid cells without objects, in the middle of cells between Lanes 2 and 3 from Column between E and F to ~J. Done without rails. Top: magnitude; Middle: Real part; Bottom: Imaginary part. The horizontal axis gives the scan distance in inches. The vertical axis gives the distance along the sense element array and spans 16 inches (0.41 m).
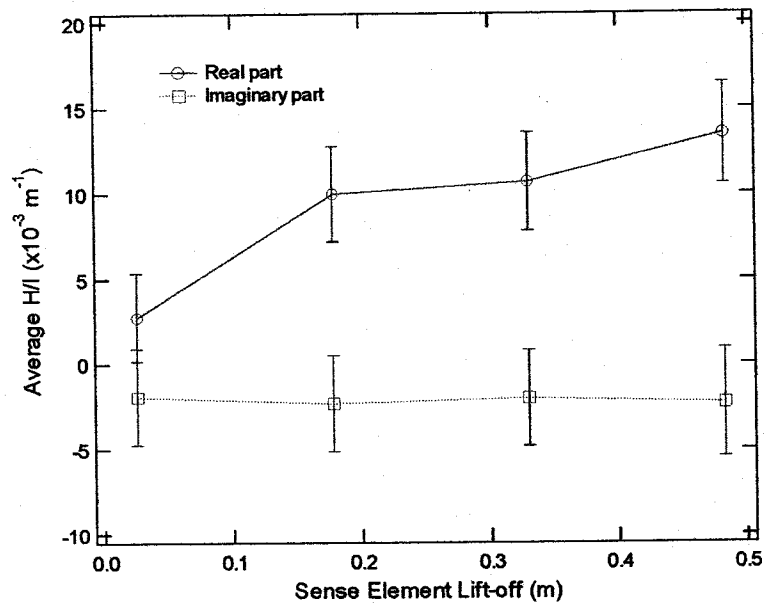
Figure 60. No scan motion measurement. The array was raised from 2.5 cm (1 in.) in ~15.2 cm (6 in.) increments every 500 points. The average signal is from all 16 elements at each height.

Diagnostic measurements were planned for the test pit, where scans were to be performed over known objects at specific depths. However, the conditions of the test pit, shown in Figure 61, prevented these measurements from being performed. Water was drained from the pit on the first day with the hope that it would dry out sufficiently by the last day of the trial. In addition, significant settling and dirt transfer outside the pit boundaries, where digging is not allowed, made the surface of the test pit much lower than the surrounding soil.
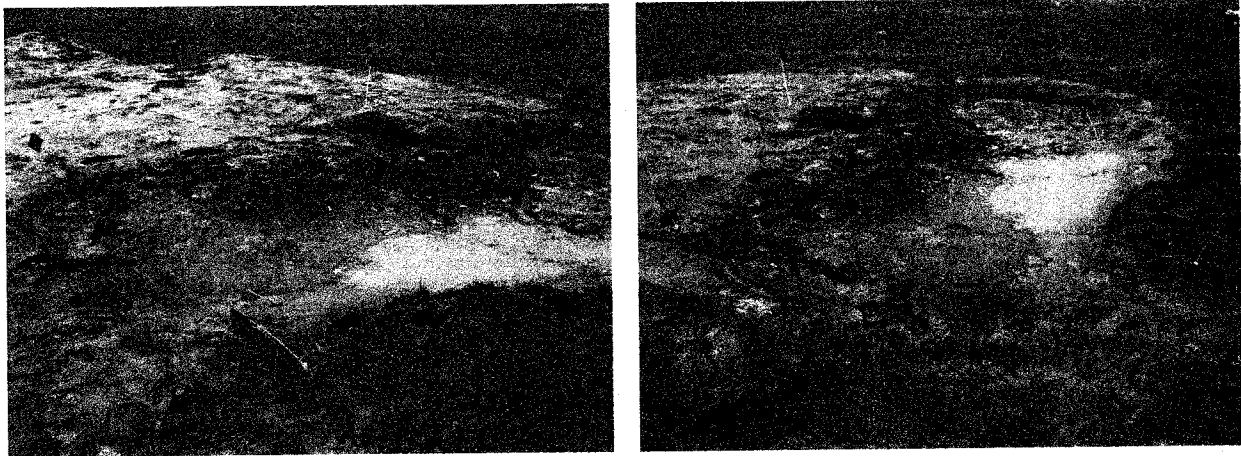

Figure 61. Photographs of the test pit area.

Criteria for Enhancements and Recommendations

This base program was aimed at generating a capability baseline for the development of an electromagnetic induction sensor array for UXO detection and clutter suppression. The eventual goal for the program is a robust discriminator for buried objects. Preliminary measurements in the laboratory and the field were performed in the base program using an existing prototype drive winding, with minor modifications, and an array of sensing elements for imaging of hidden objects. Based on these preliminary measurements, enhancements to the system have been identified. These criteria address both performance-based and instrumentation issues, as:

- **Depth of sensitivity to UXO** – This reflects the signal-to-noise ratio of the instrumentation for specific objects at prescribed depths. The noise includes background variations in soil properties as well as drift and instrumentation noise. Another aspect of this criterion is the accuracy and robustness of the estimates of the object properties.
- **Multiple object resolution** – This reflects the capability to isolate or characterize the response of individual objects that are near one another. This could include benign clutter over a UXO or multiple proximate UXO. Similar to the depth of sensitivity, this could be defined in terms of specific objects at prescribed depths and with prescribed separations.
- **Sensitivity to soil properties** – Variations in soil properties, such as the magnetic permeability or electrical conductivity, can affect the response of electromagnetic induction instruments and can mask the response of UXO unless accounted for.
- **Probability of detection** – This provides a measure of system performance for detecting all relevant objects.
- **Confidence of identification** – This addresses the capability to identify an object as harmful or benign after detection.
- **Data acquisition rate and scan speed** – Efficient site reclamation requires sufficiently high data acquisition and scan rates for the signature responses of the buried objects to be captured and characterized.
- **Instrument bandwidth** – This should be large enough so that measurements capture enough of the frequency dependent response to assist in the characterization of the UXO. Higher bandwidth may reduce the achievable scan speed.
- **Instrument portability** – The size, weight, and cost of the instrument are considerations for deployment and field use.
- **Sensor array scalability** – The array needs to be large enough to provide sensitivity to deep objects within the typical depth of UXO (e.g., 1 m).
- **Data processing** – Data obtained for the objects should be processed rapidly and accurately to provide an assessment of the object characteristics. This data includes, for example, the scan images as well as multiple frequency, sense element location and sense element orientation information.
- **Observability of object features** – the ability to independently measure multiple object features such as size, depth, orientation, material type, and shape (e.g., aspect ratio).

Recommendations for the follow-on effort include:

- **Deeper penetration depth drive** – The drive winding should be modified to permit a deeper penetration depth for the magnetic field into the soil. The prototype drive used in this base program has a depth limitation of roughly 0.45 m (18 in.), including the standoff distance to the ground surface, so the focus has been on objects located within approximately 0.4 m (16 in.) of the surface. The depth for UXO can be up to 1 m.

- **Wider drive and larger array of sense elements** – Since edge effects were visible at the outermost sense elements of the array, to improve the image quality the drive winding should be modified by extending the drive winding segments further past the sense element array. A longer array of sense elements facilitates imaging of deeper and larger objects since a single scan of the array may provide a complete spatial image of the response. A higher resolution array (e.g., 32 instead of 16 elements) would also improve the capability to determine object shape.

- **Multiple spatial wavelength measurements** – Modifying the sensor design to perform measurements at multiple spatial wavelengths would permit compensation for local ground property and stand-off variations. This should also permit the separation of near surface object and/or soil property effects on the response from deep object property variations. JENTEK often uses spatial signatures to suppress background and instrument noise.

- **Addition of complementary sense elements** – Sensing elements placed at multiple locations within the drive footprint and at different orientations capture complementary information about the buried object. This could be accomplished with a two-dimensional array of sense elements.

- **Reduced sense element variability** – This is necessary for the construction of high resolution images and can be accomplished with hardware and software modifications. For example, drift can be reduced with occasional rapid recalibration. In software, normalizing across the elements at a user-selected location, preferably not over an object, would reduce image striping.

- **Improved ease of use** – The system should be more portable for field measurements and may include mounting equipment onto the cart.

- **Reduced mechanical sensitivity of array to cart motion** – The cart design should be modified to reduce tilting of the array over uneven terrain while maintaining the ability to raise and lower the array over detected objects. Filters can remove the common mode (noise) response at a particular measurement location.

- **Additional location information** – Incorporation of a GPS locator or some other location method would facilitate scanning of large areas. The use of a single position encoder can provide accurate local position measurements but only in one direction.

- **Multiple frequency measurements** – The spectral response reflects material and geometric properties of the UXO. Measurements have been performed at a single frequency, but there is additional information that could be obtained from multiple frequency measurements.

- **Detection and suppression algorithm enhancements** – The algorithms for characterizing the objects and clutter suppression need to integrate the responses from multiple sensing elements, preferably at multiple element locations and orientations within the drive footprint, with multiple measurement frequencies. They also need to

combine information from high resolution images with property estimates from measurement grids or some other model based approach. Measurement responses from two or three drive orientations should also be incorporated.

- **Nonspherical object model development** – Basic object property estimates have been obtained with a sphere-based model, but better estimates are expected when the nonspherical shape of typical UXO is accounted for. The use of ellipsoid models with multiple sensing elements to discriminate object features (shape, size, orientation) should be investigated.

- **Multiple drive orientations** – Multiple drive winding orientations are necessary to improve observability for different object types.

Concluding Remarks

This base program was aimed at generating a base-line response for an electromagnetic induction imaging array for UXO detection and discrimination. The focus was on adapting our impedance instrumentation to function with a prototype array to demonstrate capabilities and limitations of this early stage system and to demonstrate the use of models for extracting information about object features. All technical milestones for this base program have been met. These milestones led to the generation of enhancement criteria and recommendations that are expected to be pursue in the follow-on program.

The base program accomplishments include (1) adapting an existing drive winding and an array of sense elements to work with parallel architecture impedance instrumentation; (2) demonstrating that improving (e.g., doubling) the array resolution can be accomplished without affecting the signal-to-noise ratio; (3) demonstrating a rapid-scanning capability; (4) demonstrating that scan images can reflect object orientation and shape and also the presence of multiple proximate objects; (5) demonstrating a preliminary size and depth estimation capability using a model-based approach; and (6) a similarity of object signature responses in the laboratory and the field.

System enhancements recommended for the follow-on effort include: (1) modifying the drive winding for deeper object sensitivity and to reduce edge effects on the image; (2) fabrication of a two-dimensional array of sense elements; (3) multiple spatial wavelength measurements; (4) algorithm enhancements to suppress background effects, sense element variability, and clutter; (5) methods to reduce common mode noise; and (6) use of two or more drive winding and sensing element orientations to further improve observability.

REPORT DOCUMENTATION PAGE

1. REPORT DATE *(DD-MM-YYYY)*	2. REPORT TYPE	3. DATES COVERED *(From - To)*

4. TITLE AND SUBTITLE

5a. CONTRACT NUMBER

5b. GRANT NUMBER

5c. PROGRAM ELEMENT NUMBER

6. AUTHOR(S)

5d. PROJECT NUMBER

5e. TASK NUMBER

5f. WORK UNIT NUMBER

7. PERFORMING ORGANIZATION NAME(S) AND ADDRESS(ES)

8. PERFORMING ORGANIZATION REPORT NUMBER

9. SPONSORING/MONITORING AGENCY NAME(S) AND ADDRESS(ES)

10. SPONSOR/MONITOR'S ACRONYM(S)

11. SPONSOR/MONITOR'S REPORT NUMBER(S)

12. DISTRIBUTION/AVAILABILITY STATEMENT

13. SUPPLEMENTARY NOTES

14. ABSTRACT

15. SUBJECT TERMS

16. SECURITY CLASSIFICATION OF:			17. LIMITATION OF ABSTRACT	18. NUMBER OF PAGES	19a. NAME OF RESPONSIBLE PERSON
a. REPORT	b. ABSTRACT	c. THIS PAGE			
					19b. TELEPHONE NUMBER *(Include area code)*

Standard Form 298 (Rev. 8/98)
Prescribed by ANSI Std. Z39.18

INSTRUCTIONS FOR COMPLETING SF 298

1. REPORT DATE. Full publication date, including day, month, if available. Must cite at least the year and be Year 2000 compliant, e.g. 30-06-1998; xx-06-1998; xx-xx-1998.

2. REPORT TYPE. State the type of report, such as final, technical, interim, memorandum, master's thesis, progress, quarterly, research, special, group study, etc.

3. DATES COVERED. Indicate the time during which the work was performed and the report was written, e.g., Jun 1997 - Jun 1998; 1-10 Jun 1996; May - Nov 1998; Nov 1998.

4. TITLE. Enter title and subtitle with volume number and part number, if applicable. On classified documents, enter the title classification in parentheses.

5a. CONTRACT NUMBER. Enter all contract numbers as they appear in the report, e.g. F33615-86-C-5169.

5b. GRANT NUMBER. Enter all grant numbers as they appear in the report, e.g. AFOSR-82-1234.

5c. PROGRAM ELEMENT NUMBER. Enter all program element numbers as they appear in the report, e.g. 61101A.

5d. PROJECT NUMBER. Enter all project numbers as they appear in the report, e.g. 1F665702D1257; ILIR.

5e. TASK NUMBER. Enter all task numbers as they appear in the report, e.g. 05; RF0330201; T4112.

5f. WORK UNIT NUMBER. Enter all work unit numbers as they appear in the report, e.g. 001; AFAPL30480105.

6. AUTHOR(S). Enter name(s) of person(s) responsible for writing the report, performing the research, or credited with the content of the report. The form of entry is the last name, first name, middle initial, and additional qualifiers separated by commas, e.g. Smith, Richard, J, Jr.

7. PERFORMING ORGANIZATION NAME(S) AND ADDRESS(ES). Self-explanatory.

8. PERFORMING ORGANIZATION REPORT NUMBER. Enter all unique alphanumeric report numbers assigned by the performing organization, e.g. BRL-1234; AFWL-TR-85-4017-Vol-21-PT-2.

9. SPONSORING/MONITORING AGENCY NAME(S) AND ADDRESS(ES). Enter the name and address of the organization(s) financially responsible for and monitoring the work.

10. SPONSOR/MONITOR'S ACRONYM(S). Enter, if available, e.g. BRL, ARDEC, NADC.

11. SPONSOR/MONITOR'S REPORT NUMBER(S). Enter report number as assigned by the sponsoring/ monitoring agency, if available, e.g. BRL-TR-829; -215.

12. DISTRIBUTION/AVAILABILITY STATEMENT. Use agency-mandated availability statements to indicate the public availability or distribution limitations of the report. If additional limitations/ restrictions or special markings are indicated, follow agency authorization procedures, e.g. RD/FRD, PROPIN, ITAR, etc. Include copyright information.

13. SUPPLEMENTARY NOTES. Enter information not included elsewhere such as: prepared in cooperation with; translation of; report supersedes; old edition number, etc.

14. ABSTRACT. A brief (approximately 200 words) factual summary of the most significant information.

15. SUBJECT TERMS. Key words or phrases identifying major concepts in the report.

16. SECURITY CLASSIFICATION. Enter security classification in accordance with security classification regulations, e.g. U, C, S, etc. If this form contains classified information, stamp classification level on the top and bottom of this page.

17. LIMITATION OF ABSTRACT. This block must be completed to assign a distribution limitation to the abstract. Enter UU (Unclassified Unlimited) or SAR (Same as Report). An entry in this block is necessary if the abstract is to be limited.